A NOVEL 3D-BIOPRINTING PLATFORM FOR THE FORMATION OF DENSE TISSUE FIBRES FROM DILUTE NEWTONIAN BIOINKS DEPOSITED INTO THIXOTROPIC XANTHAN GUM HYDROGEL EMBEDDING BATHS

MASTER'S THESIS

N.J.J. Kroese

Applied Stem Cell Technologies (AST)

Supervisors
Dr. V. Schwach
Applied Stem Cell Technologies

MSc V. Trikalitis
Vascularization Lab

Committee Chairman
Prof. Dr. P.C.J.J. Passier
Applied Stem Cell Technologies

External Committee Member
Dr. Ir. J. Rouwkema
Vascularization Lab

UNIVERSITY OF TWENTE.

2024

Abstract

In this thesis a scaffold-based extrusion 3D-bioprinting platform is introduced where an aqueous Newtonian bioink is deposited in a non-Newtonian thixotropic shear thinning xanthan gum (XG) hydrogel embedding bath.

Upon depositing a dilute particle-laden bioink into this bath, a rapid local particle concentration increase was observed, resulting from a radial diffusion of the bioink's carrier fluid and hydrogel redistribution and/or swelling.

This process, dubbed *diffusion packing*, was to our knowledge not used or described in literature, although is it likely present in similar bioprinting efforts.

To generate greater insight into this process, a custom imaging setup was employed, which was able to track the positions of the ink and bath components separately and in real-time, which showed the effect of altering extrusion values and the clear differences in deposition patterns between deposition in viscous Newtonian support and this non-Newtonian hydrogel support bath.

The thixotropic rheological properties of XG comprises high viscosity at relatively low concentrations, which causes the gel to restore the crevices formed in the wake of traveling needle gradually. Filling these plotted crevices readily with low viscosity bioink resulted in a vertical column, or sheet, of ink, and thus low bioink retention at the initial extrusion site was observed). To circumvent this issue, 90° bent stainless-steel needles were employed, which were able to inject the bioink at sufficient distance from the traveling needle to allow for bath recovery and the deposition in a cylindrical and horizontal ink column. Although this limits freedom in printing designs, observations suggested that optimizing the bath composition would allow for the use of regular straight vertical needles in future research.

The capabilities of this platform were tested by the printing of bioinks laden with proliferating stem cells, C2C12-cells, non-proliferating cardiomyocytes (CM), a mixture of cardiac cell types CMs and epicardial-like cells (ECCs), Smooth Muscle Cells (SMCs) suspensions and SMC-spheroids with and without collagen-coated PLA-μparticles.

The main liquid component of both the bioink as well as the embedding bath consisted of cell-culture medium, which can be tuned to most cell-types, facilitating a nutrient rich environment in which they could be cultured for days, with minimal disruptions during their very delicate initial development phase.

If sufficiently high local concentrations were reached, stable tissue fibres self-assembled, the characteristics of which were greatly influenced by their constituent cell type(s).

Cellular re-organisation was readily observed and was especially noticeable in the CMs & ECCs cardiac tissue fibres and the integration of Col-PLA-μparticles in SMC tissues, all aided by the inherently biocompatible, stable, and bioinert nature of XG and the absence of an interstitial hydrogel.

A simple series of dilutions, which also functioned as a refreshment step, removed the XG and liberated tissue constructs which, if sufficiently stable, could be picked up and manipulated while remaining intact.

When looking at the current printing results, in which the diffusion packing mechanism place a key role, and the potential capabilities which could be harnessed by future optimization, this platform allows for a relatively easy, quick, inexpensive, and highly tuneable platform for the creation of stable tissue constructs.

Samenvatting

In deze scriptie wordt een *scaffold-based extrusion 3D-bioprinting* platform geïntroduceerd waarbij een waterige Newtoniaanse bioinkt in een niet-Newtoniaanse thixotrope *xanthan gum* (XG) hydrogel suspensiebad wordt geïnjecteerd.
Bij het inbrengen van een bioink, bestaande uit verdunde een suspensie vaste deeltjes, in dit bad werd een snelle lokale toename van de deeltjesconcentratie waargenomen, als gevolg van een radiale diffusie van de bioinkt's dragervloeistof en een herverdeling en/of zwelling van de hydrogel. Dit proces, genaamd *diffusion packing*, was naar onze kennis niet gebruikt of beschreven in de literatuur, hoewel het waarschijnlijk aanwezig is in vergelijkbare bioprint experimenten.

Om meer inzicht te krijgen in dit proces werd een zelfgebouwde beeldvormingsopstelling gebruikt, die de positie van de belangrijke componenten van zowel de inktsuspensie als het suspensiebad afzonderlijk kon vastleggen en zo het proces live kon volgen. Het effect van het veranderen van extrusiewaarden en de duidelijke verschillen in afzetpatroon tussen afzetting in viskeuze Newtoniaanse ondersteuning en dit niet-Newtoniaanse hydrogel bad kon zo worden gevisualiseerd.
De thixotropische reologische eigenschappen van XG betekenden een relatief lange hersteltijd naar een *steady-state* na abrupte veranderingen in aangebrachte afschuifspanning, wat resulteerde in spleetvormige openingen in het kielzog van de bewegende naalden. Dit werd snel gevuld met de bioinkt van lage viscositeit, resulterende in een verticale kolom van bioink en dus lage inkt retentie op de bedoelde plaats van injectie. Als oplossing van dit probleem werden 90° gebogen roestvaststalen naalden gebruikt, die het bioinkt op een afstand ver genoeg van de naald te injecteren voor het vormen een cilindrische en horizontale inktkolom. Hoewel dit de vrijheid in printontwerpen beperkt, zijn er observaties dat na optimalisatie van de badsamenstelling, het gebruik van rechte verticale naalden in toekomstig onderzoek waarschijnlijk mogelijk zijn.
De mogelijkheden van dit platform werden getest door het printen van bioinkten beladen met prolifererende stamcellen, C2C12-cellen, niet-prolifererende cardiomyocyten (CM), een mengsel van cardiale celtypen CM en epicardiale-achtige cellen (ECC's), gladde spiercellen (SMC's) hetzij gescheiden of in sferoïde cluster en hetzij samen met collageen-gecoate PLA-µdeeltjes of niet.
Het belangrijkste vloeibare onderdeel van zowel de bioinkt als wel het inbeddingsbad bestond uit celkweekmedium, die kan worden aangepast op de meeste celtypes, wat een voedingsrijke kweekomgeving vort waarin ze dagenlang kunnen worden gekweekt.
Als lokale celconcentraties een voldoende dichtheid bereikten, vormden zich weefsels, waarvan de eigenschappen sterk werden beïnvloed door de celtype(n) waaruit ze waren samengesteld. Reorganisatie van cellen werd duidelijk waargenomen en was vooral te herkenning in de CM's & ECC's hartweefsel en de bij de incorporatie van Col-PLA-µdeeltjes in SMC-weefsels, mogelijk gemaakt door de inherent biocompatibele en stabiele aard van XG en de afwezigheid van interstitiële hydrogel.
Een eenvoudige reeks verdunningen, die ook fungeerde als een voedingsstap, verwijderde de XG en bevrijdde weefselconstructies die, indien voldoende stabiel, konden worden opgepakt terwijl ze intact bleven.
Als we kijken naar de huidige printresultaten, waarbij het *diffusion-compaction* mechanisme een sleutelrol speelt, en de potentiële mogelijkheden die door toekomstige optimalisatie benut zouden kunnen worden, biedt dit platform een relatief eenvoudig, snel, goedkoop en zeer aftelbaar platform voor het creëren van stabiele weefselstructuren.

Acknowledgements

I would like to thank Robert Passier and all the people from AST for providing the opportunity to do my master thesis in their group. Together is chairman of the examination committee Robert, I would like to thank Verena Schwach, and from the Vascularization Lab, Vasileios Trikalitis and Jeroen Rauwkema. During our regular meetings Verena provided her invaluable knowledge, ideas, and passion on the biological aspect of the bioprinting platform and her vision on its role in future tissue engineering efforts. The first time I saw the spontaneous contraction of a gathering of cardiomyocytes, made me appreciate the non-stop and often underappreciated effort of millions of those tiny workers we call cells comprising the human heart, and is a fond memory I will not soon forget. Second on this thank-you-list but certainly not second for providing his knowledge and ideas is Vasileios. Even more than bringing his in-depth knowledge, his thirst for understanding and his patience in the efforts to describe the basics of any complicated concept to a comparatively simple guy like myself, is giving me the idea science can be viewed as something like a game. A game with strict rules and frustrating at times yes, however when invested and played well and honest, certainly fun, all player forging different paths to an end goal which might yet be unclear, making the journey there together all the more important. Thank you also for proving my first spot as an author on a published paper, which also benefited greatly from the in-depth analyses of the dynamics occurring on the microscopic scale made possible by the custom setup both build and operated by the kind Mert Kaya. I would like to thank Danique Snippert, Simone ten Den and Carla Cofino Fabres for, what probably seemed to them, an endless supply of their finest cells of all varieties which the 3D-printer just couldn’t get enough off. I would also like to thank Carla for helping me see the light, albeit fluorescent, transmission or confocal, regarding the microscopic world.

Table of Contents

Abbreviations & symbols

Bone morphogenetic protein 4	BMP4
Bovine aortic endothelial cells	BEAC
Bovine serum albumin	BSA
BSA polyvinyl alcohol, essential lipids	BPEL
Calcium-induced calcium release	CICR
Cardiomyocyte	CM
CM-growth medium	CM-GM
CM-maturation medium	CM-MM
COUP transcription factor	COUP-TFII
Citric acid	CA
Decellularized ECM	dECM
Density	ρ
Dulbecco's Modified Eagle Medium	DMEM
Dulbecco's phosphate-buffered saline	DPBS
ECC-growth medium	ECC-GM
Effective fluid dynamic viscosity	μ_{eff} [Pa s]
Elastic modulus	E''
Epicardial(-like) cell	ECC
Essential 8-medium	E8
Extracellular matrix	ECM
Fetal bovine serum	FBS
Flow behaviour index	n [-]
Flow consistency index	K [Pa s^n]
Flow speed	u [m s^{-1}]
Glucose	G
Glycogen synthase kinase 3	GSK3
(enhanced) Green fluorescent protein	(e)GFP
Horse serum	HS
Human activin A	ACT-A
Human adipose derived stem cell	hASC
Human dermal fibroblast	hDF
Human embryonic stem cell	hESC
Human mesenchymal stem cell	hMSC
Human pluripotent stem cell	hPSC
Human umbilical vein endothelial cell	HUVEC
Hyaluronic acid	HA
Inner diameter	$\emptyset_{ID}$
Ink column	IC
Linear viscoelastic region	LVER
Liquid nitrogen	LN

Methacrylate	MA
Methacrylated gelatin	GelMA
Methacrylated XG	XGMA
Na-DL-lactate	L
Outer diameter	$\emptyset_{OD}$
Oxidized methacrylated alginate	OMA
Paraformaldehyde	PFA
Particle (volume) fraction	φ_p
Penicillin-streptomycin	P/S
PF127 diacrylate	PF127-DA
Phosphate buffered saline	PBS
Photo initiator	PI
Pluronic F127	PF127
Polydimethylsiloxane	PDMS
Polytetrafluoroethylene	PTFE
Retonic acid	RA
Reynolds number	Re [-]
eRubyII-ACTN2 & GFP-NKX2.5	DRRAGN
SB431543	SB43
Shear stress	μ [Pa]
Shear rate	$(\partial u/\partial y)$ or γ [s^{-1}]
SMC growth medium	SMC-GM
Smooth muscle cell	SMC
Sodium alginate	SA
Stem cells	SC
Storage modulus	G'
Three-dimensional	3D
Thrombospondin-1	TSP-1
Tissue-culture-treated	TCT
Tissue Engineering	TE
Transforming growth factor	TGF
Ultraviolet light	UV
Volume-to-volume	v/v
Volume-to-weight	v/w
Von Willebrand Factor	vWF
Wingless-related integrin-site 1	WNT
Xanthan gum	XG
Yield stress	σ_0 [Pa]

Chapter 1. Introduction

Biological research often requires the uses of models which approximate, albeit partially, the *in vivo* conditions as close as possible to generate detailed understanding on tissue development, cellular responses, and disease modelling. [1]–[3]

Testing on animals provides a model of great complexity, however their use is subject to ethical and financial constraints while also providing limited throughput, and limited control on experimental conditions. [1], [2] Although their value in preclinical physiological models are high, some inherent differences can make a direct translation between animal model-derived results and human cases inaccurate. [4] Something which can be partially improved by humanisation, the incorporation of human cells, in animal models. [5]

Testing on human tissues has been mostly limited to either small test groups, the use of donor material or the laboratory culture of isolated or derived cells and is still subject to most of the ethical, financial and scalability issues and lack in population diversity in trail groups. [6], [7] Therefor the implementation of cell culture-based models currently provides the best model during the early- and mid-stages of biomedical research. [8]

A wide variety of cells can be cultured sufficiently in this manner and the insights into their functioning obtained are invaluable, their culture has however been mostly limited to monolayer geometries, which makes direct comparisons with the complex three-dimensional (3D) complex morphologies and interactions, crucial for *in vivo* physiological functioning, difficult. [8], [9]

Tissue engineering (TE) comprises the ability to engineer 3D structures which approximate biological tissues in function, structure and/or composition, which would not only provide a next step in the enhancement of current biological models, but also potentially providing a platform to develop cell-laden crafts or -particles with predetermined geometries, physical and biological characteristics. These engineered tissues can be implemented *in vivo* for regenerative medicine therapies, function as a platform for *in vitro* experiments on specific and potentially patient tailored functions, and even *in vitro* fabrication of consumable products. [10]-[13]

For the construction of 3D cell culture models the field of TE has been looking at the processes used in object construction such as injection moulding, which is rapid but possesses limited special control, and additive manufacturing, in which constructs are generated incrementally, which is slower but allows for a greater degree of control. [14]

The latter is favoured for the use of TE, due to the initial low cost, exceptional freedom in design for great internal and external geometric complexity from (a combination of) bulk materials, and the opportunity for rapid prototyping. [15]

Being an emerging field, the scales and complexities comparable to the natural occurring differentiating and self-organizational processes present in tissue formation during embryonic development or tissue recovery are not yet achievable. However, simplified and smaller scale microtissues, such as organoids, or cell-or biomolecular-laden hydrogels, have already provided insights in tissue formation, cellular remodelling, their potential role to function as disease models, and their potential role in *in vivo* tissue and organ repair or enhancement. [16], [17]

Additive manufacturing, also called 3D-printing, approaches can be divided into seven different general categories, based on their core working principles. [18]

1) *Powder bed fusion*; the melting of patterned powder layer and subsequent fusion with prior layers. **2**) *Material jetting*; jetting of droplets of material upon the build. **3**) *Binder jetting*; binds a select area of material by jetting binder materials upon it. **4**) *Direct energy deposition*; expel and fuse material directly upon the part. **5**) *Sheet lamination*; sheets of material are flushed and subsequently altered using subtractive manufacturing. **6**) *Vat polymerization*; using a pattern of light to cure consecutive layers of resin, a liquid photocrosslinkable material.

These techniques provide the highest special accuracy into the 10's to 100's of *n*m-range. [10] However, the process throughput is limited due to the time-consuming bioink curing, a result of both the chemical stabilisation process and limit on light energy exposure per voxel for a certain duration regarding cell viability, coupled with the highly confined region of polymerization to maintain accuracy. [10] Additionally, only a single type of bioink can be cured from a relatively large bulk at a time, requiring resin replacement to allow more compositional complexity which is also time-consuming and potentially quite wasteful on bioink components. [10]

Of most interest to tissue engineering is the 3Dbioprinting method of **7**) *material extrusion*, in which a material, regularly called a bioink, is extruded and deposited on a build platform, upon a previously deposited layer, or inside a supporting bath, also known as an embedding bath. The bioink may contain living cells, biomaterials, or active biomolecules, and may function in a structural or sacrificial manner. [15]

Compared to the previously mentioned methods, the conditions necessary for stable structure formation, such as temperature, pH or ultraviolet (UV)-exposure, are generally more gentle on the potentially incorporated cells, gels or biological molecules.

Different combinations of biomaterials or bioinks can be extruded simultaneously or in quick succession by using setups consisting of multiple containers feeding either an

array or the same nozzle, increasing throughput and design possibilities. [10], [19], [20]
Piston driven robotic dispensing generally provides more volumetric flow control compared to pneumatic systems, where gas compression acts as a spring. Screw-based systems also provide good control and are more suitable for high-viscosity liquids. [21]
3D-bioprinting can be sub-divided in *scaffold-free* methods; in which only cells, often in a spheroid, cell sheet or tissue strand formation, are used as building blocks, and the *scaffold-based* methods; in which a support structure or medium is employed to support, suspend, or retain the cells directly or uses as a cell-laden bioink. [22]
Scaffold-free bioinks are promising for tissue fabrication because they are essentially cell aggregates. Being inherently completely biological provides excellent biocompatibility, harbouring a high cell density, while also facilitate ECM-deposition and a high-degree of intracellular interactions. [15] The absence of scaffolds allows for cell migration which induces rapid differentiation and maturation, preserve healthy cell function, viability, maturity, and increase ECM-production resulting in good biomimicry. [23]-[26] Using specific geometric retaining platforms, patterned structures can be fabricated without additional support. [27] Additionally the introduction and subsequent removal of potential non-biological components is not required, which besides reduces predure complexity, can also be beneficial if these tissue constructs are to be implanted.
However, 3D-printing development primarily focused on counteracting instabilities which have two main sources, a) surface tension; which minimizes surface area, directing geometries to become more spherical or spread geometries depending on internal forces, and contact surface wettability, and b) body forces; gravity-induces sacking or buckling. [28] The overall low mechanical stability and high wettability of bioinks challenges shape fidelity and presents difficulty to form large structures without using (sacrificial) supports and active perfusion. [28] Additional drawbacks also include low throughput and time-consuming pre-print preparations, imposing relatively high costs, both limiting scalability and the use of large constructs as building units (e.g. spheroids and strands) also restrict resolution. [23], [24] Aqueous cell suspension also possess limited control guiding cell positions, resulting often in heterogenous concentrations, limited control over final architecture and reorganisation, and thus shape retention as well as local cell ratios, when seeding multiple cell types. [22]–[24]

The scaffold-based approaches, which are used most commonly in TE, can be us to partially resolve these issues. [29] It is promising for its high versatility in available building materials, good shape fidelity, variable and tuneable mechanical properties, degradation profiles, surface chemistry, and chemical release profile. [22] Scaffolding material can be employed to support and/or retain bioink before additional stabilization can be performed.

A common approach is to use a material formed by an liquid-absorbing but non-dissolving long chain polymer networks, called a hydrogel, which can be formed in the presence of cells for their encapsulation, can be used as a building material, distributing cells homogenously throughout a construct while it can be tuned to mimic the *in vivo* environment, using for example extracellular matrix (ECM)-mimicking (e.g. denatured collagen; gelatin) or decellularized-ECM (dECM)-based hydrogels. [20], [30]–[33]
Their properties, including rheology; viscosity, non-Newtonian thixotropic shear-thinning behaviour, and post-shear recovery speeds as well as surface tension, swelling properties, and gelation kinetics, can be tuned to enable good printing fidelity, forming a highly useful and versatile group of materials. [29], [34] Although useful for seeding stable structures at low viscosity, they exhibit comparable issues as cell-only bioinks regarding their mechanical properties, insufficient for some stable tissue formation when non-supported. [35]
Thus, the use of hydrogel is often combined with the incorporation of stabilisation methods implemented during and/or after printing, which can be temporary or permanent, including the introduction of scaffolding or a plethora of crosslinking mechanics or temperature and concentration dependent phase changing materials. [15], [35] Stabilisation methods might include ionic polymerisation, for example; gelation of biocompatible polysaccharide alginate, which can also be reversed by the addition of sufficient monovalent ions or chelation agents. [20], [36], [37]
Enzymatic crosslinking, where for example transglutaminase crosslinks protein based gels like gelatin. [35], [38]
Photo-crosslinking, either by use of photo initiators (PIs), PEGTA, or UV-crosslinkable methacrylate (MA) groups, which can also be modified to other gel like gelatin (GelMA), or hyaluronic acid (MeHA). [33], [35], [39]
Temperature changes can also lead to phase transition, for example Pluronic F127 (PF127) liquifies at low temperatures while gelatin undergoes gelation at lower temperatures. [35] Collagen and pepsinized ECM on the contrary, self-assembly into hydrogel when the temperature and pH are elevated, often used as a quick temporary stabilization before additional stabilization is subsequently employed. [40], [41]
Scaffolding material, often an acellular, biocompatible substance, can be a printed support; either intra-structurally; alongside or within the construct, or printed extra-structurally; surrounding the construct acting as a container or supporting manner. [35] An example of intra-structural support is the deposition of temperature-controlled self-assembling dECM, used as a scaffold between which cell-laden (hydrogel) bioink is deposited and possibly cured. Not only can the cells environment be tai-

lored by harvesting dECM form specific tissues, also the tuneable stiffness offers control on the construct's geometry and compositional and mechanical properties. [32], [42] Instead of acting as permanent scaffold, intra-structural support can also be employed in a sacrificial (fugitive) manner, especially towards the creation of overhanging (e.g. hollow) structures, which can be achieved by manual, enzymatic or thermal removal of the support. [38], [42], [43] This strategy is suitable for capillary formation and active perfusion, overcoming nutrient diffusion limitation inherent to increasingly larger and denser tissues. [35]

The most common bioink stabilisation strategy is the use of a pre-cast supporting (embedding) bath. Where the bioink is extruded into material that typically behaves like a Bingham pseudoplastic, exhibiting rheological viscoelastic thixotropic (shear-thinning) properties. Shear stresses, resulting from a traveling needle or flowing ink, locally yields (liquifies) this scaffold, allowing for ink deposition and needle movement with minimal influence on its surroundings. When the shear stress source is removed scaffold re-solidification captures the printed structure, which can subsequently be followed by bioink stabilisation or the stabilisation of the support. [35]
Because the bioink is immediately surrounded upon extrusion, a plethora of different secondary stabilizing methods, applicable for both the bioink and supporting material, can be readily employed. Using for example $CaCl_2$ crosslinking of alginate hydrogel, HEPES for collagen acidification, leading to self-assembly, or photocrosslinking MA groups, which can all also be used in multiplex. [20] Its stiffness can be regulated pre-, during and post-print, tuning printing resolution, printing continuity, coalescence between filaments, and support removal. [44] Although the vast majority of embedding baths are water based, oil-based is also possible, allowing for the printing of hydrophobic materials (e.g. silicone). [45] Some embedding bath rheologies exhibit slow recovery speeds, which may result in insufficient ink retention due to the persistence of a vertical crevice in the needle's wake. One solution is the addition of a filler liquid on top, possessing a Newtonian flow behaviour, negligible shear elastic modulus, and low viscosity, which rapidly fills this cavity, essentially acting as a plug. This however also introduces heterogeneity in the supporting medium, reducing shape fidelity, homogeneity of the bioink's distribution, and hinders the printing of successive layers. [46], [47]
Sacrificial supports can be removed enzymatically; with, for example, the addition of alginate lyase to alginate microparticle support, thermally; using gelatin melting at incubating temperatures, or for embedding baths comprising dilutable support like xanthan gum (XG)-hydrogel, simple submersion may be sufficient for printed construct retrieval. [20], [48], [49] An example of sacrificial bioink is the use of modified hyaluronic acid (HA) hydrogel, which captures the ink in the manner described above, and is subsequently stabilized by photocrosslinking with UV, allowing the previously deposited ink to be sucked or pushed out and forming channels with an inner diameter ($\emptyset_{ID}$) down to at least 35 μm. [39] Hollow channels can also be seeded with cells, for example human umbilical vein endothelial cells (HUVECs), recreating vasculature. [50] The support itself may also act as the cell-carrier, for example; cell-laden methacrylated XG (XGMA) support, supplemented with $CaCl_2$ for alginate hydrogel bioink crosslinking, is photocrosslinked after alginate filament stabilization. Subsequent liquification of the alginate hydrogel provides a perfusable cell-laden hydrogel. [37]
The bioink and embedding bath can be comprised of similar materials such as PF127 solution, printed in a photocrosslinkable PF127 diacrylate (F127-DA) solution, both exhibiting shear-thinning behaviour. [46]

A very promising and already widely used embedding bath method is a supporting comprising a dense suspension of hydrogel microparticles. In the so called freeform reversible embedding of suspended hydrogels (FRESH) method a granular bath is centrifuged, reducing less inter-particle (interstitial) liquid, resulting in and their jammed state. This behaves like a non-Newtonian shear-thinning liquid in much the same manner as previously described. [51], [52] The bulk yield stress material can be comprised of numerous materials, even cell spheroids, tailored to achieve desired printing objectives and non-destructive print release methods. [52] A great number of secondary stabilisation methods can be integrated into the liquid phase, while most baths are also translucent, useful for monitoring and potential photocuring. [20], [51], [52] Very high-resolution filaments can be printed down to 20 μm, for example using blended crosslinked gelatin slurry. [20], [49]
The presence of low viscosity Newtonian fluids in the interstitial space does however require tight packing to allow for jamming transitions required for stable ink retention and high print fidelity. Self-healing annealable particle-extracellular matrix (SHAPE) printing platform attempt to improve upon this using a lower hydrogel phase concentration (70%) mixed with a viscous polymer solution (30%). [53] Similarly, the use of alginate-XG hydrogel has also been demonstrated, which forms a particulate hybrid medium with shear-thinning properties by mixing internally crosslinked and blended alginate with a XG. [41]

When cellular self-reorganisation abilities are sufficient, embedding baths may allow for spontaneous structural conformational changes. For example printing an aqueous high-cell density culture medium suspension (50×10^6 cells/mL), bioink in an embedding bath made from collagen I, Matrigel or a mix thereof, cells were able to reorganize and reposition relative to each other into mechanically stable strand or, when exposed to the appropriate growth factors (GFs), perusable tubes. [54] Similarly, an

embedding bath made from photocrosslinkable oxidized methacrylated alginate (OMA) allowed the printing and culture of mm-scale tissues using essentially centrifugally made cell pellets as bioink, which however showed very poor print fidelity. [55] A very high cell density bioink (3×10^8 cells/mL) was successfully printed in the FRESH 2.0 platform, however this was extruded in a 450 μm gap between previously printed collagen and was combined with a thrombin induced polymerization of the bioink's fibrinogen. [20]

Besides high cell-density bioinks, (jammed) hydrogel embedding baths and bioink exhibit low viscosity and mechanical integrity before secondary stabilization, and struggle to provide stability at material boundaries. [25], [36] Secondary stabilization methods might also not act fast enough, or they cannot be implemented at crucial steps during bioprinting process. [25]

Although good special resolution has been achieved, with features down to 35 and 20 μm, with and within hydrogel (particle) cell-free suspensions, these can only be reliably achieved with nozzles of similarly diameters. [20], [39] Extrusion through tubes or orifices of these dimension at speeds necessary for regular printing are likely to induce shear stresses detrimental to particles integrity or cell function. [10], [56] Increasing nozzle sizes will allow more gentle extrusion of viscous, high cell-density bioinks at higher extrusion rates, at the cost of lower resolution, especially compared to the patterned and highly organised structures characteristic and crucial to functional tissues, making this a less than ideal solution to complex tissue fabrication.

These negative effects associated with high-viscosity suspensions must be balanced with the aim of printing functional and stable tissue constructs, often requiring a high degree of compaction, commonly resulting from high initial cell-densities. However, high particle (e.g. cells) volume fractions (φ_p) increases the viscosity of the suspension. [57], [58] Which makes them prone to clogging events and irregular extrusion, either by the formation of particulate accumulations, or the forming of jammed states (arches), which is partially dependent on the ratio between particle size and orifice size (needle size/gauge). [12], [21], [59], [60]

Although capable of providing a sufficiently long-term culture environment, the presence of intercellular hydrogels combined with the lack of cellular binding sites, often limits or even prevents cell motility, and consequently, cellular remodelling and the formation of high degrees of cell-to-cell contact, beneficial for desired cell function, differentiation, and proliferation. [25], [26] This issue can be partially overcome by the use of alternative hydrogels or modifications, such as sulphate groups to alginate, which greatly increase cell motility and proliferation, yet intercellular hydrogel remains abundant. [61] However, the hydrogels' mechanical properties suitable to form stable, self-supporting structures often greatly limit cell movement, cell-organisation, and their removal without structural deterioration. [34]

In this thesis, a novel extrusion 3D-bioprinting platform is introduced which aims to combine the benefits of allowing high degrees of cell motility and intracellular contact from very high cell density environment with the low shear inducing printing of dilute aqueous cell suspensions.

The bioink comprises a particle (cell) suspended at volume fractions (σ_p) from 5 to 15% in a liquid expressing rheological properties and viscosities of water during extrusion, introducing minimal shear forces. The carrier fluid may only comprise cell-specific culture medium together with a density modifier, used for retaining suspension homogeneity during printing operations. This cheap and easy to use bioink permits free particle movement while being tuneable both in density, biochemical makeup, particle concentration and the particles' compositions.

This Newtonian particle suspension is printed in a non-Newtonian thixotropic (shear-thinning) embedding bath made from the well-known, inexpensive and versatile XG hydrogel, acting as an extra-structural and sacrificial scaffold, which is biocompatible and presenting few binding sites when unmodified, preventing cell adhesion. [62], [63]

In combination with water-based bioinks, XG-based hydrogels spontaneously exhibit a mechanism, not explicitly described and utilized in detail in 3D-bioprinting literature, capable of greatly increasing local particle densities. By allowing the bioink's carrier liquid to flow and/or diffuse radially into the surrounding bath, particles are locally condensed by both increasingly less interstitial liquid and an encroaching, swelling hydrogel matrix.

Due the gradual and radial particle condensation, features significantly smaller than needle gauges, can be reliably formed.

This mechanism, which can be considered a passive secondary stabilisation method, does not negatively influence cell function and leaves little to no interstitial hydrogel. Printing bioinks containing only cells, or combined with particles harbouring cell binding sites, result in mechanically stable fibre tissue constructs after a short culture, without the need of additional stabilisation methods.

They show healthy tissue functions such as proliferation, spontaneous contraction from cardiac cells, cytoskeletal alignment, high degrees of cellular reorganisation, and the ability to be remain intact during physical manipulation.

To show versatility and compatibility bioinks comprising microparticles, cell spheroids, hydrogel microbeads, pigments, dyes, multiple cell types and combinations thereof are used, which demonstrate highly specific and controlled tissue engineering potential. [64]

Release of printed construct can be simply achieved by increment hydrogel dilution.

1.1 Disclaimer on a selection of results presented

Parallel to the experiments presented in this thesis, close-up and in-depth analyses on the hydrodynamic behaviour aqueous Newtonian fluids or suspension in viscous Newtonian and non-Newtonian hydrogel embedding baths. These experiments were independently carried out by V. Trikalitis and M. Kaya in a custom-made imaging setup. The part of their results and findings were presented in the premier article Trikalitis *et al*. (2023) on this 3D-bioprinting platform, of which the author of this Thesis was a co-author. [65] A selection of their data, and the figures and images based upon them, was kindly provided to be used in this Thesis for helping to provide an improved understanding on key bioprinting platform characteristics. This data, for which the author does not claim any credit, will be clearly marked.

1.2 Structure of this report

In the next **Chapter 2 Theory** the chemical structure of XG hydrogels are discussed and rheological properties this generates (**§2.1**). This is followed by an analysis of shear forces generated which can be expected when extruding aqueous and dilute bioinks and their effect on cell viability (**§2.2**).
In the following paragraph (**§2.3**) the flow characteristics of an aqueous Newtonian ink trough a XG hydrogel embedding bath are explored using data and visualizations sourced both from own experiments as well as from close-up and in-depth analyses, performed by V. Trikalitis and M. Kaya. [65] Based on this data, the novel diffusion packing mechanism is introduced using, among other things, videos captured by Trikalitis and Kaya (**§2.4**). Finally, the function, need and method of the modifying the ink density is illustrated (**§2.5**).

In **Chapter 3 Materials and Methods** the composition of culture media, bioinks and XG embedding baths are reported, together with the workflows for their preparation and use in the bioprinting process, together with the protocols followed for cell-, spheroid- and post- printing cultures. Lastly the fixation, staining and imaging of tissue samples with the aim of exploring tissue structure and function are discussed.

Chapter 4 Platform Optimization delves into the preliminary exploration of platform potential with the aim of finding characteristic functions and inherent limitations for increasing performance. Here the reasoning behind the currently used embedding baths and bioinks compositions are explained. Followed by an elaboration on the effects of different needle architectures, both in size and overall shape, together with those of different feed rates (volume/time), infill values (particle volume/distance), and needle movements through the bath, the data for which was partially produced by the efforts of V. Trikalitis and M. Kaya. [65] Post-print culture and extraction techniques are briefly discussed as well.

In **Chapter 5 Results** the most relevant results regarding deposition, tissue formation, tissue functioning, culture and extraction of printing cell-, spheroid- and particle-laden bioinks and combinations thereof are shown.
The result of printing non-biological ink comprising suspension of particles in 3 broad size ranges of small; pigments, medium; μparticles and large; hydrogels, are also shown.

These results and the subsequent possibilities and limitations these results seems to indicate are addressed in **Chapter 6 Discussion** together with some observed discrepancies. Promising and curious but non-replicable result from initial experiments showing peculiar bath performance with alternative needle geometries are also shown and discussed.

The most important outcomes from preceding chapters are then summarized and concluded **Chapter 7 Conclusion**.

Finally a selection of ideas for potential for platform performance improvements and evaluations are suggested **Chapter 8 Future Outlook**.

Chapter 2. Theory

2.1 Xanthan Gum hydrogel

Gums are polysaccharides which have a high affinity for water and in solution are able to increase its viscosity, even at low concentrations. [62] Xanthan Gum is a biocompatible branched polysaccharide produced through fermentation by the Gram-negative bacteria of the genus *Xanthomonas*, with *X. Campestris* used commercially. Long-established and widely used in the food and cosmetic industries, mostly as a thickening agent, due to its biocompatibility, enzymatic resistance, cytocompatibility, pH and temperature stable rheological properties, and chemical modification capacity, its potential role biomedical applications such as tissue engineering has been expanding recently. [66], [67] In **Fig. 1** its chemical structure is depicted, showing a linear pentasaccharide backbone with mannose side chains. [62] The acetyl and pyruvyl residue prevalence and distribution along the chain, which varies with bacterial species and fermentation broth conditions, influence the behaviour of XG aqueous solution. [66]

The average molecular weight ranges between 1×10^6 to 20×10^6 mol/g. The terminal mannose moiety in the side chain is partially substituted with a pyruvate residue, which is deprotonated at pH > 4.5, allowing Ca^{2+} mediated physical crosslinking, while the proximal mannose is acetylated. [62], [66], [68].
The rheological properties of XG are well understood for a wide number of ranges and solvent conditions, notably ionic strengths, and pH values. Compared to other polysaccharide gums the shear-dependent viscosity changes are more pronounced, hypothesised of being a result of the alignment of XG chains, between which no chemical bonds form in the absence of ions (**Fig. 1.C**). The aquatic crystalline hydrogel matrix is composed of the randomly intertwined secondary right-handed double helical XG chain structures. This is further stabilized by intermolecular and intramolecular hydrogen bonds, electrostatic interactions and steric hinderance between the chains. [67], [69] These rod-like configuration realigns more easily when exposed to shear forces above its yield stress, compared to the random helical configuration characteristic of other polysaccharide hydrogel matrixes, resulting in a decrease in viscosity until it recovers. [67], [70], [71] The recovery time after applying a shear stress greater than the yield stress, (outside the linear viscoelastic region (LVER)), is inversely proportional to the zero-shear viscosity and thus XG concentration. [72]
The chains can form physical networks in aquatic solutions with the use of cations, e.g. Ca^{2+}, Me^{2+} and Pb^{2+}, binding stronger with heavier metal ions (**Fig. 1.B**). [62] A decreased viscosity and shear thinning behaviour, can be seen by the addition of cations due to; 1) side chain moving towards the cellulose backbone and subsequent reduction in average hydrodynamic radius allows easier alignment when experiencing shear and 2) the loss in the ability to undergo shear-induced conformational changes by internally linked polysaccharide chain. In this complex the pyruvate residues on the terminal moiety are the principal binding site for the cations, due to them possessing a negative charge and experiencing the least steric hindrance. The polysaccharide main chain and *O*-acetyl group on the side chain are minimally involved. [63]

Apart from having the potential to possess non-Newtonian rheological shear thinning properties useful for 3D embedded printing while acting as a carrier of crosslinking compounds for ink stabilization, unmodified XG is biocompatible which allows tissue formation with minimal interaction with material the printing platform utilizes. It can however be functionalized with for example the crafting of amino acids to the G chains using citric acid (CA) or etherification, esterification, oxidation, acetalation and amidation for pharmaceutical and biomedical use. [62],[68],[73]

As mentioned in the **Introduction,** XG has been used in a plethora of supporting materials, mostly combinated with stability enhancing additives, such as $CaCl_2$ for alginate bioink crosslinking, or cell-laden XGMA for UV crosslinking of the support itself, leading to stable, viable, and high cell density encapsulation. [37] A noted benefit of using a XG-only based support is allowing for construct retrieval using simple submergence. [37] It has also been used as a rheological optimizer in extrusion printing self-supporting sodium alginate (SA) inks. [74]

Although widely used in the pharmaceutical industry, foodstuffs, and field of oil recovery, XG-based hydrogels as scaffolds have been underexplored in current 3D-bioprinting, especially as its sole hydrogel-forming component and omitting secondary stabilisation methods. Although well-known rheological properties are promising, its potential sensitivity to culture media components has currently not been researched and demands for comprehensive studies out of the scope of this research. However, being relatively inexpensive, biocompatible, possible to incorporate many different culture media, no need of stabilisation methods, and the potential for easy removal indicate potential for an extended role in 3D bioprinting scaffolding.

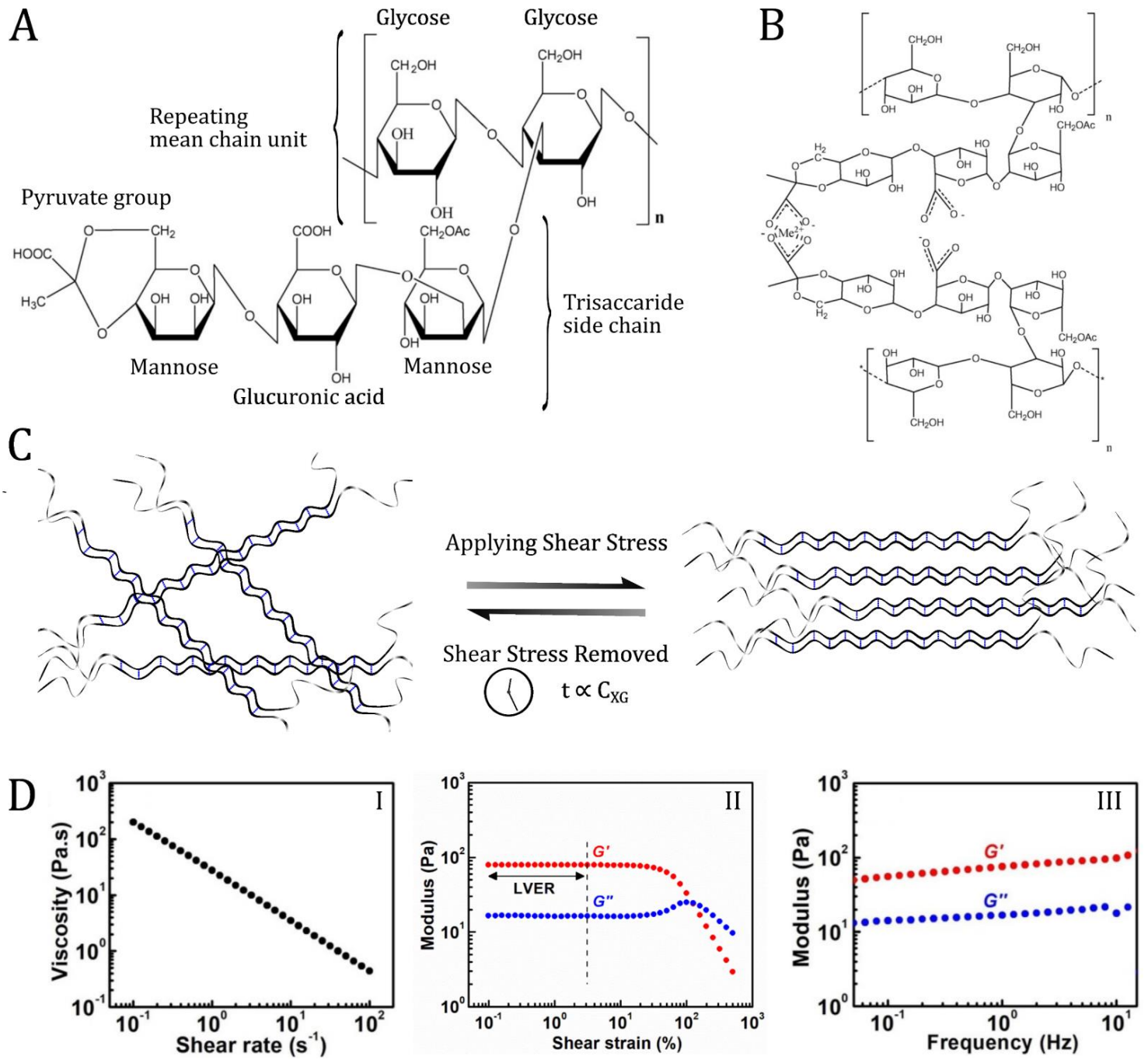

Figure 1. A) Haworth projection of XG with its trisaccharide side chain connected to alternate glycose unites forming the backbone. [63] The pyruvate group on the terminal mannose moiety is depicted, which are normally partially deprotonated. Often an acetyl group (Ac) is substituted, by way of an esterification, to the internal mannose, forming an O-Acetyl functional group (acetoxy group). **B**) Schematic representation of XG complex formed by the ionic binding of deprotonation pyruvate to a bivalent cation. [63] **C**) Without applying shear, the crystalline hydrogel matrix is a random distribution of XG chains bound by inter-and intramolecular hydrogen bonds (blue dashed lines). When shear is applied above its yield stress, double helical rod-like structures align and the viscosity decreases. Recovery time to regain zero-shear conditions is proportional to the XG concentration. [67] **D**) Rheological properties of 1.5% (w/v) XG in distilled water supplemented 50 mM $CaCl_2$: (**I**) Viscosity decrease with increasing shear rate, characteristic for non-Newtonian shear-thinning behaviour. (**II**) Storage modulus (G') and elastic modulus (G'') against shear strain (deformation %) showing a LVER up to a strain of 3% and a transition from a gel-like state to liquid-like state at ±126%. (**III**) Relatively stable moduli against a frequency sweep at 3% strain (within the LVER). [37]

2.2 Ink properties

In a system where a particle suspension is flows through an orifice it has been found that the system geometry, comprised of the *neck-to-particle* diameter ratio (D/d) and constriction angle, can be regarded as a good indicator when to expect a transition from uninterrupted flow to an intermittent or clogged state. [59]
The effects of colloidal particle interactions, Brownian motion, intra-particle, particle-wall interactions are kept minimal and constant, however the effect of φ_p is not clearly addressed. [59]
Because this platform setup utilises standardised needles, keeping the internal geometry consistent, a maximum limit on φ_p and particle sizes are automatically imposed. However, if interparticle interaction are excluded and the suspension is regarded as homogeneous during the printing period, something that will be discussed in **§2.5**, all used bioinks can be regarded as dilute. Thus, all irregular flow behaviour that could be observed will be the result of either embedding bath characteristics or due to particle precipitation and/or coagulation.

2.2.1 Fluid wall shear stress

When extruded through a channel, like a needle, fluid and particles suspended within will experience a shear stress which is highest at the channel's walls. In addition to the previously mentioned flow characteristics, these forces are crucial to determine bioink rheology, suspended particle integrity, cell viability and possible differentiation ques. [75], [76]
The bioinks cellular components volume is regarded as comprising a homogeneous collection of spherical and dissociated particles of predetermined average diameter, multiplied by their population. The φ_p was ≤ 0.1 for almost all bioinks used in these experiments, which is lower than the $\varphi_p \approx 0.3$ threshold at which viscoelastic behaviour can be expected for spherical particles with minimal mutual binding affinity, which can be attributed to some dense cells suspensions. [57], [58]
The addition of the polymer-like crystal colloid structure of fetal bovine serum (FBS), which itself is highly non-Newtonian, have been shown to contribute to shear-thinning behaviour in solution. [77] At $\varphi_p = 1\times10^{-3}$, spherical viable cells do increase viscosity and viscoelastic behaviour as well, although to a lesser extent than FBS. When combined these rheological parameters do decrease more than FBS-only. [77] Because the liquid component of the bioink used in this research comprises mostly cell medium at >70% (v/v), which is made from 10-20% (v/v) FBS, the bioink is expected to undergo some shear thinning during printing. The calculations of shear forces must therefore incorporate a shear rate dependent factor.

For calculating the shear stress first, it must be shown that the fluid flow can be considered laminar by calculating the dimensionless Reynolds number (Re). [78], [79]

$$Re = \frac{\rho_{ink} \times \emptyset_{ID}^{n} \times u_{avr}^{2-n}}{8^{n-1} \times K}\left(\frac{n}{a+bn}\right)^{n} \qquad \textbf{Eq. 1}$$

In which ρ_{ink} is the bioink's density [kg/m^3], $\emptyset_{ID}$ the hydraulic diameter, identical to the needle's inner diameter [m], u_{avr} is the average flow speed [m/s], see **Eq. 6**. a and b correspond to properties of the flow channel geometry and are 0.25 and 0.75 respectively for a pipe of circular cross-section. The variables K is the flow consistency index [Pa s^n], and n the flow behaviour index [-], which is < 1 for pseudoplastic fluids. The flow is regarded is laminar if Re < 2100.
The shear stress τ_{wall} [Pa] produced and experienced by a non-Newtonian fluid in a hydrodynamic system is highest at the channel's wall. It can be calculated when assuming the fluid properties can be expressed mathematically as being depended on shear rate. For laminar flow of non-Newtonian fluids methods one can assume the fluid to follow the *Power-Law*, also known as *Herschel-Bulkley Law*, which states: [77]

$$\tau_{wall} = \tau_0 + K\left(\frac{\partial u}{\partial y}\right)^{n} \qquad \textbf{Eq. 2}$$

In which $\left(\frac{\partial u}{\partial y}\right)$ is the shear rate [s^{-1}], also depicted as γ, and n, here also called the power-law index [-]. K and n can be obtain from experimental rheological data by calculating $\log(\mu_{eff})$ and $\log(\gamma)$ respectively. Of note is the restraint on these indexes which is that they are only approximations whose accuracy is dependent on the experimental data, and they can only predict rheological properties accurately in and around the range of parameters (e.g. shear rates) used in the experiments from which their values were derived. τ_0 is the yield stress [Pa], the point at which applied stress breaks up the existing network and the suspension start flowing viscously. Shown to be negatable at φ_p < 0.45 for spherical particles and only slightly larger with dense cell suspensions. [57], [58] Because the φ_p of the bioink will not exceed 0.1, this parameter will not be taken into account.
Non-Newtonian flow through a circular cross-section can be calculated using the generalized Poiseuille equation:

$$\left(\frac{\partial v}{\partial r}\right)^{n} = \frac{r\gamma_0^{n-1}}{2\mu_0}\frac{\partial P}{\partial z} \qquad \textbf{Eq. 3}$$

Where μ_0 the limited viscosity at low shear rate γ_0, and ∂P the pressure drop over the path length ∂z $[m]$.

The effective fluid dynamic viscosity μ_{eff} [Pa s] can be calculated using the power-law assumptions using **Eq. 4**.

$$\mu_{eff} = \mu_\infty + K\left(\frac{\partial u}{\partial y}\right)^{n-1} = \mu_\infty + K\gamma^{n-1} \qquad \textbf{Eq. 4}$$

Being an approximation, if $n < 1$ the equation predicts $\mu_{eff} \to 0$ as $\gamma \to \infty$, which is impossible. Therefor the μ_∞ is introduced as viscosity at $\gamma \to \infty$.
Assuming the setup to extrude a set volume in a constant manner, thus regardless of resistance and disregarding startup time, the fluid flux Q [m^3/s] needed to deposit a cylindrical ink column can be calculated using as follows:

$$Q = L_{path} * A_{ID} = L_{path} * \left(\frac{\emptyset_{OD}}{2}\right)^2 * \pi \qquad \textbf{Eq. 5}$$

In which L_{path} is the length $[m]$, determined by the build platform movement. From which the average velocity u_{avr} through a tube with diameter $\emptyset_{ID}$ can be calculated.

$$u_{avr} = \frac{Q}{A_{ID}} = \frac{Q}{\left(\frac{\emptyset_{ID}}{2}\right)^2 * \pi} \qquad \textbf{Eq. 6}$$

This Q is identical to the Q through the needle which can be calculated integrating speed from **Eq. 3** over the cross-sectional area with no-slip boundary conditions as follows: [80]

$$Q = \left(\frac{n}{3n+1}\right)\pi\gamma_0\frac{n-1}{n}\left(\frac{\partial P/\partial z}{2\mu_0}\right)R^{\frac{3n+1}{n}} \qquad \textbf{Eq. 7}$$

Where the channel radius R = $\emptyset_{ID}/2$.

Using the fluid flux through a tube with inner diameter $\emptyset_{ID}$ and assuming power-law approximations τ_{wall} can be calculated: [80]

$$\tau_{wall} = K\left(\frac{8 \times Q}{\pi \times \emptyset_{ID}^3}\right)^n \qquad \textbf{Eq. 8}$$

Which forms into the following equation if **Eq. 7** is substituted in **Eq. 8**

$$\frac{\partial P}{\partial z} = \frac{\tau_{wall}}{\left(\frac{n}{3n+1}\right)^n}\left(\frac{4}{\emptyset_{ID}}\right) \qquad \textbf{Eq. 9}$$

Which gives the following relation as well

$$\Delta P = \frac{\tau_{wall}}{\left(\frac{n}{3n+1}\right)^n}\left(\frac{4 \times L_{chan}}{\emptyset_{ID}}\right) \qquad \textbf{Eq. 10}$$

Where L_{chan} is the needle's channel length.

There is off course no line-up of needles with continuous $\emptyset_{OD}$ and $\emptyset_{ID}$. However, taking the product range of needle gauges supplied by NeedlEZ, the manufacture used in this research, a trendline can be fitted which gives an estimate of a $\emptyset_{ID}$ for every $\emptyset_{OD}$ and *vice versa*. [81]

The because the u_{avr} decreases proportionally faster with an increasing $\emptyset_{ID}$, the Re increases with a decrease in needle dimensions, and thus an increase in needle gauge.
The most turbulent bioink flow can therefore be expected at the smallest gauge. In this research 90° bend needle gauges are used of sizes G23 (406 μm $\emptyset_{ID}$, 635 μm $\emptyset_{OD}$), G26 (279 μm $\emptyset_{ID}$, 483 μm $\emptyset_{OD}$) and G27 (229 μm $\emptyset_{ID}$, 406 μm $\emptyset_{OD}$), all of length L_{chan} 40 mm. [81]
When calculation for maximal fluid flow, the Re comes to ± 2.8 × 10^1, situated below the 2100 threshold for turbulent flow for G27, and even smaller needle, like G30 (152 μm $\emptyset_{ID}$, 305 μm $\emptyset_{OD}$) all, will produce Re far below this threshold at ± 4.5 × 10^1. The flow through the needles can be regarded as laminar for all cases discussed here.
Of most interest in τ_{max}, which is achieved at the highest extrusion rate. The current setup has an upper extrusion limit at which print fidelity is compromised, later discussed in **§2.3**. This limit is both a product of 1) the maximum movements speed of the printer's build platform at 20 mm/s, which gives Q_{max} over L_{path}, and 2) the maximum diameter of the extruded ink column, which is equal to the needle's $\emptyset_{OD}$ used. This Q_{max} which when implemented in **Eq. 8** will give the maximum τ_{wall} for a flow through a needle with $\emptyset_{ID}$.
The values for K = 34.35 ± 024 mPa s^n and n = 0.138 ± 0.003 were derived by Wyma *et al*. (2018) for a L929 cell suspension of 1.991×10^6 cells/mL (φ_p = 0.001) and 10% FBS at D5. [77] From **Eq. 8** the graphs depicted in **Fig. 2.A** & **2.C** can be produced, while **Eq. 8** gives **Fig. 2.B**.

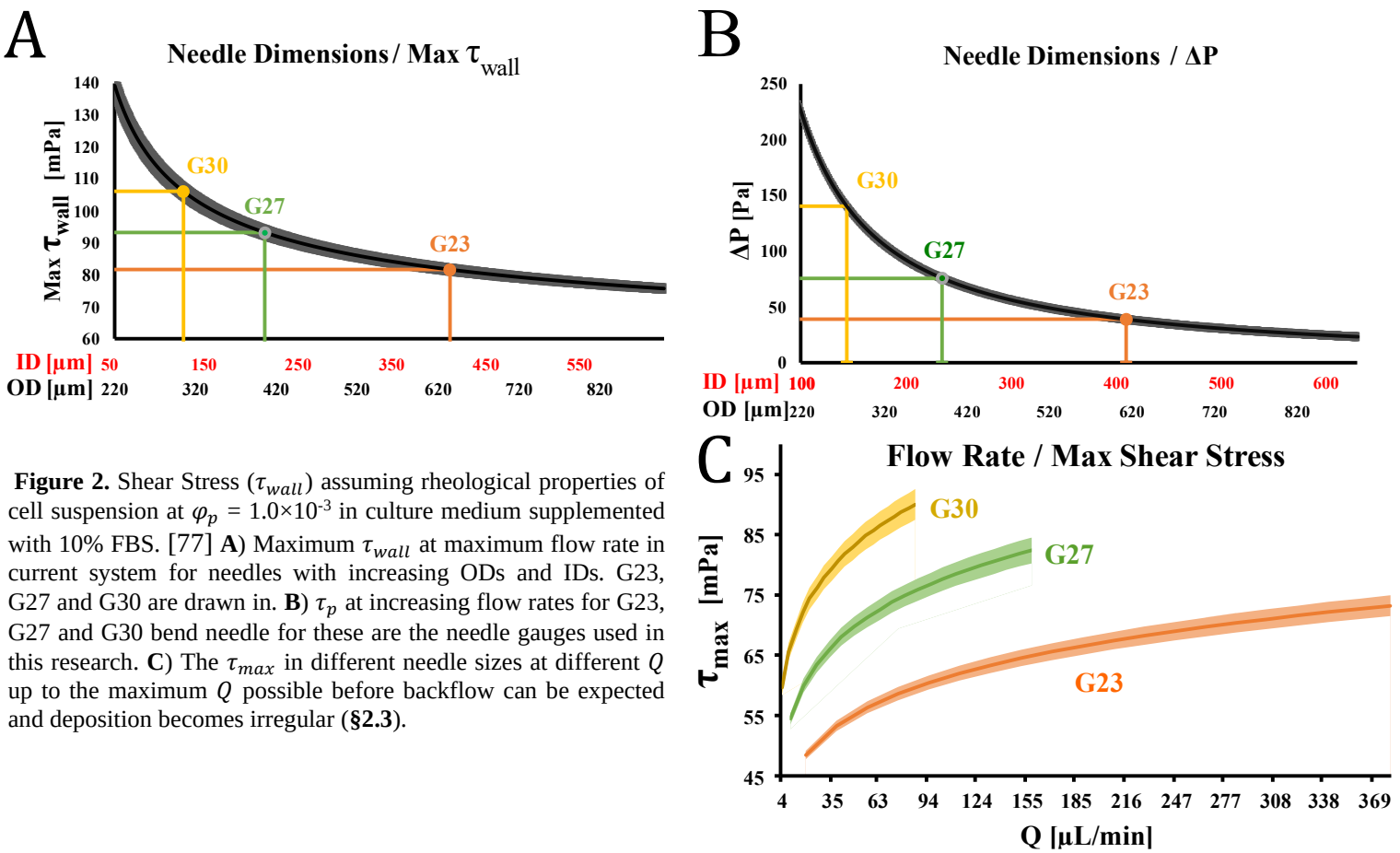

Figure 2. Shear Stress (τ_{wall}) assuming rheological properties of cell suspension at φ_p = 1.0×10^{-3} in culture medium supplemented with 10% FBS. [77] **A**) Maximum τ_{wall} at maximum flow rate in current system for needles with increasing ODs and IDs. G23, G27 and G30 are drawn in. **B**) τ_p at increasing flow rates for G23, G27 and G30 bend needle for these are the needle gauges used in this research. **C**) The τ_{max} in different needle sizes at different Q up to the maximum Q possible before backflow can be expected and deposition becomes irregular (**§2.3**).

2.2.1.1 Shear rate dependent cell viability

The relatively high pressures generated during printing might cause cell damage and reduce cell viability. [26], [75], [80]

Extrusion based cell viability study which correlate printing pressure to cell viability finds a reduction of 38.75% live cells, printing bioink containing 1.5% (v/v) alginate and 1×10^6 cells/mL, when printed with a dispensing pressure of 28×10 kPa (40 psi) compared to 34 kPa (5 psi). [80]

Exponential decrease in live cells was observed with a viability decrease of 10% at 20 kPa to 60% at 120 kPa. These dispensing pressures are far higher than those generated in the extrusion system used in this research; ΔP of ±65 Pa at Q_{max} of ±1.5 μL/s and u_{avr} of ±8 cm/s with the smallest size needle generating τ_{max} of 90 mPa (1.3×10^{-5} psi) in the smallest G30; **Fig. 2.B**.

Shear stresses <5 kPa, obtained at average flow velocity in multiple m/s, had almost no effect on cell viability in a study with high cell density (10^6 C/mL) in 0.5% (v/v) alginate bioink with L929 Mouse Fibroblast cells. [75]

Cell damage assays with 3T3 and Schwann cells at 1 × 10^6 cells/mL in 5% alginate have shown slight cellular damage ±5% at flowrates as low as 2.5 × 10^{-3} mL/s in 250 μm needle (G25). Although this flow rate is slightly lower compared to the maximal flow rate calculated for G25 in the current setup, the bioink viscosity was about 1000-fold higher and is far more share rate dependent (n ±4 orders of magnitude larger). [56]

Constructs from very high density cell-only bioinks composed of either pelleted human mesenchymal stem cells (hMSCs), human adipose-derived stem cells (hASCs) or human dermal fibroblasts (hDFs) printed in a shear-thinning microgel embedding bath showed very high viability, even after UV photocuring. [55]

Because the cell densities and bioink rheology have not been shown in theory to induce shear stresses significantly harmful to cell viability, compared to the aforementioned studies, no detrimental effected regarding to the extrusion step is expected.

2.2.1.2 Mechanosensing effect of Shear Stress

Beside cell death, cellular response to surrounding shear stresses can cause the activation of pathways by way of mechanosensing and mechanotransduction. A downstream mechanoresponse can cause a cascade leading to conformational changes regulating cell growth, shape changes and differentiation. [76] Every cell type has a different shear stress magnitude and duration threshold above which this than act as a biophysical cue. [77] Studies which aim to quantify shear stress induced gene regulation analyse cellular phenotype, maturity, gene up- or downregulation after 12 to 48 hours of exposure and often these forces are maintained for multiple hours. [77], [82]–[86].

The effect of relatively short shear stress exposure (e.g. 3D printing) has been researched far less, with few studies examining gene expression in less after >2 h exposures.

Gomes *et al.* (2005) saw a significant increase of von Willebrand Factor (vWF) and thromobospondin-1 (TSP-1) in

HUVEC ECM after administering 130 mPa for 2 hours during culture. [87] The quick release of these glycoproteins change cell adhesion properties which, over the duration of culture, may induce alternate gene behaviour, protein release and differentiation. [87] On shorter timeframes a quick transient increase in Ca^{2+} by some bovine aortic endothelial cells (BAEC) has been observed after applying 2 mPa of shear stress, the magnitude of which increased, plateauing at 40 mPa and peaking after only 15-40 s. [88]
Because exocytosis of Ca^{2+} is known to induce vWF release, one needs to be mindful of induced shear stresses experienced by cell types which are mechanosensitive. [89]
Because during bioprinting cells only experience peak shear up to a couple of seconds while most downstream effect on prolonged cellular response is expected to be induced after minutes or hours, minimal to negligible effects on the cell species used are expected, and the examination of potential alterations in gene-expression, protein release or phenotype lay beyond the scope of this thesis.

2.3 Ink tracing properties

Embedding bath rheological properties greatly regulate ink deposition behaviour. When the needle dispensing is stationary in viscous a Newtonian embedding bath, higher viscosity allows ink retention while preventing mixing (**Fig. 3.A**). An example of a Newtonian hydrogel can be prepared by mixing XG and SA, which forms intramolecular hydrogen bonds, even at high XG concentrations. [90]
In non-Newtonian shear-thinning gel shear force imposed by a flowing ink can be sufficient to cause bath liquification. The fluid, always following the path of least resistance, moves along a thin liquefied boundary encompassing the needle, while the surrounding bath retains solid behaviour, as can be seen when printing in 1.5% (w/v) XG/Milli-Q water **Fig. 3.B**. This figure replicated from Trikalitis *et al*. (2023). [65]
Although in stationary deposition more localized ink retention is achieved in printing in Newtonian liquid, the control on location and extent to which bath liquification occurs in shear-thinning fluid, and thus where ink is mainly deposited, can be utilized. A bath through which a needle travels will locally liquefy along its path which, when extruding simultaneously, ink can push aside, resulting in a well-regulated deposition in the needle's wake.

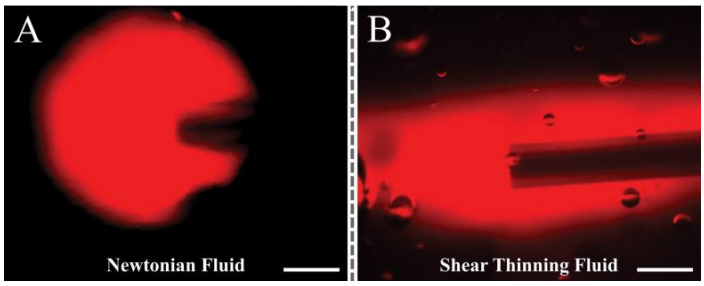

Figure 3. Stationary deposition location of water-based ink in Newtonian (1.5%/2.0% (w/v) XG/SA in Milli-Q-water) and non-Newtonian shear thinning (1.5% (w/v) XG in Milli-Q-water) hydrogel embedding baths, replicated from Trikalitis *et al*. (2023). Rhodamine B (1% w/v)-labelled water ink expands and mixes radially while expelled injected in Newtonian fluids while propagating along the nozzle direction in the non-Newtonian embedding bath. Scalebars white: 500 μm. [65]

Printing with a straight needle will create a cavity in its wake which will spontaneously collapse if hydrostatic stress at the bottom of the crevice exceeds the yield stress: [28]

$$\rho \times g \times h > \sigma_y \qquad \textbf{Eq. 12}$$

Or because $\sigma_y = \left(\frac{v}{d}\right) \times \eta$:
ρ = density, g = gravity, h = depth/height, σ_y = gel's yield stress, η = viscosity, v = tip speed and d = crevice diameter.

$$\left(\left({}^{v}/_{d}\right) \times \eta\right)/(\rho \times g \times h) < 1 \qquad \textbf{Eq. 11}$$

However, the current rheological properties of 1.5% (w/v) XG do not suffice in trapping ink in this manner, possibly due to slow bath recovery, which can take 10s of seconds until the hydrogel network has found a new steady configuration. [91] As can be seen in **Fig. 4.A**, this results in a vertical ink column (IC), or sheet, extending from the extrusion site, through the crevice, to the bath's surface.
Although vertical extrusion shows stable localized ink retentions (**Fig. 4.C**), this greatly restricts printing freedom. Similar problems have been solved by the addition of a third material, which fills the crevices to retain extruded bioink at the desired location. [46], [92] However, this introduces an additional setup component, the rheology, biochemical effects, and implementation of which has to be optimized. Instead, the choice was made to implement a 90° bend needle which essentially separates the extrusion site from the vertical crevice momentarily during movement, hindering the outflow of ink, allowing for the horizontal deposition of continuous lines **Fig. 4.B**.

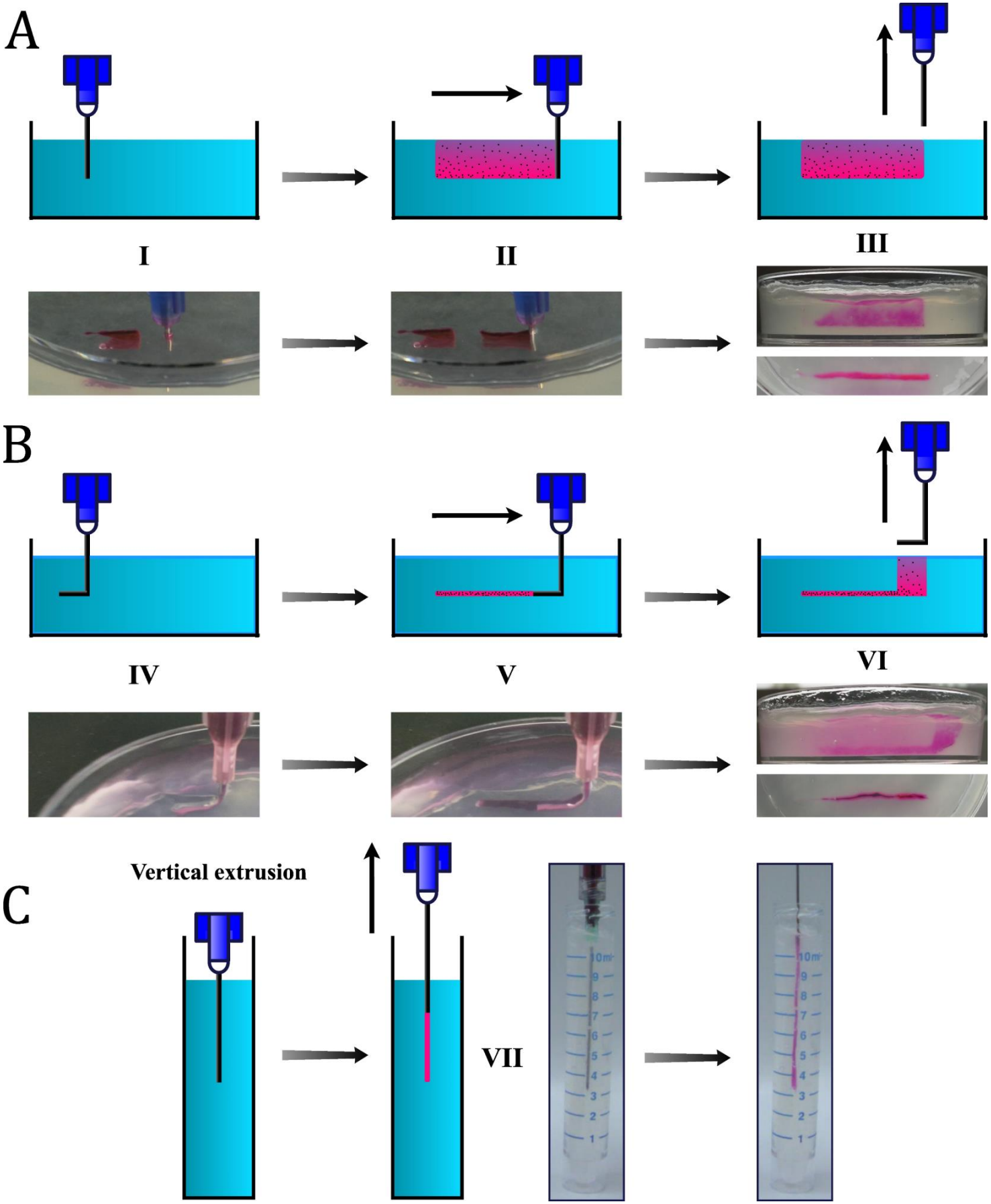

Figure 4. Ink retention inside cavity generated by moving extruding needle. The creation and subsequent filling of cavities by the movement of needles through a XG while extruding DPBS containing trace amounts of rhodamine, 20% OptiPrep, and additional pigment for better visualisation. **A)** A straight G23 stainless stain needle forms a thin sheet of ink. **B)** G18 90° bend stainless steel needle deposits a line while taking along a trace amount of ink during exit. **C)** Vertical extrusion with straight needle moving upwards, replicated from Trikalitis *et al*. (2023). [65] In all cases needle geometry governs deposition locations by creating liquefied sections or cavities of low resistance into which the ink easily flows and accumulates. Final deposition density is also dependent on particle density, ink density, ink extrusion volume and rate and time before particle movement is restricted by hydrogel repositioning.

Looking into the mechanics and results of extruding while stationary or in motion in more detail, different extrusion rates were tried by V. Trikalitis and M. Kaya which either form ICs larger (**Fig. 5-I** & **-IV**), matching (**II** & **V**) or are smaller (**III** & **IV**) than the needle's $Ø_{OD}$, which mainly governs the section of bath liquefied while in motion. [65] Both static and traveling extrusion resulted in severe bath shearing followed by radial expansion of the ink when the amount of ink when $Ø_{IC} > Ø_{OD}$.

A continuous and consistent cylindrical deposition can be seen while traveling if $Ø_{IC}$ matches $Ø_{OD}$, while an irregular and sometimes interrupted deposition was observed when $Ø_{IC} < Ø_{OD}$. These results show a theoretical window of extrusion rates, depended on gauge and movement speed, outside of which irregular deposition and poor shape fidelity is highly likely.

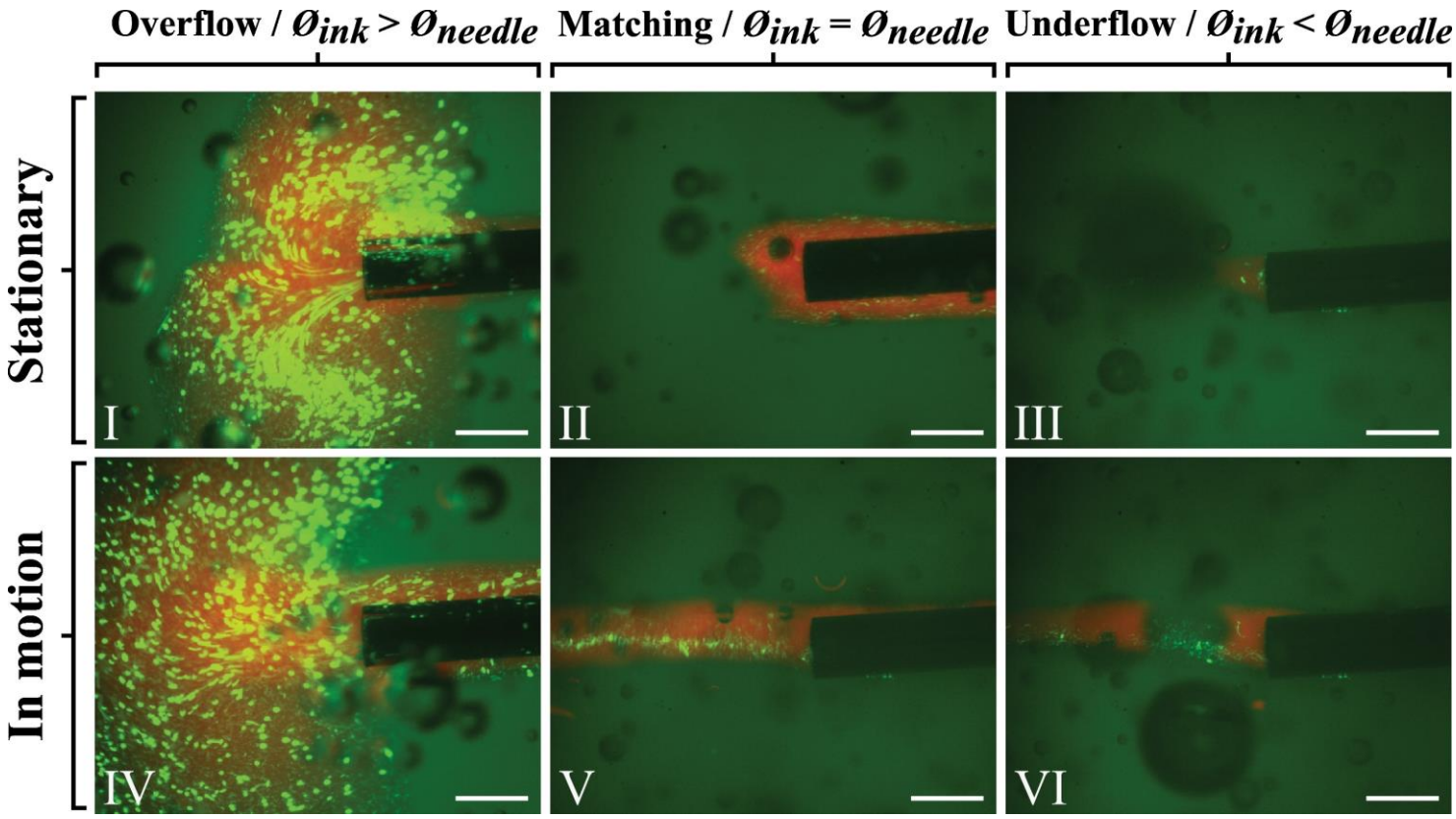

Figure 5. Ink deposition patterns at different extrusion rates by hand while stationary or in motion in 1.5% XG/Milli-Q water bath. (**I & IV**) Extrusion of an ink column significantly larger than the nozzle's OD at $\pm 1 \times 10^3$ µL min^{-1}. Causing radial overflow from the point of ejection and backflow over the needle surface, especially at when in motion. (**II & V**) Extrusion of ink column matching the nozzle's $Ø_{OD}$ at $\pm 1 \times 10^2$ µL min^{-1}. Causing backflow over the nozzle when stationary but constant deposition of ink with relatively stable diameter when in motion. (**III & VI**) Decrease in both the volume of backflow as well as ink column deposition diameter and consistency when extrusion rate is lowered to and underflow of $\pm 1 \times 10$ µL min^{-1}. This figure is based on data provided by V. Trikalitis and previously presented in Trikalitis *et al*. (2023). Scalebars white; 500 μm. [65]

2.4 Bioink diffusion packing mechanism

After depositing an aqueous and dilute particle suspension with water-based main carrier fluid (e.g. culture medium) in relatively high-concentration XG, a subsequent particle density increase is observed in the following minutes.
When printing of aqueous suspension inks into Newtonian (**Fig. 6.I-III**) and non-Newtonian (**Fig. 6.IV-VI**) hydrogel suspension baths are compared, a clear difference can be seen over time. In the Newtonian hydrogel the bioink readily mixes as can be seen by the wide area over which the suspended particles are located while the carrier fluid mixes and diffuses away. In the non-Newtonian XG bath however the movement characteristic of the ink's carrier fluid develops from being mainly governed by pressure driven flow towards concentration driven diffusion away from the deposition point, while the suspended particles radially accumulate.
It is theorised that this process, termed *diffusion packing*, comprises 2 simultaneously occurring stages. 1) The hydrogel matrix physical permeability allows the fast diffusion of carrier fluid into its surrounding, while the acting as a net for larger particles restricting their movement. 2) A slow expansion due to reorganisation of the hydrogel matrix pushes the particles closer together over a longer period of time. Although depended on the rheological properties of the embedding bath and the amount of ink deposited, the first stage has mostly concluded after 2 min, while the second stage can take several additional minutes to become unnoticeable.
This processes, which is to the best of our knowledge yet to be described and utilized in the field of 3D-bioprinting in detail, is a passive mechanism in which areas of very high particle/cell form, with little or no interstitial hydrogel.

A schematic drawing of this mechanism is depicted in **Fig. 7.A**. Printing vertical and horizontal sheets with straight and bend needles respectively (**Fig. 7.B-I - B-IV**) or the vertical extrusion of bioink show a good shape fidelity, retaining acrylic pigment particles in their respective positions while the carrier fluid (indicated by pinkish rhodamine B) diffuses (**Fig. 7.B-V** & **B-VI**). Using a custom setup, the exact position of each component involved in the mechanism; the XG embedding bath, the Newtonian bioink phase and suspended particles phase, can be followed in real time showing the process' progress (**Fig.7.C**). From this data, graphs can be produced which show the clear accumulation and dispersion of particles and carrier liquid respectively over time (**Fig. 7.D**).

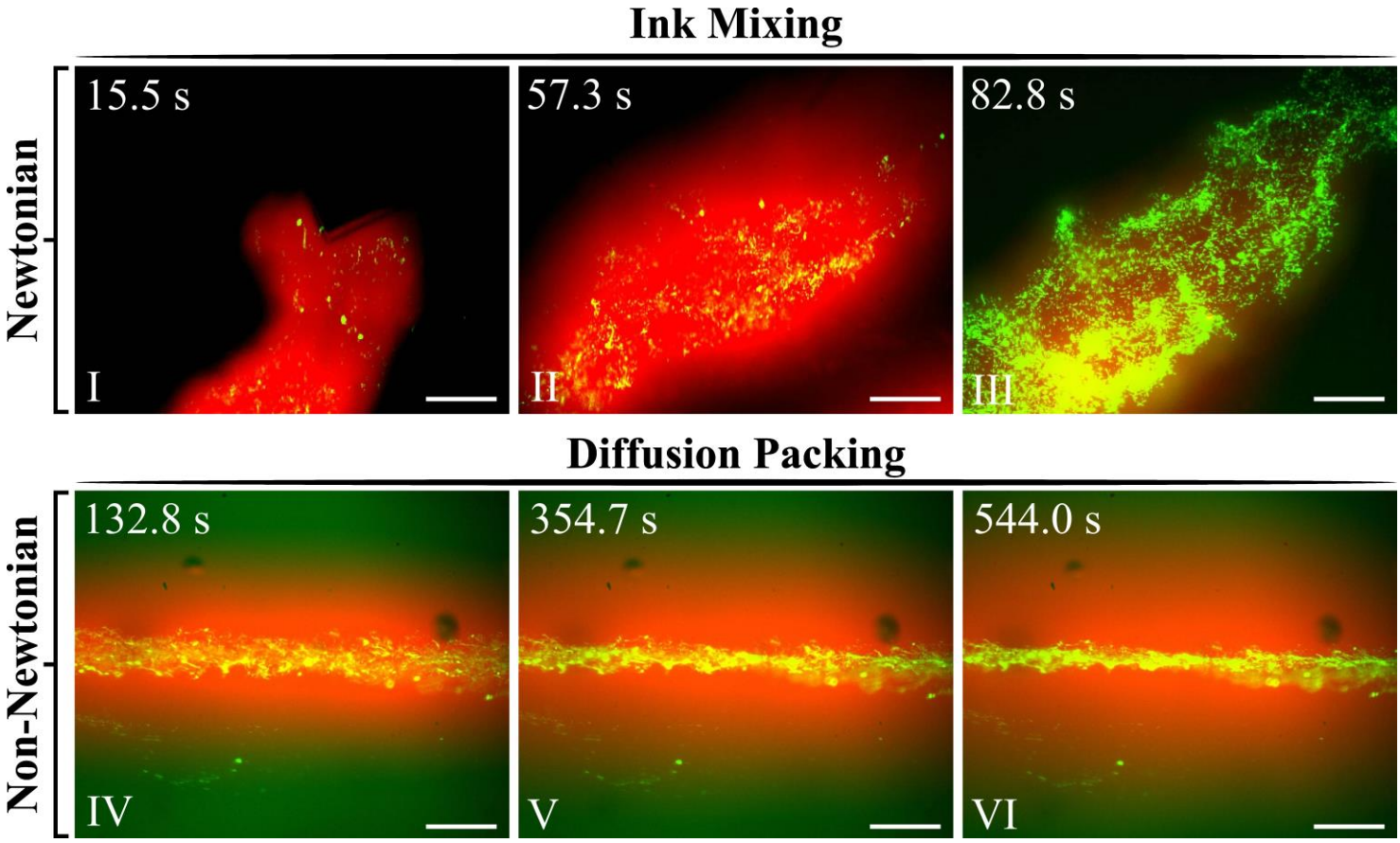

Figure 6. The progression of aqueous ink deposition patterns in non-Newtonian (1.5% (w/v) XG) and Newtonian (1.5%/2.0% (w/v) XG/SA) embedding baths. (**I-III**) PS-C6 particles (green) suspended at φ_p 0.1 in 0.1% (w/v) Rhodamine B-labelled Milli-Q water (red) was extruded from a needle, after which the ink mixes which the surrounding bath and the carrier fluid diffuses radially, making the particle-signal more prominent. (**IV-VI**) Deposition of the same ink in a XG embedding bath, also labelled green, resulted in the radial compaction of particles, greatly increasing their density locally, while the ink carrier fluid diffuses radially into the surrounding bath. Scalebars white; 500 μm. Based on data received from V. Trikalitis and part of which was published in Trikalitis *et al*. (2023). [65]

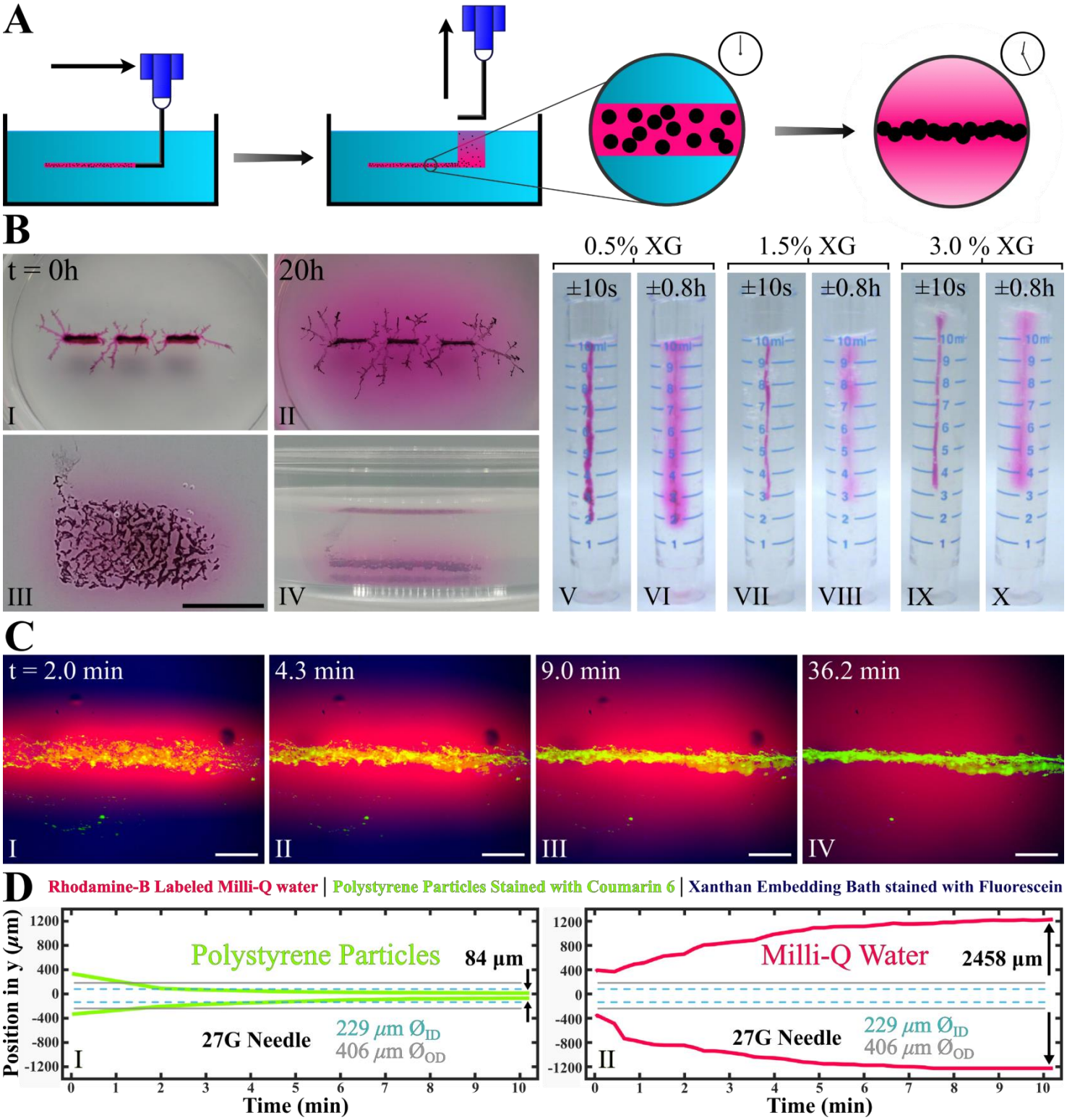

Figure 7. Diffusion packing. A) Schematic depiction of ink extrusion by a bend needle. Over time the ink's liquid phase will diffuse into the surrounding XG embedding bath, while particles larger than the hydrogel matrix pore size will be radially concentrated, pushed by the encloses hydrogel while the buffering liquid phase leaves. (**B.I**) Deposition of three 7mm lines of PBS based ink containing acrylic paint (1:10), Rhodamine B (1:10) and 11% OptiPrep in a 1.0% XG/water bath by a straight needle, forming sheets. Small irregularities on the bath's surface are filled with ink, forming shallow strands spread radially. (**B.II**) After 20 h the rhodamine B diffusion becomes clear, the flows through surface crevices extends, while the solid acrylic pigment particles are locally retained. (**B.III**) Horizontal movement of a bent needle while extruding an ink containing relatively dense dye pigment particles (1:10), and rhodamine (1:10) in PBS creating a heterogeneous sheet. (**B.IV**) Rhodamine diffusion into the 1.0% XG/PBS bath only a few minutes after printing, while the pigment is retained in a constant plain 1-2 mm above the dish's surface. (**B.V-X**) By-hand extrusion of ink containing rhodamine (1:100) while traveling vertically in (L→R) 0.5%, 1.5% and 3.0% (w/v) XG/Milli-Q water, followed by the condensation of suspended particles along its axis and radially rhodamine diffusion, replicated from Trikalitis *et al.* (2023). [65] Differences in visible inks can be ascribed to differences in extrusion quantities, not bath concentrations. **C.I-IV**) Close-up view of the diffusion of the Rhodamine-B labelled carrier fluid, the compaction of Coumarin 6 stained particles in a Fluorescein stained XG embedding bath over 4 times points. (**D.I**) Graph denoting the position of outermost particles at a single slice of line deposited with a G27 needle, with $Ø_{OD}^{G27}$ and $Ø_{ID}^{G27}$ are given as reference, showing a compaction from a diameter slightly exceeding $Ø_{OD}^{G27}$ to a final width sub-$Ø_{ID}^{G27}$. (**D.II)** Graph of outermost fluorescent Rhodamine B signal along the same slice and timeframe, showing radial diffusion. The data and analysis in **C** and **D** are provided by V. Trikalitis and replicated from Trikalitis et al. (2023). [65] Scalebars black; 10 mm, white 500 μm.

2.1 Density modifier

Depending on the length of the printing session, the ink is kept stationary in the syringe for ≥5 minutes, during which significant densities differences between particles, insoluble liquids, and the ink's primary liquid phase can cause these components to settle somewhere in te ink container. The resulting heterogeneous suspension or emulsion may create clogs and an ink composition which is not consistent over time during the session, which degrades print fidelity and reproducibility. [93]–[97]

To mitigate particle settling, while also providing significant mechanical protection to shear induced damage, the use of dilute shear thinning hydrogels have been successfully demonstrated. [98] However, the issue of non-traversable interstitial hydrogel remains.

A soluble 60% (w/v) iodixanol-based density (ρ) modifier (brand-name; OptiPrep™) with a density of 1.320 ±0.001 g/mL, slightly above that of water/medium, is employed to raise the carrier fluid's density, approximately matching that of the particles and liquids to be suspended with minimal impact rheologically and biologically. Altering the fraction of OptiPrep, a liquid's density can be tuned causing particles to either sink, suspend or float, **Fig. 8.A-C** respectively, keeping the bioink suspension homogeneous and allowing for the extrusion of a stable concentration of particles over longer time periods.

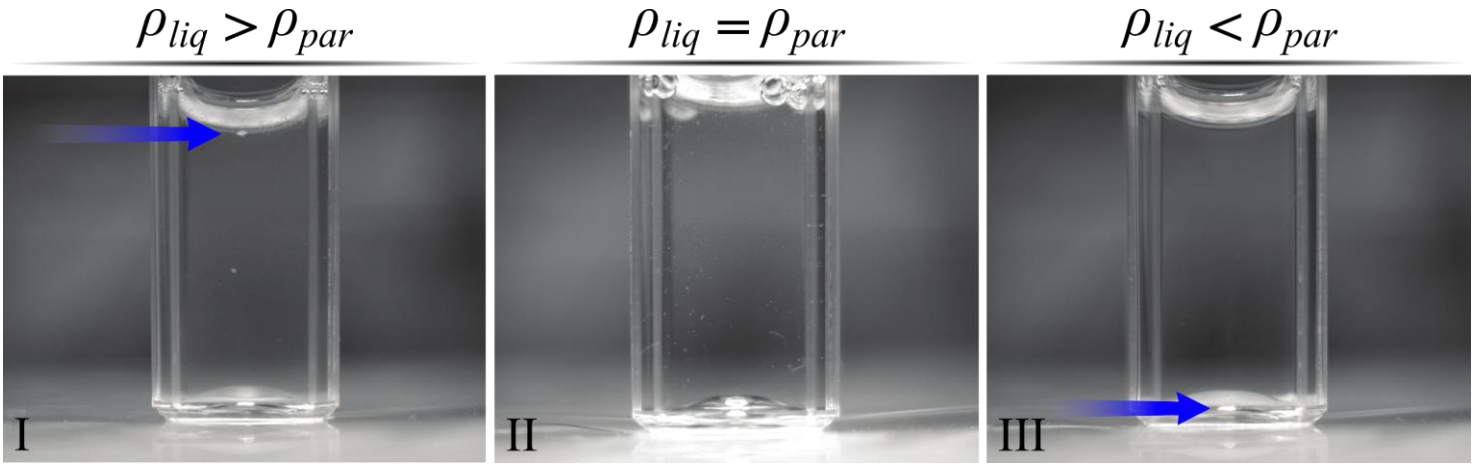

Figure 8. Density modification. Particles suspended in liquid where the densities are changed using the addition of OptiPrep such that **(I)** $\rho_{liq} > \rho_{par}$, **(II)** $\rho_{liq} = \rho_{par}$ and **(III)** $\rho_{liq} < \rho_{par}$. Images previously published in Trikalitis *at al*. (2023) and were kindly provided for replicating here. [65]

Chapter 3. Materials and Method

3.1 Cell Culture

3.1.1 Culture of hPSCs

Feeder-free human pluripotent stem cells (hPSCs; Coriell, GM25256), a human embryonic stem cell (hESC) line (HES3) expressing both green fluorescent protein (eGFP) at the NKX2.5 locus and mRubyII as a fusion protein with α-actinin, were used for differentiation into cardiomyocytes (CMs). NKX2.5 is a well-established as a human cardiac reporter present in both progenitor and contracting CMs and α-actinin, a sarcomeric protein, is especially prevalent in the contracting CMs. Forming the double reporter *mRubyII-ACTN2* and *GFP-NKX2.5* (DRRAGN) line when differentiated to CMs, as previously described in Ribeiro *et al*. (2020). [99]

hPSCs, also from the HES3-line, expressing double reporters for both *NKX2.5*$^{GFP/+}$ as well as chick ovalbumin upstream promotor transcription factor (COUP-TFII) expressing mChrerry (*COUP-TFII*$^{mCherry/+}$), which is expressed in mesodermal cell types including some endothelial cells, were differentiated into epicardial-like cells (ECCs) as reported in Schwach *et al*. (2017). [100]

Both the hPSCs, together with WTC iPSCs (Coriell, GM25256) used for printing only stem cells (SCs), were seeded in stem cell growth medium (SC-GM); Essential 8-medium (E8; ThermoFisher, 1517001) + 0.5% RevitaCell (ThermoFisher, A2644501) on tissue culture-treated (TCT)-plates (Greiner, 354230) coated with vitronectin (ThermoFisher, A14700), and cultured by refreshing daily with E8 without RevitaCell during which they were passaged twice a week, using EDTA (ThermoFisher, 15575020) for dissociation. After sufficient cell numbers were reached, differentiation was started or, in for WTC iPSCs, directly used in the bioink.

3.1.2 Differentiation & culture hPSC-derived CMs

Differentiation of hPSCs$^{eGFP\text{-}NKX2.5/+\text{-}mRubyII\text{-}ACTN2/+}$ into CMs was performed as described previously by Birket *et al*. (2015). [101] As schematically depicted in **Fig. 9**; one day before the start of differentiating hPSCs into CMs they were seeded on growth factor reduced Matrigel-coated plates (Corning, 354230) at $10\times10^3/cm^2$ with E8 + 0.5% RevitaCell medium. At day 0 the cells are washed with Bovine Serum Albumin (BSA; Sigma-Aldrich, A3311), polyvinyl alcohol, essential lipids (BPEL)-medium after which BPEL supplemented with 1.5 µM glycogen synthase kinase 3 (GSK3) inhibitor and Wingless-related integrin-site 1 (WNT) pathway activator CHIR99021 (Axon Medchem, CT 90021), 20 ng/mL human activin A (ACT-A; Miltenyi Biotec, 130-115-010) and 30 ng/mL bone morphogenetic protein 4 (BMP4; R&D Systems, 314-BP/CF) was added. [102] On day 3 BPEL supplemented with 5 μM XAV939 (R&D Systems, 3748) was added followed by a medium refreshment with only BPEL on days 6 and 10. Following differentiation if spontaneous regular cell contraction could be seen by >70% of the cell population, it was purified to only CMs by making use of their ability to metabolise lactate, unique compared to the other cell-types present. To achieve this; on days 13 and 15 they were cultured in CM maturation medium (CM-MM) supplemented with 7.18 μL/mL Na-DL-lactate (L; Sigma-Aldrich, L1375). The composition of CM-MM has been shown to optimize for CMs maturation and function and can be found in **Apx II**. [101] At day 17 CM-MM + lactate was supplemented with 1% glucose (G; Sigma-Aldrich, 346351). Starting between days 20 and 22 the cells were harvested, for freezing or direct use in the bioink, by a 3 min incubation with TrypLE (10X) (Thermo-Fisher, A12177) at 37°C for dissociation.

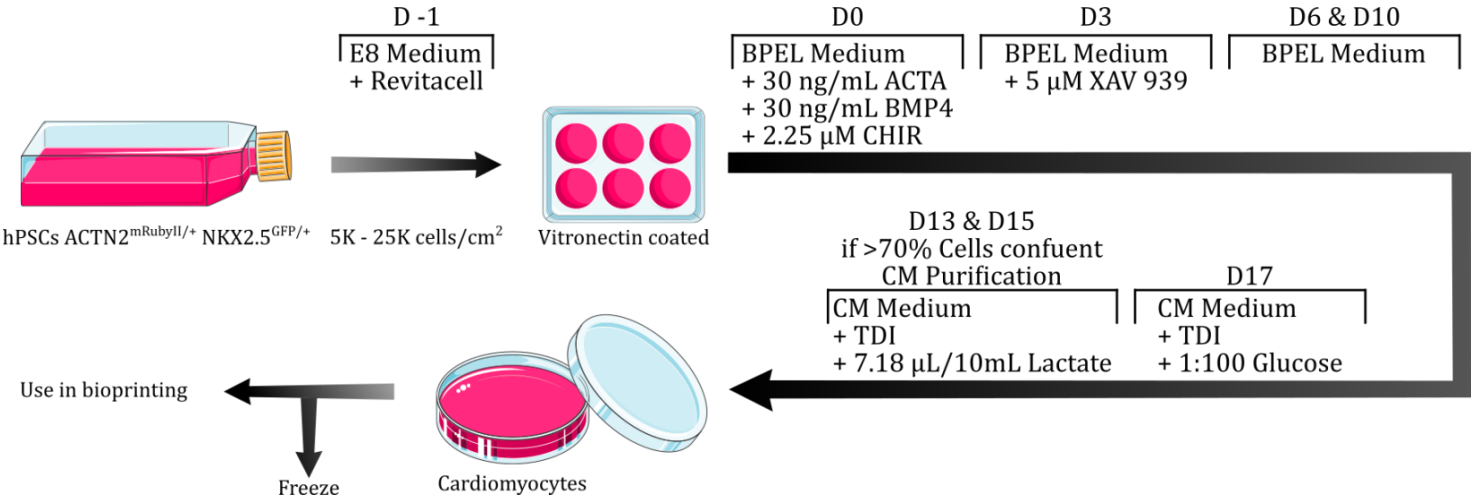

Figure 9: Schematic of the protocol used for differentiating hPSCs into CMs. [101]

3.1.3 Differentiation & culture from hPCS-derived ECCs

hPSCs$^{eGFP\text{-}NKX2.5/+\text{-}mCherry\text{-}COUP\text{-}TFII/+}$ differentiation into functional epicardial-like cells (ECCs) was performed based on the method described by Guadix *et al*. (2017). [100], [103] As schematically shown in **Fig. 10**; at day -1 hPSCs were seeded at $10\times10^3/cm^2$ in vitronectin coated plates. At day 0 they were washed with BPEL-medium and BPEL + 1.5 μM CHIR99021, 20 ng/mL Activin-A and 20 ng/mL BMP-4 was added. This was replaced by BPEL + 5 μM XAV939, 1 μM retinoic acid (RA; Sigma-Aldrich, R2635) and 30 ng/mL BMP-4 on day 3. On day 6, PBEL with 1 μM RA and 30 ng/mL BMP-4 was added. Using TrypLE (1X), for which TypLE (10X) was diluted 1:10 with Dulbecco's phosphate-buffered saline (DPBS; ThermoFisher, 14190), the cells were dissociated on day 9 and reseeded on 5 μg/mL fibronectin-coated (Sigma-Aldrich, F1141) plates at $25\times10^3/cm^2$, after which they were cultured with ECC-growth medium (ECC-GM): BPEL containing 10 μM transforming growth factor (TGF)-βRI-inhibitor SB431542 (SB43; R&D Systems, 1614). Between days 13 and 14 the ECCs were confluent and ready to be harvested for freezing or to be used in the bioink directly.

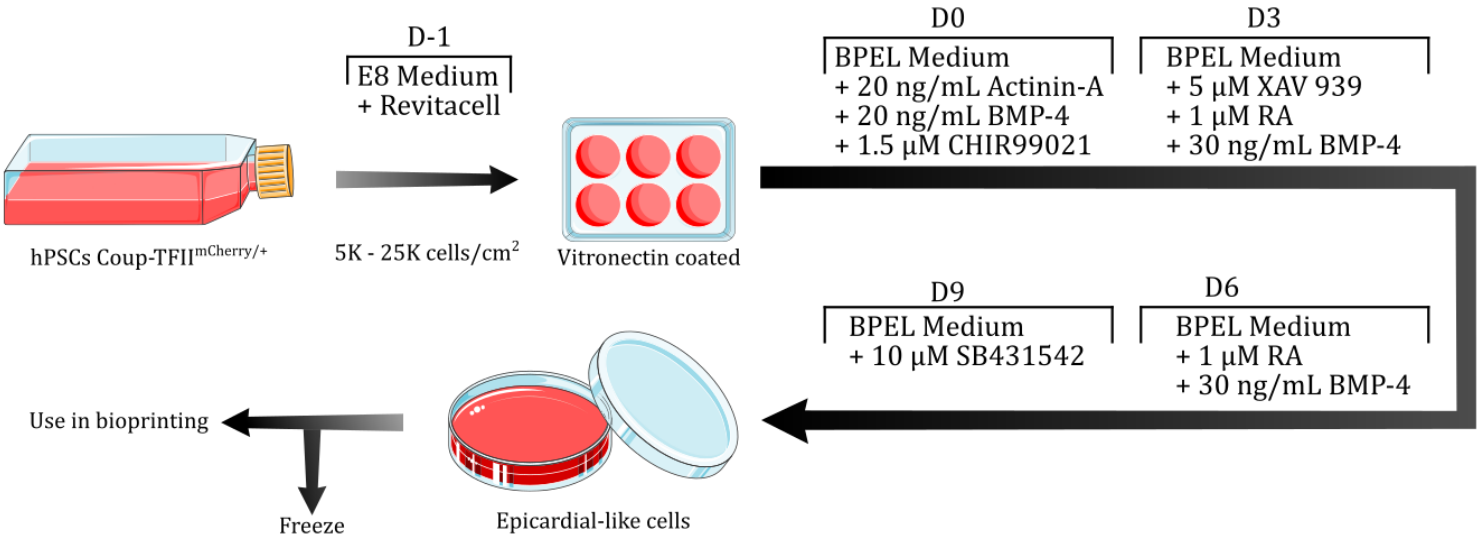

Figure 10: Schematic of the protocol used for differentiating human pluripotent stem cells (hPSCs) into epicardial-like endothelial cells (ECCs). [100]

3.1.4 Culture of RFP-SMCs

For the printing inks containing cell spheroids, a combination of cell spheroids with particles or sperate cells combined with human aortic smooth muscle cells (SMCs, P4+2) expressing red fluorescent protein (RFP-SMC; Angio-Proteomie, cAP-0026RFP) were thawed (**§3.1.6**) and seeded at $2.7\times10^3/cm^2$ on TCT-plates in SMC growth medium-2 with supplements (Lonza, CC-3182 + CC-4149) + 1% (v/v) penicillin/streptomycin (P/S; Thermo Fisher, 15070063) (SMC-GM2). The medium was replaced every 2 days up to day 7. They were then dissociated with TrypLE (1X), reseeded at $9.5\times10^3/m^2$ and cultured in SMC-GM3: 76.5% Dulbecco's Modified Eagle's Medium (DMEM; Thermo Fisher, 41965-039) with 20% fetal bovine serum (FBS; Sigma-Aldrich, F7524), 2.5% (v/v) 1M 4-(2-hydroxyethyl)-1-piparazineethanesufonic acid (HEPES; Thermo Fisher, BP310) in phosphate buffered saline (PBS; Thermo Fisher, 18912-014) and 1% P/S. At day 15 they were dissociated and used to form SMC-spheroids (**§3.2.7**) or used in the bioink directly.

3.1.5 Culture of C2C12 cells

Quickly proliferating C2C12 cells were thawed and seeded at $2\times10^3/cm^2$. Cultured in C2C12-medium consisting of DMEM + 10% FBS and 1% P/S until 60% confluent, they were dissociated using a 3 min incubation with 0.25% trypsin-EDTA (Thermo Fisher, 15400054) after which they were directly used in the bioinks.

3.1.6 Freezing & thawing of CMs, ECCs & SMCs

The cells that were thawed for these experiments were frozen in liquid nitrogen (LN). This was performed by first washing the culture 3× with DPBS and then adding Trypsin-EDTA for dissociation. After incubating for 5 min at 37 °C the cells are detached and the Trypsin-EDTA is inactivated by adding 1:4 DMEM. The cells were then pelleted centrifugally for 5 min at 300 $*g$ (Eppendorf, 5810R) and the supernatant is removed. They were then resuspended in their specific cell culture medium, counted and pelleted again. After removing the supernatant ice-cold freezing media was added after which the suspension was kept on ice. Separated in files and after being cooled at ±1 °C/min overnight to -80 °C, they were transferred to the LN-vessel for long-term storage. For freezing CMs the freezing medium consisting of; 50% KnockOut™ Serum Replacement (Thermo Fisher, 10828), 40% CM-MM + lactate + glucose and 10% Dimethyl sulfoxide (DMSO)-Hybrimax (Sigma-Aldrich, D2650). For ECCs; 80% ECC-GM + 20% DMSO and for SMC; 90% FBS and 10% DMSO.

Thawing of cells from LN-storage was done by warming the tubes in a 37 °C water bath until only a small amount of ice remained. Cold cell-specific medium was then slowly added to dilute the freezing medium to at least 1:6. After which they were pellated by centrifuging at 240 $* g$ for 3 minutes, after which the supernatant is removed, cell-specific culture medium is added, and they are either used in monolayer culture or used in the bioink immediately.

3.1.7 Culture of RFP-SMC-spheroids

After culturing a sufficient number of SMCs, they were harvested by using Trypsin-EDTA 0.25% and reseed into an 4% agarose (Invitrogen, 16500) mould consisting of cylindrical microwells of ±200 μm diameter (Ø) and ±200 μm deep at ±267 cells/μwell in SMC-GM2. Half the medium was replaced daily, resulting in an average spheroid diameter ($Ø_{avr}$) of ±67 μm after 7 days. Retrieved by flushing out and pelleted by centrifuging at 960 $* g$ for 1 min. **Fig. 11.B-I** & **-II** shows the compaction from sperate cells at day 0 to a compact spheroid of roughly 70 μm $Ø_{avr}$.

For bioink containing only SMC-spheroids, the SMC-culture, subsequent spheroid formation and collection was performed as mentioned prior, except instead of SMC-GM2, Human Smooth Muscle Cell Growth Medium (Cell Applications, 311) + 1% P/S (SMC-GM1) was used. Resulting in spheroids with $Ø_{avr}$ 112 μm.

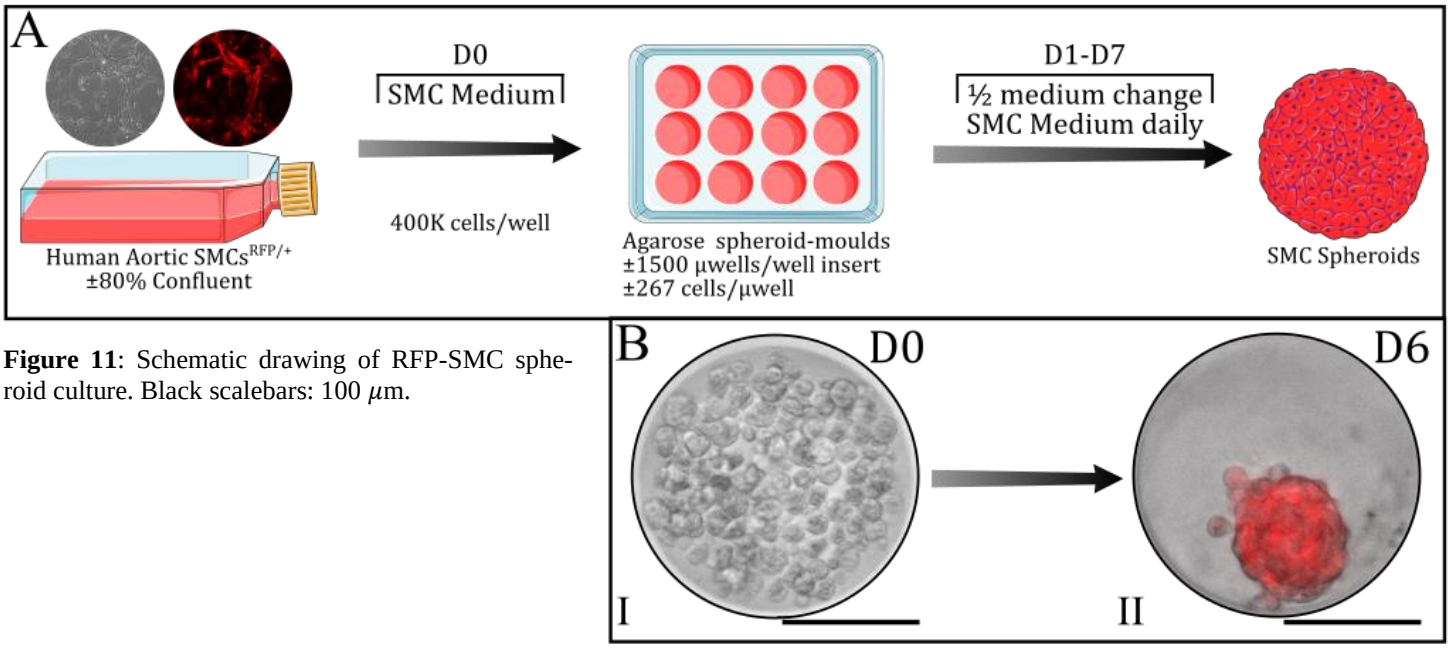

Figure 11: Schematic drawing of RFP-SMC spheroid culture. Black scalebars: 100 μm.

3.2 Bioink preparation & syringe loading

All inks were prepared by a similar manner. First the cells, spheroids or particles are harvested, thawed or filtered. Then centrifugally pelleted and subsequently resuspended in their respected carrier fluid. The density was modified by the addition of 60% (w/v) iodixanol-based OptiPrep (STEMCELL Technologies, 07820). The components, which were at room temperature (RT), were carefully mixed to avoid foam formation.

Creating a bioink where the liquid component was mainly composed of a xanthan gum (XG; Sigma-Aldrich, G1253) hydrogel based on cell culture medium, the XG powder was added to the cell medium and OptiPrep after which it was mixed on a tilt-and-toll mixer (LLG-uniRoller 6, LLG-Labware, Germany) for ±24 hours at RT. Before use the air bubbles were removed by centrifuging for 1 min at 300 $* g$ before being added to the cells which were carefully resuspended to avoid the formation of bubbles. If bubbles were introduced, they were removed as much as possible by a short 1 min centrifugation at 200 $* g$.

A 1000 μL pipette tip was used to transfer bioink into the tip of a 1 mL syringe (BD & Co., 309628). A blunt 90° bend stainless steel G18 (965 μm $Ø_{ID}$, 1092 μm $Ø_{OD}$), G23 (406 $Ø_{ID}$, 635 $Ø_{OD}$), G26 (279 $Ø_{ID}$, 483 $Ø_{OD}$) or G27 (229 $Ø_{ID}$, 406 $Ø_{OD}$) (NeedlEZ) was fitted for printing using bend needles. [81] When printed with a straight needle, a stainless steel G22 blunt tip needle (410 μm $Ø_{ID}$, 720 μm $Ø_{OD}$, CELLINK) was used. [104] Before and after each printing session the needles were cleaned by flushing with 70% ethanol after submersion at least 30 minutes and subsequently air-dried.

3.2.1 CMs laden Newtonian bioink

DRRAGN line derived CMs (P10+21) were thawed and resuspended in DMEM and centrifugally pelleted at 240∗g for 3 min. They were resuspended in CM-MM1 and 20% (v/v) OptiPrep, 4 μg/mL human collagen type I (hCol-I; 1 mg/mL, Merck, CC050) and 6 μg/mL human collagen type III (hCol-III; 1 mg/mL, Merck, CC054). The final concentration was 15.5×10^6 cells/mL and the $\emptyset_{avr}$ was ±19.9 μm resulting in an ink of φ_p 0.063.

3.2.2 CMs laden non-Newtonian hydrogel bioink

Thawed lactate purified FLB CMs (P27+44) of $\emptyset_{avr}$ 25 μm were resuspended in 0.75% w/v XG made from CM-MM supplemented with 2.1 μg/mL hCol-I and 3.0 μg/mL hCol-III at 12.2×10^6/mL to create non-Newtonian bioink of φ_p 0.10, laden with a non-proliferating cell species.

3.2.3 Proliferating iPSCs laden Newtonian bioink

WTC-hiPSCs (P20+12) were cultured in E8, dissociated, pelleted at 230∗g for 3 min and resuspended in 67% E8 and 20% (v/v) OptiPrep at 37.3×10^6 cells/mL, which with $\emptyset_{avr}$ ±19µm formed a bioink with φ_p 0.134.

3.2.4 C2C12-laden Newtonian bioink for XG/SA-bath

C2C12 cells (P16) that were printed in a bath composed of both XG and sodium alginate (SA; Wako, 196-13325) were suspended in C2C12-med and 20% (v/v) OptiPrep at 8.3×10^6 mL^{-1} to a relatively low φ_p 0.01. This was to aid the aim of exploring the printing of larger, more spread-out structures without local overpopulation of the fast-proliferating C2C12 cells, depleting available nutrients before an interconnected and stable structure form.

3.2.5 C2C12-laden non-Newtonian bioink for XG-bath

C2C12 were dissociated with Trypsin-EDTA 0.25% centrifuged at 300 $* g$ for 3 min and resuspended in 1.0% (w/v) XG/C2C12-Med hydrogel, 20% (v/v) OptiPrep at 87×10^6 mL^{-1}. With 13 μm $\emptyset_{avr}$ the bioink had a φ_p 0.10.

3.2.6 Bioinks containing both CMs & ECCs

The cells used bioinks containing a mixture of CMs (P10+21) of $\emptyset_{avr}$ 19.9 μm and ECCs (P4+27) with $\emptyset_{avr}$ 15.2 μm were thawed, pelleted at 240 $* g$ for 5 min and resuspended in 70% CM-growth medium (CM-GM; DMEM + 10% horse serum (HS; ThermoFisher, 26050088) + 1% P/S + 10 μg/mL insulin (Sigma-Aldrich, I9278)) and 20% (v/v) OptiPrep with both φ_p^{CM} and the φ_p^{ECC} at 0.05 for a φ_p^{tot} of 0.10. [105]

3.2.7 SMC-spheroids bioinks

Bioink composed of only RFP-SMC (P4+4) spheroids were created by mixing spheroids, cultured for 7 days to an $\emptyset_{avr}$ of ±109 μm, with 70% SMC-GM2 and 20% (v/v) OptiPrep at 14×10^3 mL^{-1}, resulting in a φ_p 0.10 bioink.

3.2.8 SMC-spheroid & Col-PLA-μparticles bioink

SMC-spheroids from RFP-SMCs (P4+4) with an $\emptyset_{avr}$ of 67.3 μm were resuspended with a final concentration of 1.04×10^5 mL^{-1}, resulted in a partial φ_p^{sph} of 0.017.

Collagen coated poly(lactic acid) (PLA) microparticles (Col-PLA-μparticles; MicroMod, 11-25-304) with $\emptyset_{avr}$ of 30.25 μm, were centrifuged at 200 $* g$ for 1 min. After aspirating the supernatant, they were resuspended and incubated at 37 °C for 4 hours in 1:10 P/S in PBS for sterilisation. They were the again pelleted at 200 $* g$ for 1 min, resuspended in SMC-GM2 and added to the SMC-spheroid suspension at 9.2 ×10^5 mL^{-1} forming a $\varphi_p^{\mu p}$ of 0.017 for a 0.034 φ_p^{tot}. Compensating for the both the μparticles' and spheroids' relatively high density 46% (v/v) OptiPrep was used in 51% SMC-GM2 as the carrier fluid.

3.2.9 SMCs & Col-PLA-μparticles mixed bioinks

SMCs (P4+2) were thawed, and their population was expanded by culture in SMC-GM2 and passage once. Pelleted at 230 $* g$ for 3 min and with $\emptyset_{avr}$ 26.5 μm resuspended at 7.7×10^6 mL^{-1} in SMC-GM2 forming a φ_p^{SMC} of 0.075. After the addition of 24% (v/v) OptiPrep and Col-PLA μparticles 30.25 μm $\emptyset_{avr}$ were added in the at 8.9×10^5 mL^{-1} for a 0.013 $\varphi_p^{\mu p}$ and a 0.088 φ_p^{tot}.

3.2.10 Alginate hydrogel spheroid suspension inks

Large green-fluorescent alginate hydrogel microbeads, made in-house using in-air microfluidics as described in Kamperman *et al.* (2018), were labelled with fluorescein isothiocyanate (FITC). [106] With a $\emptyset_{avr}$ of 160 μm, they were gathered from suspension using a 70 μm cell strainer. Resuspended at ±47×10^3 mL^{-1} in DPBS resulted in a 0.10 φ_p ink.

3.2.11 PLA-μparticle suspension inks

PLA microparticles (PLA-μp; Micromod, 11-00-203) were disinfected in the same manner as the Col-PLA-μparticles. They were then suspended at 6.9×10^6 mL^{-1} in 80% (v/v) OptiPrep + 10% P/S creating a 0.10 φ_p ink.

3.2.12 acrylic paint particles suspension inks

Acrylic paint was diluted with water after which the pigment particles suspension was centrifuged at 300 $* g$ for 5 min. The pellet was resuspended in 45% DPBS with 40% (v/v) OptiPrep and 10% rhodamine B (Labshop, K94900-25) forming a suspension of 0.05 φ_p. Their size range was very polydisperse, however generally $\emptyset$ <10 μm.

3.2.13 Relatively high-& low-density particles inks

For showing the effect of including particles with densities significantly higher and lower than the carrier fluid in the same ink, dye containing mostly iron oxide particles diluted with PBS and centrifuged at 300 $*$ g for 5 min. This created a sunken and floating pellet comprising high- and low-density particles respectively. Low-density particles consisted of air bubbles surrounded by pigments, decreasing their overall densities. The intermediate supernatant was aspirated, the particles were resuspended in DPBS and a drop of soap, which increased suspension stability, was added forming a particle suspension of φ_p ±0.05 which was homogenous for up to 4 minutes.

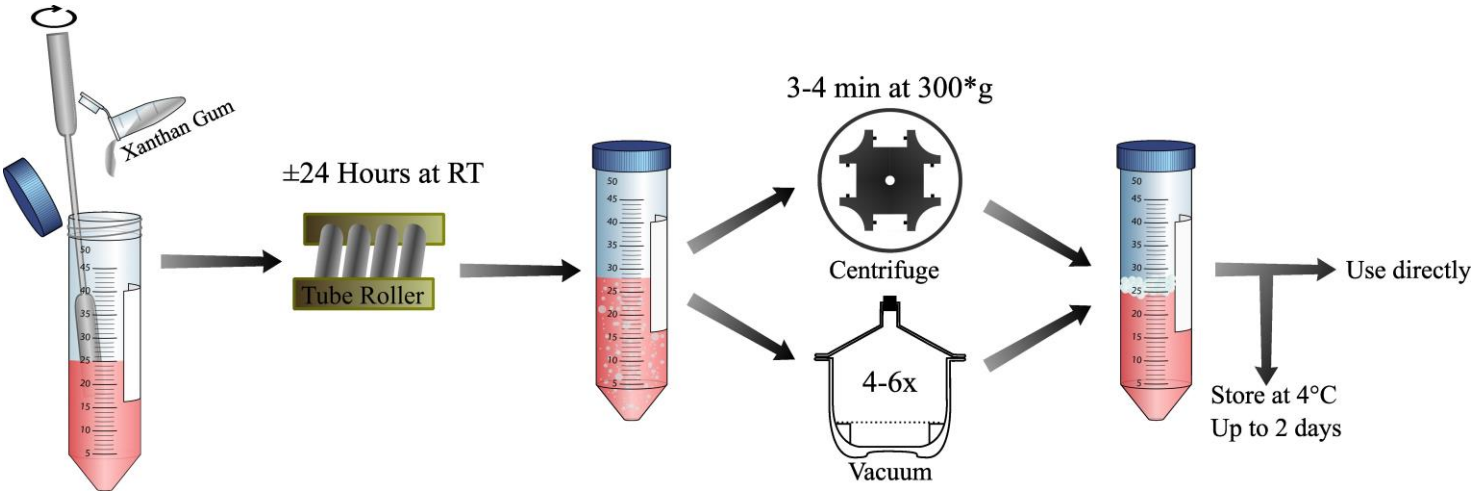

Figure 12. Schematic drawing of standard Xanthan Gum hydrogel embedding bath preparation.

3.3 Preparation of XG-hydrogel embedding baths

Creating a XG hydrogel embedding bath required relatively few and simple steps, as depicted in **Fig. 12**. All baths were created in a similar manner by first mixing Xanthan Gum powder, from *Xanthomonas Campestris,* or a mixture of XG and SA powders with the liquid component, which could be cell-specific culture medium, DPBS or Milli-Q water, in a 50 mL centrifuge tube while stirring. After shaking vigorously, the mixture was put on tube roller mixer for 24-30 hours at RT, during which a homogeneous hydrogel formed, which however still contained air bubbles. When not used immediately, the gel was stored after this step up to 2 days at 4 °C. The air bubbles were removed utilizing 2 different methods, depending on the bath's properties. First the mixture was shortly centrifuged for 1 min at 200 $*$ g to remove the largest air pockets. The container was then placed into a desiccator and a partial vacuum was established and quickly released, popping bubbles. However, gel made from some culture media possessed properties such as high surface tension, making bubbles very stable, and thus this vacuum method impractical or impossible. For these gels the first centrifuging step was intensified by a prolonged and more intense spin of 3-4 min at 300 $*$ g, removing most (large) bubbles. 35 mm non-TCT petri dishes (Greiner bio-one, 627161) or 60 mm non-TCT petri dishes (StemCell Technologies, 38069) were filled with ±7 mL or ±18 mL of gel respectively, creating an embedding bath ±7 mm in height. Which were then sealed and stored for up to 2 days at 4°C or used directly for printing after being stored in an incubator at 37 °C for at least 2 hours.

3.3.1 XG baths for CM-laden Newtonian bioinks

Newtonian CM-laden bioinks were printed in an embedding bath composed of 1.5% (w/v) XG in CM-MM supplemented with 5 mM lactate and 1% glucose.

3.3.2 XG baths CM-laden non-Newtonian bioinks

XG hydrogel bioinks laden with CMs were printed in an embedding bath consisting of either 1.5% (w/v) XG in DMEM or 1.5%/1.5% (w/v) XG/Alg in DMEM. DMEM was used instead of CM-MM or CM-GM because this hydrogel formulation exhibits less viscosity, aiding in less destructive bath removal. In addition to this it was hypothesized this could mean a faster bath recovery and thus special bioink retention when printed with a straight vertical needle.

3.3.3 XG Baths for WTC iPSC-laden Newtonian bioinks

Embedding baths into which WTC-iPSCs-laden bioinks were printed comprised 1.5% (w/v) XG in E8 medium.

3.3.4 XG/SA baths for C2C12-laden Newtonian bioinks

For printing a fast-proliferating C2C12 cell suspended in a Newtonian bioink into a viscous Newtonian hydrogel support 1.5 (w/v) XG and 2.0% (w/v) SA powders were first mixed and then added to C2C12-medium in to 1.5% (w/v) and 2.0% (w/v) respectively.

3.3.5 XG & XG/SA baths for C2C12-laden non-Newtonian bioinks

Embedding baths for printing XG hydrogel bioinks, laden with fast-proliferating C2C12 cells, with a straight needle were made from C2C12-medium mixed with either 1.5% (w/v) and 1.5%/1.5% (w/v) XG/SA.

3.3.6 XG baths for CM- & ECC-laden bioinks

The embedding bath used for printing a mixture of CM and ECCs were made from 1.5% (w/v) XG in CM-GM.

3.3.7 XG baths for SMC-spheroid-laden bioinks

Due to the rheological properties of a XG/SMC-GM1 hydrogel exhibiting relatively high viscosity, air bubbles are near impossible to remove compared to other culture media-based gels. The final XG concentration was halved to 0.75% (w/v) in SMC-GM1 to partially reduce viscosity.

3.3.8 XG baths for SMC-spheroid & col-PLA-μparticle mixed bioinks

Bioinks containing the combination of SMCs, either sperate or in spheroids, and col-PLA-μparticles were printed in a bath comprising 1.5% (v/v) XG in SMC-GM3.

3.3.9 XG baths for suspended hydrogel spheroid, PLA-μparticle, or paint pigment particle-laden inks

Ink containing only particles (alginate, PLA-μparticles, or paint pigment particles) were printed in a hydrogel made by mixing 1.5% (w/v) XG in DPBS.

3.4 G-Code design

The g-codes, describing the operations to be performed by the printer, were designed based on initial settings provided by the printer manufacturer's software NewCreatorK (ROKIT Healthcare, v1.57.70).

The most important commands consist of a series of *X*-, *Y*- and *Z*-values [mm], describing a series of points, or nodes, in 3D space which in sequence describe a path. Utilizing the *G1*-command for *coordinated movement* the build platform moves in the XY plane while the syringe holder moves up and down along the Z-axis. Overall desired movement speeds along a path between 2 points can be set between 1 to 20 mm/s at increments of 1 mm/s using the feedrate (*F*)-command. A maximum movement speed along each separate axis can also be set using the *M203*-command. At each note the extrusion value (E)-command [mm] sets the plunger height. If there is a difference in *E*-value between 2 nodes, the printer will continuously move the plunger in a linear manner when traveling between them, causing extrusion (or suction). The extrusion rate [μL/s] is therefore dependent on 1) the movement speed between two points and 2) the speed at which the printer can initiate a command and ramp-up.

The code was changed often between printing experiments based on new observations, the use of new tools and materials, or change bioink compositions (φ_p's). Due to the current limitations of the platform, all paths used for the results discussed in **Chapter 5**, describe a straight- and horizontal-line during extrusion. For calculating the dimensions of the line to be printed it was assumed that 1) the extruded ink column formed a uniform cylinder with its central axis identical to the needle's central axis and 2) liquid diffusion occurred uniformly and radially, thus causing particle compaction about this axis.

3.5 3D-Bioprinting

3.5.1 The 3D-printing process

Printing was performed with a ROKIT INVIVO hybrid 3D printer (ROKIT Healthcare) composed of a syringe holder with plunger press, which can only move up and down in the Z-axis in its entirety, and a movable platform which can move in the X/Y-axes. After printer calibrations, the build in HEPA air filter system was engaged, its interior was cleaned with 70% (EtOH) and the build in UV lights were activated for sterilisation at least 30 min prior to printing. The syringe was mounted, its excess air was extruded, and residue ink was removed by imbibition using a paper towel. The 37 °C embedding bath was put in place after which the UV-lights were deactivated, and printing was initiated.

The nozzle lowered into the embedding bath container to ±3 mm above its bottom. The build platform then moved 18 mm towards in the direction of the needle's bend at 3 mm/s followed by a 3 mm movement in the opposite direction at 3 mm/s. This last movement created an area of partially liquified gel at the needle tip, such that the bioink does not have to yield the bath when extrusion was initiated, resulting in a well-controlled and repeatable start. Following the same direction for 10 mm at 2 mm/s the bioink was extruded at a constant feed rate. The printer then slowed to 1 mm/s for 2 mm after which movement was halted for ±2 minutes. This was to; 1) minimize disruption by movement or local bath distortion during the most critical period of diffusion packing and 2) postpone te formation of a large region of less resistance towards the surface for the ink to flow into, and thus leave the intended deposition area. In most experiments a maximum of 3 lines were printed in parallel, separated by ±4 mm, in the same petri dish.

It was noticed that the difference in density between the liquid and solid components of the bioink was deemed significant over the timeframe of a printing session by resulting in a temporally inhomogeneous particle density extrusion when printing PLA-microparticles and paint pigments. The syringe was therefore carefully removed, shaken, and re-installed periodically every 3-4 minutes for homogenization.

3.6 Post print culture

The post-print culture of deposited cells was performed in the same manner through all experiments.
The constructs were printed and cultured in the same dish for the duration of the experiment incubating at 37 ℃, 20% O_2 and 5% CO_2.
Using a 1000 μL or 200 μL pipette, part of the embedding bath was carefully removed, avoiding the print area as much as possible, after which new cell type(s) specific cell medium or media was carefully added dropwise.
For; (a) iPSCs: SC-GM, (b) CMs: CM-MM, (c) mix of CMs & ECCs: 1:1 mix of CM-GM:ECC-GM, (d) SMC-spheroids only: SMC-GM2 (e) mix of μparticles & SMCs or SMC-spheroids: SMC-GM3.
The amount replaced depended on the stability of the constructs, their position in the petri dish and the (local) dilution of the embedding bath. The first refreshment, 24-36 hours after printing, allowed about 1/4th (1.5-2 mL) of the total bath volume (±8 mL) to be removed. Subsequent refreshments, focussing more on hydrogel removal and performed every 1-2 days until experiment termination, allowed slightly more volume to be replaced and present while staying 3-4 mm away from the deposited cells.
Often, especially in the first 2 days, the constructs' mechanical stability was not enough to withstand dragging forces generated during bath aspiration, leading to spreading of cells or breaking of constructs. In most lines a slight bend towards the aspiration area was also induced.
Sufficiently stable constructs could be manipulated or extracted with tools without breaking when the bath was sufficiently diluted (**Fig. 13**).
For testing the stability of PLA-μparticles in SMC-GM3, they were printed in 1/5% (w/v) XG/DPBS which was replaced by SMC-GM3 before a 3-day culture.

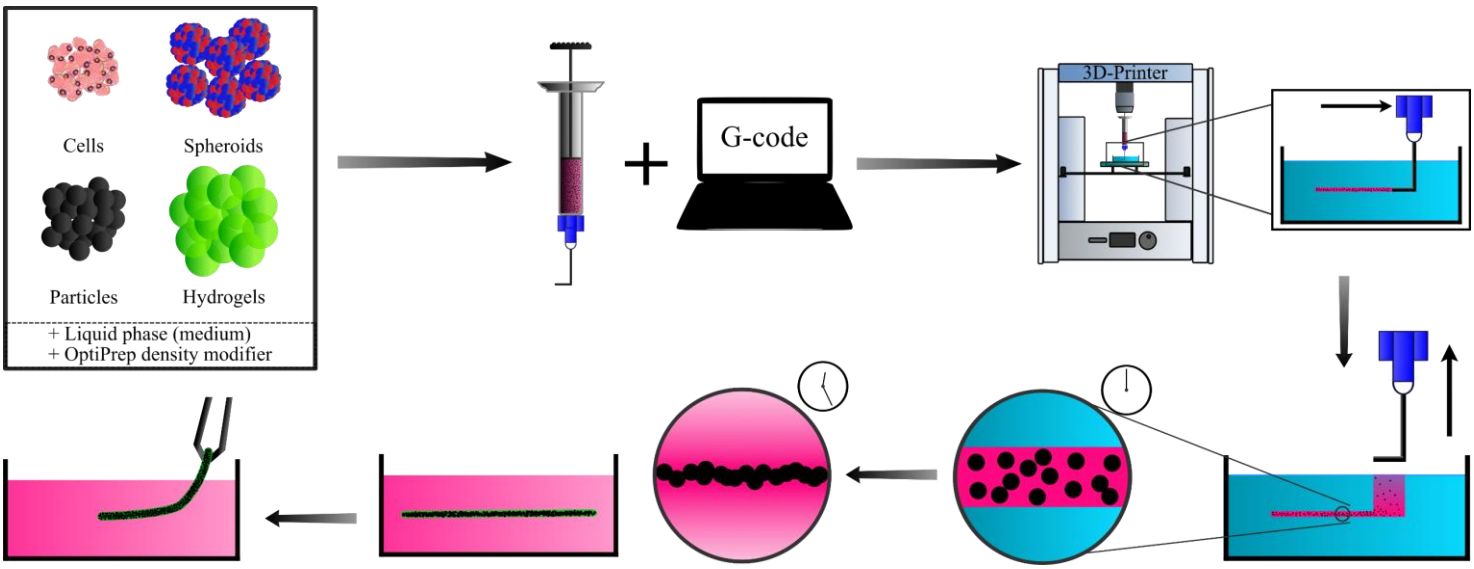

Figure 13. Schematic drawing of printing process and subsequent tissue formation and extraction

3.7 Imaging and analysis

3.7.1 Detailed imaging of 3D printing

The detailed fluid dynamic visualizations were V. Trikalitis and M. Kaya. This paragraph will go into the formulation of suspension inks and subsequent imaging and visualization of ink and embedding bath components, as described previously Trikalitis *et al*. (2023). [65]

Fluorescent particles for multicolour microscopy were fabricated by grinding fibres synthesized using electrospinning Polymer solution for electrospinning was prepared by dissolving polystyrene (PS) pellets (Sigma-Aldrich, 430102) in anhydrous N, N-dimethylformamide (DMF; Sigma-Aldrich, 227056- 1L). Coumarin 6 (Sigma, Aldrich, 442631-1G) was selected to make the polymer solution fluorescent since it is stable in PS matrix and has relatively high photobleaching resistance. For beaded fibre synthesis, 30.0% (29.8% PS and 0.2% coumarin 6) weight-to-volume ratio in DMF was prepared and homogenized overnight at RT using a tube roller mixer. The electrospinning process was performed with an acceleration voltage of 14 kV, solution feed rate of 2.5 mL/h, and needle (G18) tip-to-collector distance of 16 cm. [107] Randomly oriented fibres were deposited on a grounded aluminium foil at 24 °C and relative humidity of 22%. The deposited fibre meshes were cut into 2- and 3-mm pieces using a scalpel and transferred into a glass vial containing 1% (v/v) Tween 80 (Sigma-Aldrich, P4780) in Milli-Q water.

The grinding process, which mechanically breaks the continuous fibres using ultrasound waves, was performed using an ultrasonic cleaner (Branson, 2510) for 2 h to obtain fluorescent particles ranging in size from 5 μm to 65 μm Ø. Real-time widefield fluorescence microscopy was performed to visualize 3D printing during linear deposition of particles suspension inside the XG embedding bath using the setup shown in **Fig. 14**. In order to visualize XG through fluorescence imaging, it was stained with fluorescein sodium (Sigma-Aldrich, F6377). In-house fabricated coumarin 6-stained particles were placed in rhodamine B labelled Milli-Q water. Coumarin 6 and fluorescein sodium have overlapping excitation and emission spectra (**Fig. 6**). The concentration of fluorescein sodium in the xanthan was adjusted to be five times less than the brightness of the particles in the acquired fluorescence images. The difference in intensity levels enables the separation of the xanthan regions and the particles using a predefined thresholding value. The 10× and 2× long-working distance apochromatic objective lenses (Mitutoyo, Plan Apo) were employed to focus the excitation light to the nozzle tip in the xanthan bath and collect emitted fluorescent light for image formation, respectively, **Fig. 14**. [108] Upon the thresholding, images containing Milli-Q water, particles, and xanthan were encoded with red-black, green-black, and blue-black colour maps, respectively. Multicolour visualization of the 3D printing was acquired by overlaying these colours.

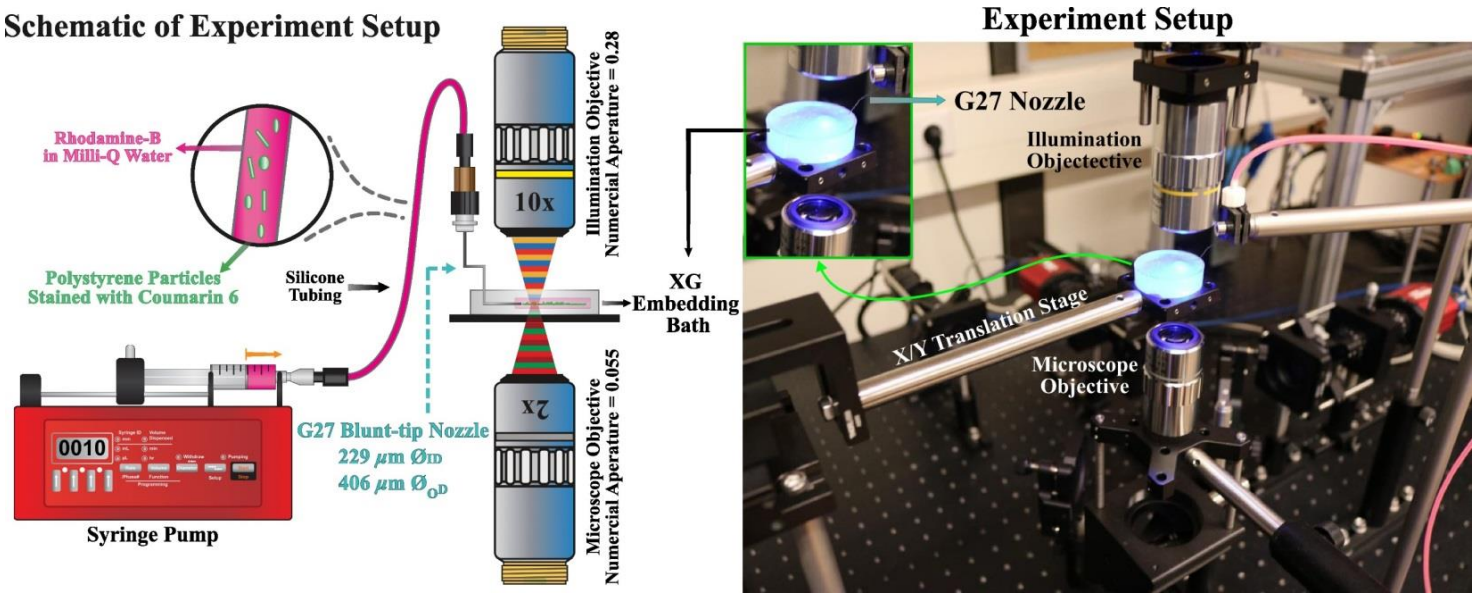

Figure 14. Custom setup for real-time microscopic imaging of 3D printing engineered and operated by M. Kaya. [65]

3.7.2 Imaging of printed tissues

Most brightfield and fluorescent images were taken using the EVOS FL (ThermoFisher Scientific) and EVOS FL Auto 2 (ThermoFisher Scientific). Brightfield and fluorescent images and videos of spontaneous and induced contraction of CM/ECC-tissues were captured using the Nikon ECLIPSE Ti2 (Nikon Instruments).

Confocal images were obtained using a Zeiss LSM800 confocal microscope (Carl Zeiss).

To obtain signal from fluorescent ECCs marker COUP-TFII locus bound mCherry 561 nm excitation (attenuator) and 579-696 nm range detection (645 nm gain) settings were used. These settings were also used for visualising mRubyII-α-actinin fusion proteins present in CM sarcomeres. The whole CM was visualised using the Alexa Fluor 488 nm excitation and in detection in 493-579 nm range (540 nm gain) settings for obtaining signal from eGFP present on the locus for cardiac marker NKX2.5.

For imaging the RFP in RFP-SMCs the same excitation wavelength as for mCherry was employed 561 nm and its emission was detected between 596-679 nm. To enhance SMC visualisation in constructs made from only SMC-spheroids, GFP was bound using immunostaining to cytoskeletal protein alpha-smooth muscle actin (α-SMA) using immunostaining. Its signal was obtained by excitation at 488 nm, detected between 513-560 nm, and combined with the RFP-signal when analysed and presented. DAPI in their nuclei was located by excitation with 405 nm and detection at in range 410-495 nm.

3.7.3 Tissue fixation & immunofluorescent staining

Tissues were fixated for analysis by first aspirating the medium and remaining embedding bath as much as possible, after which the tissues were washed once with DPBS. They were then incubated for 1 hour with 4% paraformaldehyde (PFA; Sigma-Aldrich, 252549) in PBS+ (PBS with magnesium and calcium) at RT, which was then aspirated before the tissues were washed with PBS+ twice for 20 min. This and the possible immunostaining performed after were executed in the darkness as much as possible.

Immunostaining of printed CMs/ECCs tissues was performed by starting with tissue permeabilization by incubation with a permeabilization buffer consisting of 0.3% Triton X-100 (Sigma-Aldrich, T8787) in PBS+ trice for 20 min. Non-specific anti-body binding was blocked by a 4 °C overnight incubation with blocking buffer containing 3% BSA, 0.3% Triton X-100 and 0.1% Tween 80 in PBS. The next day primary antibody mix containing 1:250 mouse anti-cardiac troponin T (CTT, ThermoFisher, MA5-12960) and 1:100 goat anti-TBX18 (Santa Cruz, sc-17869) in antibody buffer (0.1% BSA, 0.3% Triton T-100 and 0.1% Tween 80 in PBS+) was added for a 48-hour incubation at 4 °C. After washing 3 times for 20 min with permeabilization buffer, half of the tissues were incubated with secondary antibody mix containing AF488 goat anti-mouse (ThermoFisher, A11001) and AF657 goat anti-rabbit (ThermoFisher, A21244) and half the tissues were incubated with AF488 goat anti-mouse and AF546 donkey anti-goat (ThermoFisher, A11056) at 1:500 in antibody buffer for overnight at 4 °C. They were then finally washed with PBS+ trice for 20 minutes at RT and confocal imaging was or they were stored at 4 °C.

Similarly, tissues derived from SMC-spheroid were stained with 1:200 α-smooth muscle cell actinin mouse anti-human (α-SMA, Sigma, A2547) followed by 1:500 AF488 goat anti-mouse, and 1:200 DAPI (ThermoFisher, D1306) for visualizing their nuclei.

3.7.4 Data analysis

ImageJ/Fiji (NIH USA) was used for most image and video analysation. To give generate a detailed yet clear insight in general construct morphology, the ImageJ plugin Extended Depth of Field (EDOF, v2.0.1) was used to compact Z-stacks from transmission and fluorescent microscopy into a 2D images. Imaris Viewer (Oxford Instruments) was used for analysing and recompositing confocal microscope Z-stack data into EDOF representations.

3.8 Electrical stimulation of printed tissues

CM/ECC-tissues were electrically stimulated to control and evaluate cell contraction function, overall tissue contraction function and the intra-cellular calcium-induced calcium release (CICR) during cell membrane depolarisation. A 10ms biphasic electrical potential pulse of 20 V/cm was established over the length of these tissues floating in 1:1 CM-GM:ECC-GM at day 14 after printing, creating a different and well controlled frequency of contraction compared to its spontaneous rhythm. Pulsations at 1.0, 1.5, 2.0, 2.5, 3.0, 3.5 and 4.0 Hz were administered in sequence, with 2 minutes pauses in-between. Videos were obtained using the Nikon ECLIPSE Ti2 over a 10s period at 70 fps. Due to the tissue's elongated shape (3750 μm × 200 μm), shown in **Fig. 34.E**, the contraction was most pronounced along its main axis. In each frame, a certain group of pixels on its tips were tract, the separation between which were plotted as relative displacement (**Fig. 34.F**).

3.8.1 Calcium staining

To visualise the CICR during (induced) CMs/ECC tissue contraction, green-fluorescent calcium binding dye Fluo-8AM (Abcam, AB142773) staining solution was added to a 1:50 mixture of DMSO and HPSS (ThermoFisher, 24020117), to a concentration of 8 μM. The tissues' medium was aspirated after which they were incubated for 1 h at 37 °C in the calcium staining solution. The solution was then aspirated, a 1:1 mixture of CM-GM and ECC-Med was added, and they were imaged with the NIKON ECLIPSE during spontaneous and induced contractions.

Chapter 4. Platform Optimization

Although extrusion-based 3D-bioprinting is a rapidly developing technique, overlapping of many different fields Twente University participates in remarkably, such as complex tissue culture, bioengineering and microfluidics, this platform and the act of bioprinting were still novel to the researchers.
Developing insight into a platform, consisting of both performing novel procedures and utilizing new materials combinations, requires a stage of exploring platform characteristic based on alterations and observation. These findings and their implantation towards desired preferences can be regarded as platform optimizations albeit, in the scope of this thesis, they were quite limited. Findings relevant to obtaining satisfactory tissue printing results regarding bath composition (**§4.1**), bioink characteristics (**§4.2**), needle architecture (**§4.3**), feedrate and infill value (**§4.4**) needle movement characteristics (**§4.5**) and post-print culture and extraction (**§4.6**) will be discussed here.

Unless stated otherwise, the reference frame of the results depicted are such that the bath moved to the left, or the needle moved to the right, while printing.

Before exploring the platform optimization, the results of initial experiments have to be shorty addressed, which will discussed in greater detail in (**§6.2**).
Initial experiments showed the capability of very localized and well controlled deposition of bioink by a vertical straight needle. Subsequent diffusion packing formed a construct showing relatively good stability and shape fidelity. Printing with CMs in 3 layers separated by 200 μm, resulted in tissues 7-8 mm in length and 3-4 mm width and 0.4-0.5 mm in height pulsating as if forming a continuous structure in a timeframe comparable to monolayer cultures, a result which surpassed most optimistic predictions.
However, after the initial XG-stock was depleted and replenished, these early results couldn't be replicated.
Many parameters were altered greatly to do so, including:

- Movements speed
- Acceleration
- Jerk
- Ink temperature
- Ink composition
- Extrusion speed
- Bath temperature
- Bath concentration
- Bath liquid composition
- Needle hydrophobicity
- Needle size
- Bath height

Unfortunately, in all cases a deposition of thin ink column, reminiscent of a vertical sheet or wall, from the extrusion site to the surface was formed.
It was then hypothesised a secondary matrix was possibly originally present, acting as a strong net, capturing the bioink. Which sparked the idea of replicating such conditions with the inclusion of SA in XG baths. After failing to exhibit the desired properties in the tested concentration ranges and hydrogel ratios, changing the needle geometry was chosen with the aim of making printing without sheet formation in XG-only baths possible.

4.1 Embedding bath composition

As discussed in (**§2.1**), increasing the xanthan concentration in solution changes the rheological properties of which its shear thinning behaviour and viscosity are the most relevant to the extrusion bioprinting performed in this research. No in-depth rheological analysis has yet been performed on XG hydrogels made from cell culture media and it has been observed during this research that these properties differ significantly between different culture media at similar XG concentrations. The concentrations used in current embedding bath formulations are therefore subjectively selected and are kept constant between them, not because of consistent and desired rheological properties, but to form a baseline of expectations for each XG/medium combination, which can be used in future experiments.

The 1.5% (w/v) XG concentration used most often throughout this research is based on an observed balance between properties seen which differ between relatively high and low concentrations, which can be seen in **Fig. 15**. To low concentrations might result in insufficient mechanical resistance due to unmodified XG demonstrating low stiffness. For example, in the additional figures of Brassard *et al*. (2021), human intestinal stem cells tubular prints were more likely to collapsed into separate clumps at lower Matrigel concentration. [54]

The possible theoretical advantages for higher concentrations, which translates into higher viscosity and higher G' and G'', result in better localized ink retention by reducing its velocity a) after extrusion and b) during movement (e.g. transport), which can both lead to a better shape fidelity (for particular shapes), and c) even though full bath recovery might endure longer, the conditions at which ink is retained or extruded particle speed is significantly reduced, may restore more quickly.

Potential theoretical disadvantages are a) longer full matrix recovery resulting in a sustained crevices or localized area of partially liquified hydrogel allowing ink to depart, b) bath disturbances such as nearby needle movement and bath removal propagate further, potentially damaging for tissue shape fidelity and assembly, c) bath dilution has to be performed more extensively before a stable tissue can be recovered and d) diffusion limitations of both nutrients and waste products, both due to properties of XG hydrogel as well as higher XG densities in the tissue's proximity, limiting maximum cell density, metabolic activity and altering overall cell viability.

As can be seen in **Fig. 15.I-II** & **VI-VII** the 0.5% and 1.0% (w/v) XG/DPBS baths show streams of ink at the surface flow radially through shallow crevices formed by small irregularities at the baths' surfaces. Because the particles used in the ink were slightly denser than the fluid in which they were suspended, the observation they both propagate easily to the surface suggests a bath recovery too slow to retain the ink sufficiently. This was far less pronounced in 1.5% (w/v) XG bath which, combined with the potential disadvantages of even increasingly higher concentrations, was therefore chosen as the compromised standard XG concentration.

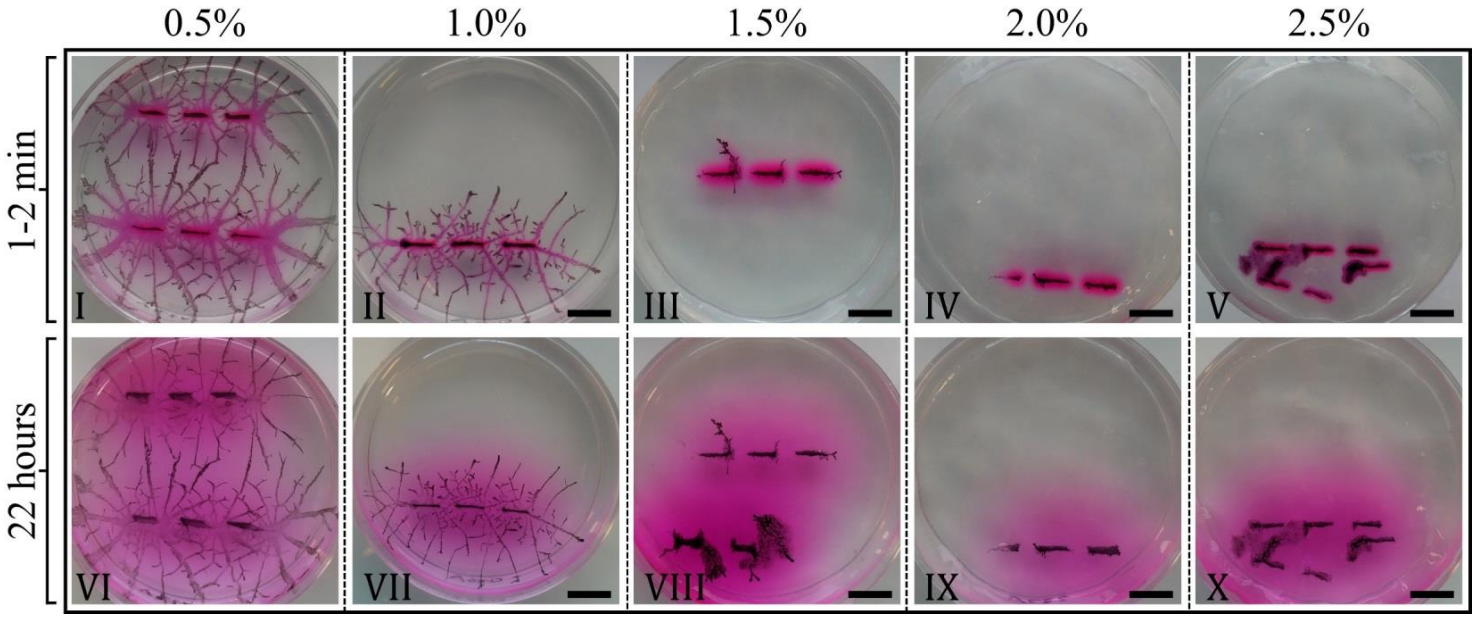

Figure 15. **Ink retention in different XG hydrogel embedding bath concentrations**. Using a straight needle (G22) ink, containing acrylic paint pigments and rhodamine, was deposited in 3 consecutive lines (5 mm, E100iOD) from left to right at RT. The XG concentrations from left to right were 0.5%, 1.0%, 1.5%, 2.0% and 2.5% (w/v) in DPBS. The top Row (I-V) show the results 1-2 minutes after printing and the bottom row shows the same samples after 22 hours at RT. Initially a decrease in diffusion speeds of rhodamine can clearly be seen with an increase in XG concentration. After 22 hours diffusion propagation distance does not significantly differ between the different baths. The extensions propagating radially from the extrusion sites in 0.5% and 1.0% bath, are irregular ridges at the surface filled with overflown ink and depositing particles and rhodamine continuously. Scalebars black: 10 mm.

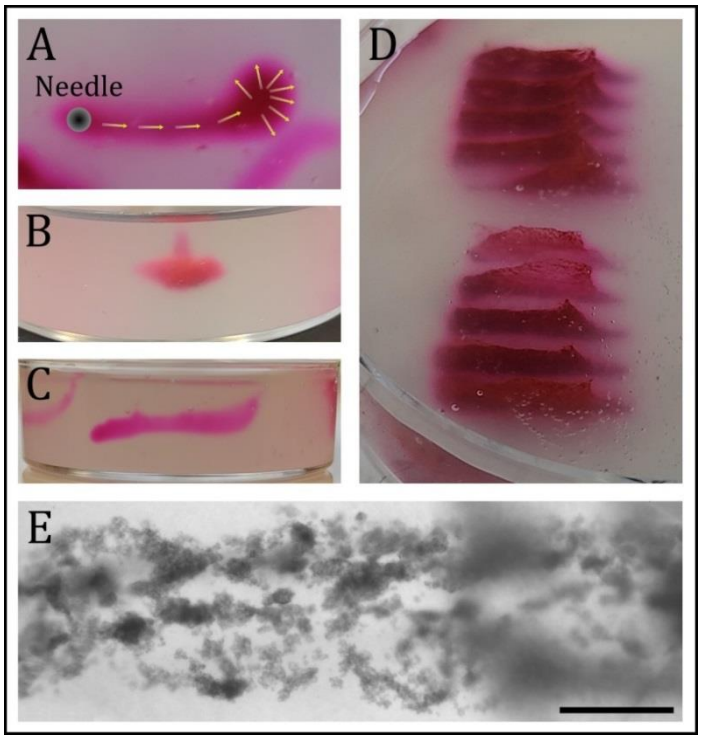

Figure 16. Demonstration of printing in mixed XG/SA Newtonian in either Milli-Q water (**A-C**, **E**) or DPBS (**D**) embedding bath using straight needles (G22). **A**) DPBS ink containing trace amounts of rhodamine extruded in 1.5%/1.5% (w/v) XG/SA in Milli-Q water with arrow indicating the direction of fluid flows. **B**) Shows the result of radial expansion during point injection. **C**) A free-hand attempt of matching extrusion rate with bath volume sheared by a moving needle, resulting in a suspended ink deposition. **D**) Sheet formation when printing horizontal lines at different extrusion rates in 1.5%/2.0% (w/v) XG/SA. Bottom 5 (Bottom to top); 2.14, 2.01, 1.34, 0.68, 0.33 μL/mm at 5 mm/s. And top 5 (bottom to top); 1.0, 6.0, 10, 15.0 and 20.0 mm/s with 1.34 μL/mm. **E**) Shows FLB-CMs printed in 1.5%/1.5% (w/v) XG/SA Milli-Q water after 1 day, no to limited compact. SB black: 500 μm.

To discover if the mechanism of diffusion packing can be used while also reducing the formation of sheets due to bath liquification around a vertical needle as a result non-Newtonian rheology, it was hypothesised a Newtonian bath made from a combination of XG and SA might have the desired properties. Milli-Q water mixed with a close to 1:1 ratio of these powders formed a quite clear, viscous Newtonian hydrogel from which air bubbles were easily removed and showed quick bath recovery after distortion. **Fig. 16** presents examples of the effect of printing in this embedding using a G22 straight stainless-steel needle. Its characteristics have distinct advantages and disadvantages over non-Newtonian XG baths. In **Fig. 16.A** the ink can be seen expanding radially from the initial injection site even after the needle is moved during extrusion, while in XG-based baths the ink normally follows the needle's wake and flows upwards. **Fig. 16.B** shows a similar result after point extrusion and **Fig. 16.C** a free-hand attempt to balance the extrusion rate slightly below the volume of bath sheared in the needle's wake with the intention of printing a line. Both produce a deposition area which is suspended freely inside the bath stably. Shown in **Fig. 16.D** are lines of pigments and rhodamine/water extruded in 1.5%/2.0% (w/v) XG/SA in DPBS with straight needle using different printing parameters. The bottom 5 lines printed with a decreasing extrusion rate; 2.14, 2.01, 1.34, 0.68, 0.33 μL/mm (b » t) at 5 mm/s. The top 5 lines were printed 1.34 μL/mm at increasing movement speeds; 1.0, 6.0, 10, 15.0 and 20.0 mm/s (b » t). Sheet formation could be seen in all conditions. A small chimney-like protrusion can be seen which is a result of the bath 'snapping back' after needle exit, showcasing the viscous drag established on its surroundings. Printing with a straight needle in a gellan gum embedding bath (0.5%, 1.0%, 2.0% and 3.0% (w/v)) resulted in similar vertical sheet formation (data not shown).

FLB-CMs printed in 1.5/1.5% (w/v) XG/SA in Milli-Q water show little to no overall compaction of the line after 1 day of culture as shown in **Fig. 16.E**. Also, ink flowing through the deposition area was clearly observed at least 10 min after printing concluded, suggesting poor bath absorption through diffusion. Hydrogel based on the polysaccharide gellan gum, at 0.5%, 1.0% and 2.0% (w/v), was tried in both DPBS and DMEM as well, to the same effects (results not shown).

Of note is the limited capacity at which these baths were explored during this research. Further experimentation with combinations and formulations of hydrogel-forming powders and its liquid component might therefore produce more desired properties. Although enhanced ink retention was clear, after the diffusion packing mechanism was not observed in the same extent, XG-based embedding baths were favoured for further study.

Further embedding bath composition optimization was performed by replacing CM-MM with CM-GM and SMC-GM2 with SMC-GM3 as its liquid component, for they were seen to be less viscous; improving both the removal of air bubbles and possibly bath recovery speed and decreasing bath distortion during agitation, although rheological experiments have yet to be performed.

The need for cell-specific culture media as the base for the embedding bath, which seem to produce gums exhibiting significantly distinct rheological properties, imposed restrictions on the tailoring to, and balancing between, desired rheological and biological properties.

4.2 Bioink characteristics

4.2.1 Suspension of imbalanced densities

The densities of suspended particles must match with the carrier fluid closely. Slight discrepancies will cause irregular extrusions over a significant period of time. In **Fig. 17.A** & **B** the alginate hydrogel particles, which are slightly more dense than the overall ink, will sink slowly forming clumps or clogs which results in (**A**) a inhomogeneous deposition and (**B**) a clog which caused a blow-out upon initiation. SMC-spheroid particles slightly differ in density between themselves, resulting increasing particle volume fraction over the duration of printing even after periodic re-homogenisation. **Fig. 17.C** & **D** are results from the same ink only the former had about a minute more settling time than the latter. Also **Fig. 17.C** was printed prior to **Fig. 17.D**, thus accounting for the densest spheroids in that printing session, which can be a result of their culture conditions including local confluency. [109], [110] A macroscopic example of mismatching densities between suspended particles is with printing iron oxides pigments. Most of them sink rapidly, while some, accumulated around air bubbles, float. **Fig. 17.E** shows there is period before full diffusion packing during which these particles separate clearly along these differences and thus will never form a stable singular structure. These observations emphasize the importance of achieving matching particle and carrier fluid densities and individual particle densities collectively. Using OptiPrep, (as discussed in **§2.5**), it was found that increasing the fluid's density to ±1.07 g/mL may stabilize the ink suspensions.

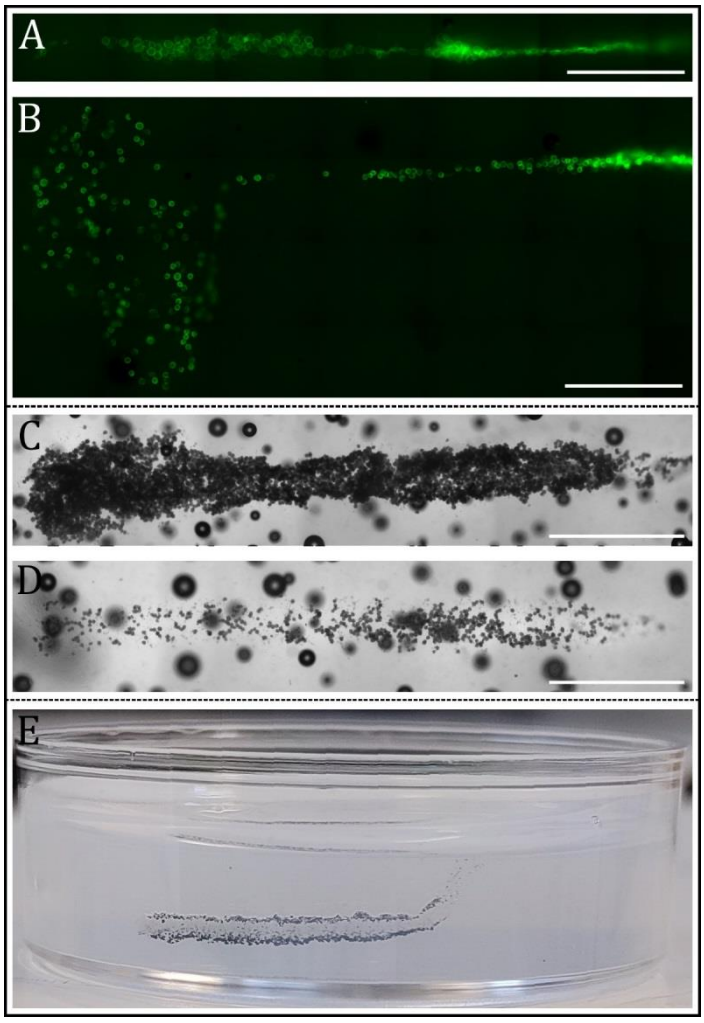

Figure 17. The effect of particle densities on print results. Mismatching ink densities with the particles it suspends severely impacts print fidelity. (**A**) More dense alginate hydrogel particles cause partial clogging or (**B**) clog the needle before printing, resulting in a bursting upon initiation. After every print of SMC spheroids, they were resuspended, however due to a difference in densities between spheroids, time differences of less than a minute can lead to vastly different particle extrusion rates: **C**) resuspension + 120s **D**) resuspension + 60s. **E**) A suspension made from particles with densities both above and below that of the ink separate in the ink-column before diffusion packing has finished. Scalebars white: 1000 μm.

4.2.2 Bioink composition

After the retention of bioink during and after printing proved difficult, using the setup of printing with a straight needle in a XG-based bath, utilizing hydrogel based bioink was explored. These can provide very stable materials which are studied extensively for 3D-extrusion bioprinting. Because the diffusion packing mechanism was most promising and deserving for further study, it was hypothesised XG could be used. This non-Newtonian suspension will liquified during extrusion and resolidify at the extrusion point, improving special retention and printed shape fidelity. Initially providing stability, extensive dilution may allow diffusion packing to ensue.

However, as mentioned previously the presence of XG between suspended cells greatly limits their motility and only chance encounters will lead to congregation. Careful and extensive dilution of the surrounding bath only mostly creates a dragging force separating the individual cells further. A demonstration in the form of a comparison between bioinks with or without XG hydrogel, is presented in **Fig. 18**. Hydrogel bioinks result in no clear overall compaction. Only very local accumulations of cells, whose presence are pronounced in **Fig. 18.V-VII** due to fast proliferations rates.

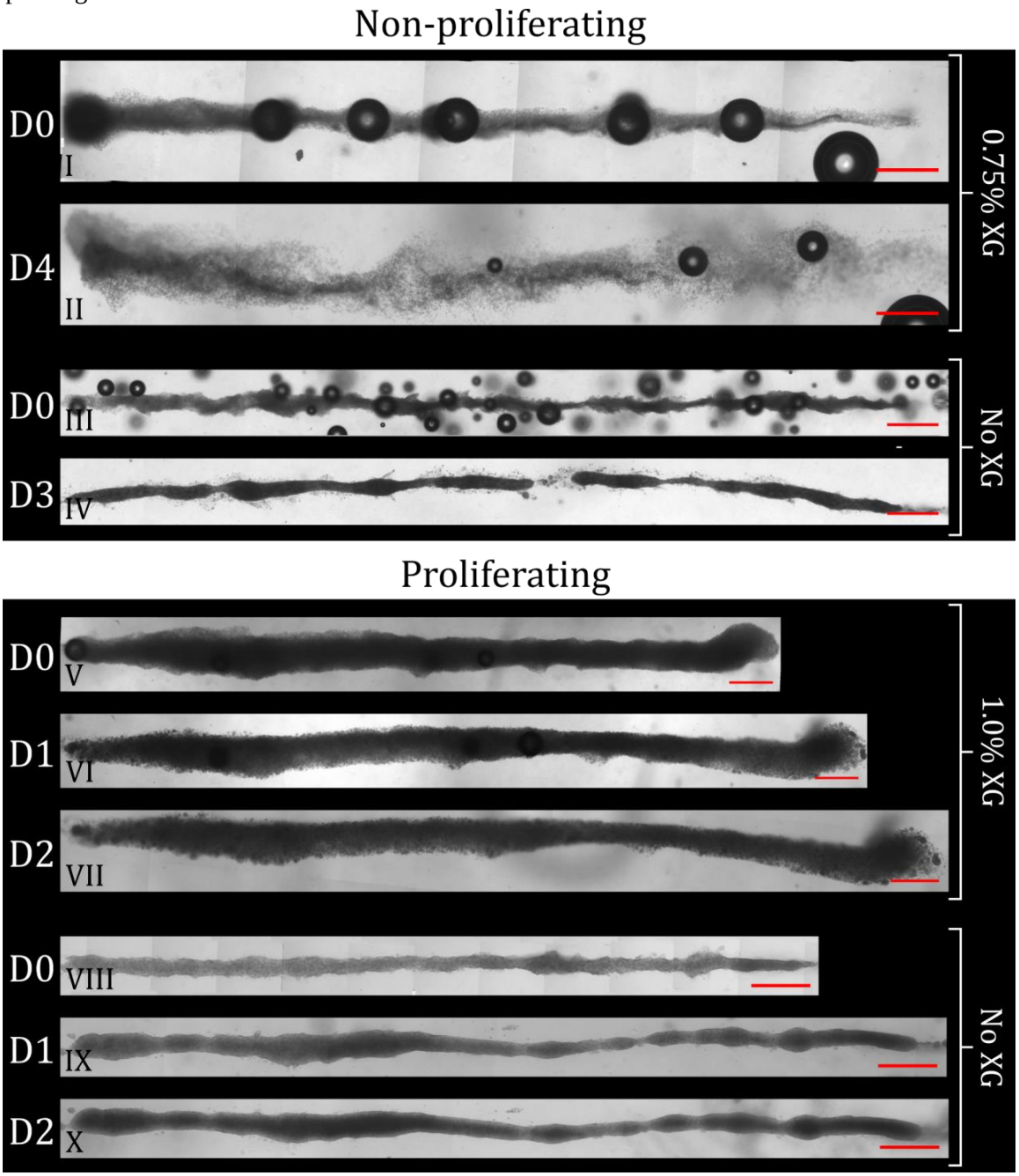

Figure 18. The result of printing proliferating and non-proliferating cell types suspended in bioinks supplemented with and without XG. (**I-II**) Non-proliferating CMs suspended in a 0.75% (w/v) bioink were printed in a 1.5% (w/v) XG-bath. Compaction was almost non-existent and spreading of cells can be seen to both sides the bath pas partially refreshed twice. (**III-IV**) Non-proliferating CMs and ECCs suspended in only medium and OptiPrep were printed in the same bath type which was partially refreshed twice as well. Although the line broke, clear compaction was observed. (**V-VII**) and (**VIII-X**) display the printing of proliferating C2C12 cells in 1.0% (w/v) XG and iPSCs SC in medium and OptiPrep respectively. Only very local compaction could be seen, forming small collections of cells but no increase in overall cell density was observed. This in contrast to SCs construct, which does compact radially, and subsequent cell proliferation causes an increase in both size and cell density. Scalebars red: 1000 μM.

A close-up example of this is shown more clearly in **Fig. 19**. Here C2C12-laden 1.0% (w/v) XG hydrogel suspension were printed in 1.5%/1.5% (w/v) XG/SA (**Fig. 19.I-IV**) and 1.5% (w/v) XG (**Fig. 19.V** & **VI**), in both cases showing only minor local compaction and density increases.
An additional drawback, that can clearly be seen in **Fig. 18.I**, is that during the mixing of particles in hydrogel, air bubbles are easily introduced which are difficult to remove, which will cause multiple issues during printing. Centrifuging result in inhomogeneous cell distribution and vacuum popping, practically boiling, is detrimental to their viability. The use of hydrogels bioinks thus also significantly complicates bioink preparations.

Further optimization regarding the bioink composition and properties were experiments addressing a possible limitation on φ_p. However, a consisted number of cells or particles of ideal density needed for such experiments were not readily available. For example; 250 μL is the minimal volume of bioink needed for a single experiment, 150 μL dead volume and 100 μL for printing, requires 54×10^6 C2C12 cells ($\emptyset_{avr}$ 13 μm) at φ_p 0.25, which requires resources beyond the scope of this research. The volume fraction was thus not optimized for the highest cell density sufficiently printable.

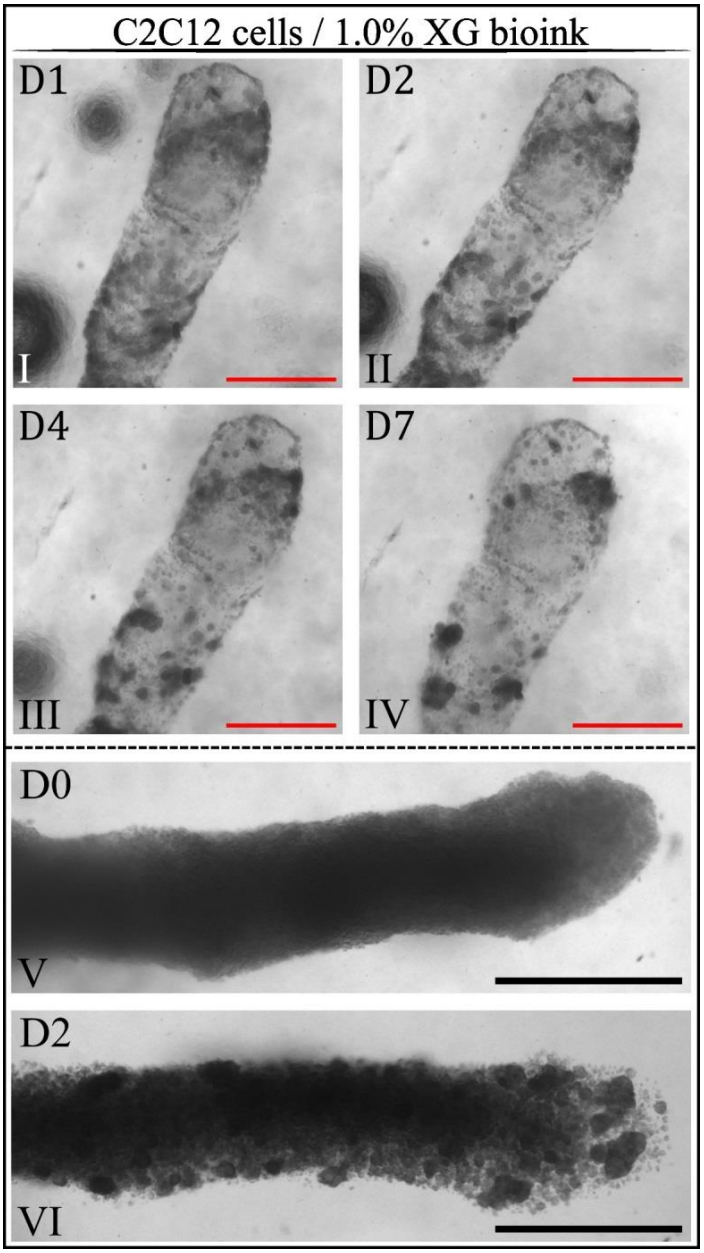

Figure 19. Close-ups of the non-compaction of hydrogel bioinks. (**I-IV**) C2C12 cells, suspended in a 1.5% (w/v) XG hydrogel bioink showed no noticeable radial compaction in a 7-day culture, during which the surrounding 1.5%/1.5% (w/v) XG/SA bath was replaced daily. (**V-VI**) C2C12 cells in the same bioink printed in a bath consisting of 1.5% (w/v) XG, resulting in only very local cell density increases by accumulation and proliferation. Scalebars red: 1000 μm, black: 500 μm.

4.3 Needle architecture

Most of the optimization of needle architecture has already been discussed the theory section's paragraph about ink tracing and filling of cavities (**§2.3**, **Fig. 4**).

With the aim of optimization and recreating the desired results observed in the initial experiments, multiple printing parameters regarding the needle's effect on bath liquefaction, ink tracing and deposition were tested. To the surfaces hydrophobic coatings were applied using 1) a silicon spray normally used for waterproofing fabrics and 2) alternatively a layer of polydimethylsiloxane (PDMS). Also needles made entirely from hydrophobic polytetrafluoroethylene (PTFE, Teflon) were tried. These approaches only reduced sheet formation in the first mm's after print initiation, before the surfaces were fouled by the ink or bath, after which no difference in performance with a normal stainless-steel needle was observed.

For reducing the size of the liquefied area formed by a moving nozzle, and thus reducing the duration of recovery after yielding, smaller gauges down to a G27 nozzle ($Ø_{OD}$ 406 μm), were tested to no significant change in results.

None of the methods tested decreased the formation of an ink sheet significantly, and thus experiments were preceded with blunt stainless-steel needles bend 90°, positioned inline to the direction of movement.

The restrictions and limitations this needle geometry imposed on the deposition orientation and final shapes were regarded less severe than those observed employing vertical straight needles, using similar embedding baths and bioinks, and their ability to repeatably deposit in straight lines, which could form stable tissue (fibres) after compaction and culture, was deemed sufficient for the scope of this research.

The two most important parameters hypothesised to affect the construct's initial diameter when printing a straight line were the 1) the needle size and 2) the infill value ($V_{ink}/(A_{needle} \times L_{path})$) (**§4.4**).

To determine the effect of needle sizes, lines were printed using the same infill value and movement speeds but two different needle sizes (G23 and G27). At intervals the cross-sectional diameter along their major axes were determined and graphed in **Fig. 20**.

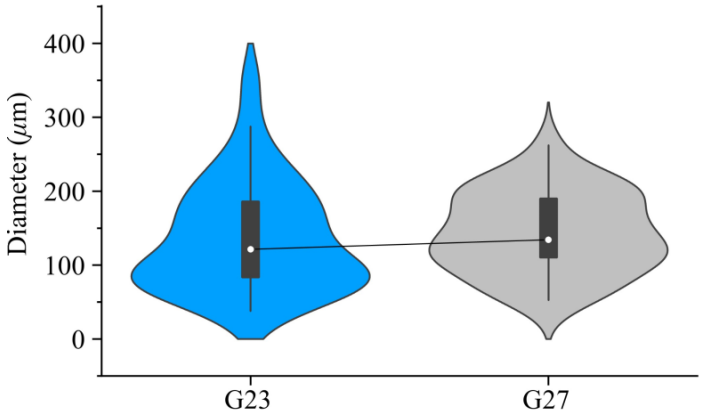

Figure 20. Graph displaying the cross-sectional diameter of lines printed with identical infill and speed values with a G23 and G27 90° bend needle. Bases upon own data, analysed by V. Trikalitis and reproduced from Trikalitis *et al*. (2023). [65]

Although the outer cross-sectional diameter of G23 is 56% larger over the G27 needle, comparing the overall distribution in their respective diameters indicates only a minor effect of needle size on these line dimensions.

As mentioned in **§2.3** the needle size imposes an upper bound to extrusion volume over a path of given length, also known as the infill rate. When ink volume extruded exceeds that of the cavity volume in the needle's wake, calculated as multiplying the path length with the needle's outer cross-sectional area, the chance of backflow increases noticeably. For every needle size there is thus a different infill-rate which matches the cavity volume, termed $E100\%$, which for G23, G26 and G30 is 0.32, 0.13 and 0.07 μL/mm respectively.

Note; for printing with a G26 needle, due to a technical error, g-codes designed for a G30 were executed. The result was therefore not fully representative and excluded from **Fig. 20**.

To determine the needle size best suited for printing a stable line in a repeatable manner for further experimentation iPSCs were printed using the E100% values of G23, G26 and G27 needles. A representative selection of the results can be seen in **Fig. 21.I-III**. The largest extrusion value gave the widest, longest continuous, most homogeneous, cell dense fibres and thus, G23 was chosen as standard in subsequent experiments.

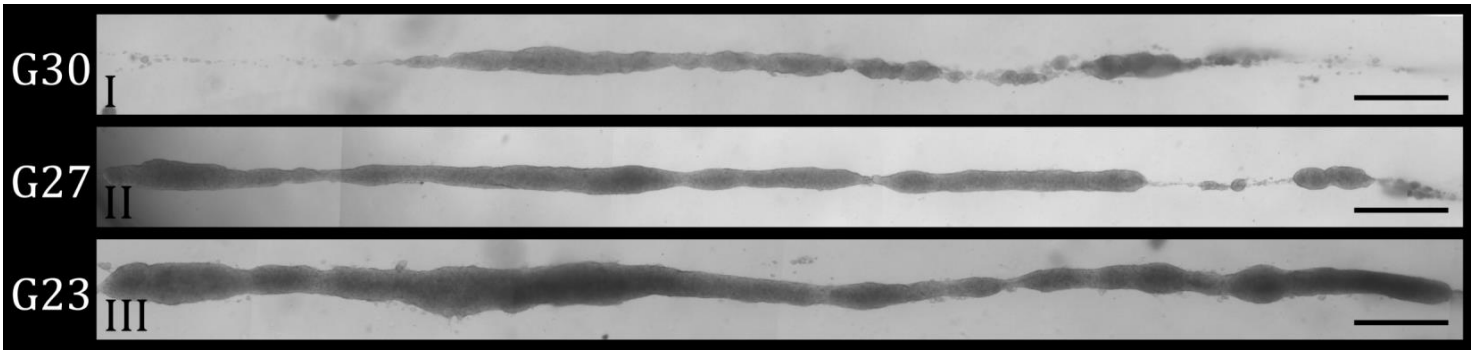

Figure 21. IPSCs bioink was printed using an extrusion value where extruded volume matched the bath volume displaced by a traveling needle. Depositions using E100% for a (**I**) G30: 0.07 μL/mm, (**II**) G27: 0.13 μL/mm and (**III**) G23: 0.32 μL/mm, showed a clear successive increase in line width and homogeneity.

4.4 Feedrate and infill value

Infill value (extruded volume over path length relative to needle size) and extrusion rate (extruded volume over time) can be easily controlled in extrusion printing. Because the amount of extruded volume, number of particles, and the compacted line thickness are directly linked when printing, within the platform limits as seen in **§2.3 Fig. 5**, a correlation can be formed between them. Keeping the syringe diameter constant at G23 but changing the volume extruded lines were printed with iPSCs (**Fig. 22.I-IV**) and PLA-μparticles (**Fig. 22.V-VIII**). A linear increase in infill volume leads to a linear increase in number of particles extruded. Plotting a compacted diameter of a representative line printed with the E50%, E100% and E150% infill values for a G23 needle, displayed in **Fig. 23**, shows a clear positive correlation. The average diameter, maximum diameter as well as its distribution all increase with a raise in volume extruded, to a significantly major effect compared to the increase in needle dimensions and corresponding extrusion rates, discussed in **§4.3**.

Thicker lines have the highest change to form a singular mechanically stable construct during culture and partial bath replacement. However, increasingly irregular width distribution at higher infill rates suggests the role of backflow or bath yielding by elevated ink momentum to reduce print fidelity at some point.
The effect of extrusion rates on backflow, previously discussed in **§2.3**, is shown in **Fig. 23**.

A note about the effect of feedrate on the printing process and shape fidelity regards the initiation. This can disrupt the deposition through two main events. 1) The initial resistance of both the bioink to be ejected, the plunger system, and the high viscosity hydrogel can cause a sudden increase in pressure and acceleration forcing the liquid out with enough momentum to shear the bath and be deposited far away from the intended area without any chance to compact sufficiently. 2) With particles there is always a potential of a (partial) blockage which resistance must be overcome, which can initiate or exaggerate the first event.
Although the 3D-printer recognises commands maximizing plunger acceleration and jerk, this command was not always adhered to. This unreliability had the potential to deviate from the settings required for the experiment waste many cells and embedding baths in the process. This point is also discussed in **§6.1.2** about limits in the 3D-printer used.

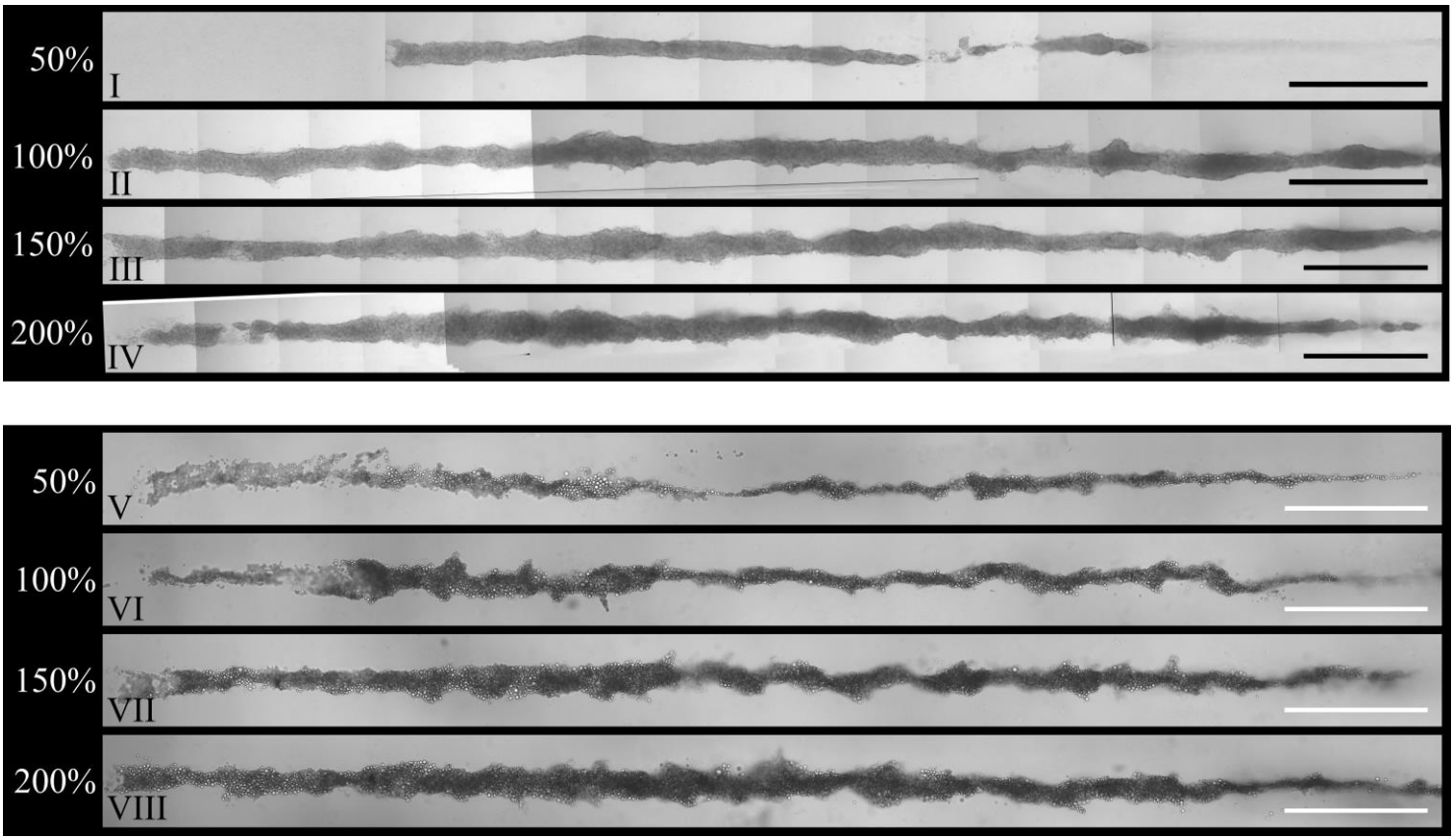

Figure 22. Increasing infill values correspond to increase line thickness and average line length. (**I-IV**) Lines consisting off iPSCs (D0) and (**V-VIII**) PLA-μparticles. Increasing the infill value led to a slight increase in average line section length. More pronounced was the average increase line thickness as well as the length of continuously connected sections after compaction. The infill percentage and corresponding infill rates were; E50% = 0.16μL/mm | E100% = 0.32 μL/mm | E150% = 0.49 μL/mm | E200% = 0.63 μm/mm. Scalebars black: 1000 μm, white: 2000 μm.

For these reasons, combined with the results from the previous paragraph regarding needle sizes and extrusion values, and this paragraph, regarding minimal and maximal infill values, show the largest needle tested to have the ability to most consistently and repeatedly deposit in a manner most likely to lead to the formation of a mechanically stable cellular construct with infill-rates at or around E100%, matching bioink extrusion with bath displacement. Reaffirming the choice to set G23 as standard in future experiments utilizing similar setups.

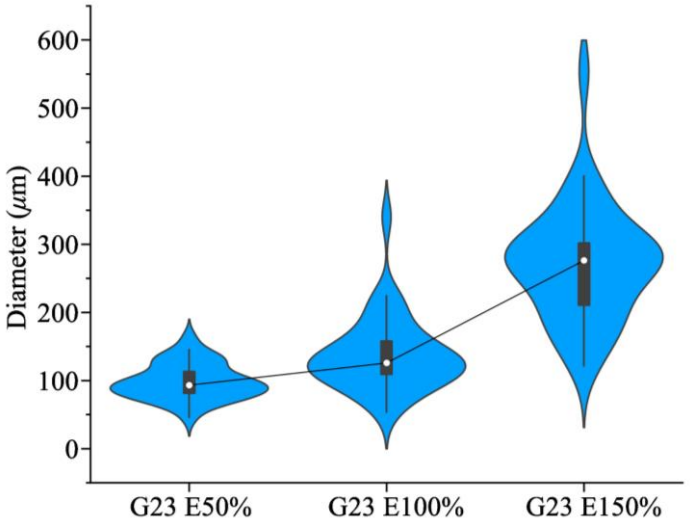

Figure 23. Graph displaying the effect of extrusion different extrusion values on the diameter of a line printed with a G23 90° bend needle. Bases upon own data, analysed by V. Trikalitis and reproduced from Trikalitis *et al*. (2023). [65]

4.5 Needle movement characteristics

Needle movement encompasses many aspects influencing printing results directly or indirectly. These can be classified in two main sections: A) Movement path geometry and B) Movement speeds and acceleration.

4.5.1 Movement path geometry

Most of the optimization of path geometry was to adopt the compromised movement restrictions imposed by employing bend needles. For deposition be most localized and performed in a repeatable manner this means movement in the direction of the bend parallel to the needle's horizontal component.
Building on this restriction, further improvements with the intent of improved shape fidelity and variety, and construct stability were tried, to an extent in scope with this thesis.

Increasing local particle density by depositing ink over the same area multiple times, both by moving the needle back and forth or by looping ~Bath entry → line deposition → bath exit~, was only very rarely accomplished. The perturbing side effects of large bath disruption, bioink displacement, and the introduction of interstitial XG outweighed the benefits of denser particle concentrations to some parts of the structure, when compared to the loss of numerous more distant and isolated particles.

Printing parallel lines in close proximity before mayor compaction, with the aim of forming a horizontal sheet, does not seem to be able to avoid intermediate XG and the necessity of printing very close to ink only deposited moments before, leads to inevitable bioink displacement. Examples shown in **Fig. 25** show the results of printing DPBS/Rhodamine-B (**A-B**), SMC-spheroids (**C-D**) and C2C12-cells (**E-F**). Although there are differences in rheological properties between the embedding baths used, the lines clearly more visible in the DPBS print compared to the SMC-spheroid and C2C12 prints are probably a result of the 800 µm vs 400 µm space between lines. This suggests a transition distance below which the deposition region regularly mixes. The first couple of mm's does seem to indicate the formation of a flat and wide geometry might be achievable, however the location of the needle's vertical component during repositioning does generate bath distortions and vertical sheet formation. Mechanically unstable sheets are relatively sensitive dragging effect of peripheral bath refreshment, which can be seen by the spreading of C2C12 cells from D0 and D1 (**Fig. 25.E→F**).

Sheet formation by slowly extruding while moving sideways, orthogonal to the needle's horizontal component, liquefying a horizontal flat region with the aim of generating a sheet also didn't show promising results as seen shown in **Fig. 24**.

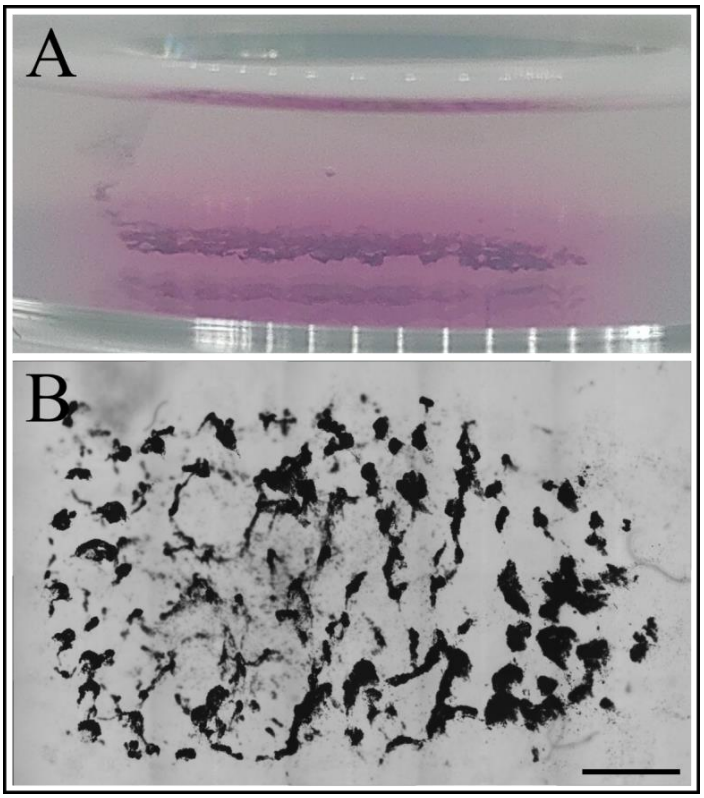

Figure 24. Extruding acrylic while moving orthogonal to the direction of needle horizontal component with the aim of sheet formation. However, this resulted in local accumulation and subsequent sinking of relatively heavy particles. Red arrow indicates the direction of movement. Scalebar black: 2000 μm.

Both methods used suffer from the same drawbacks; A) The chance of achieve a homogenous ink dispersion is very low. B) Because the particles used are often slightly denser than the embedding bath and bioink, accumulations of particles will form very slight but noticeable lower, sinking areas into which more particles to slowly flow. creating a positive feedback loop which leads to the unpredictable formation of large particle clumps as shown in printing acrylic paint particles **Fig. 24**.
As can be seen in **Fig. 25** some cells and spheroids do accumulate, albeit in a unorganized manner, which opens the opportunity for denser more complex tissues using higher φ_p bioinks in future optimization research.

Very briefly it was tried to form a tube with lumen by printing while the bath was moving in the opposite direction. But due to unpredictable deposition and the needle's vertical component causing sheet formation, this method was abandoned quickly.

These results show that the tested methods for creating more complicated designs which stray from the printing of a straight line cannot yet be reliably used for such purposes. The current setup is thus only optimized for the use of a simple path design describing a single free-floating line deposited by a straight movement of the bath in the direction of the needles opening.

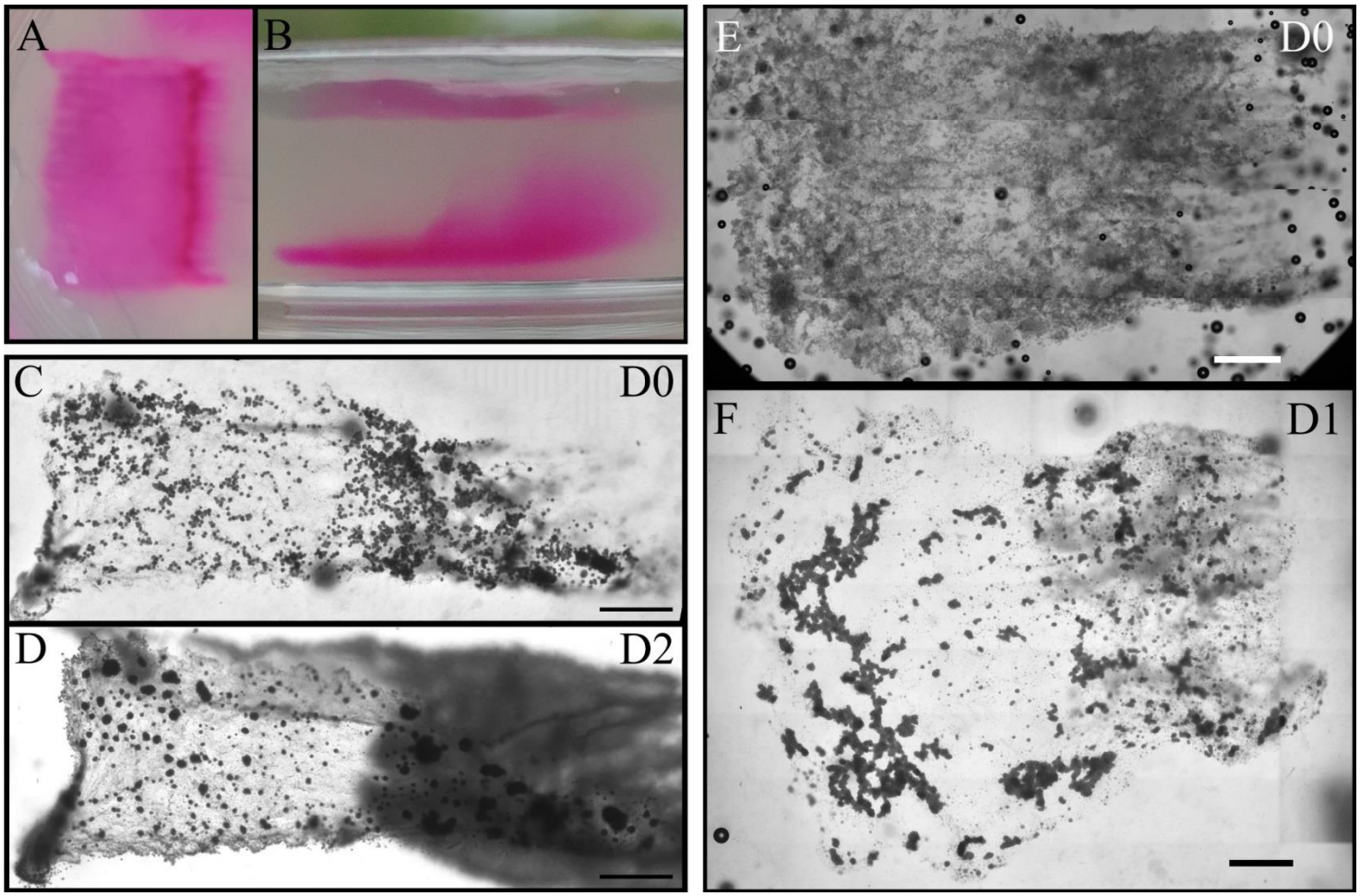

Figure 25. Methods for sheet formation. (**A-B**) 15 parallel 5.0 mm lines made from DPBS ink containing rhodamine B printed in 1.5% (w/v) XGD/DPBS separated by 800 μm. Distinct lines can clearly be seen, indicating minimal local bath distortion. Almost connected in the first mm's to a flat and wide geometry, the repositioning of the needle's vertical component during repositioning does generate bath distortions and vertical sheet formation further down the line. (**C-D**) 12x 11.0 mm lines consisting of SMC-spheroid bioink separated by 400 μm, extrusion only occurred in the first 5.0 mm. The dark area out of focus on D2 are spheroids proliferating quickly on the bath's surface, where oxygen is more readily available. (**E-F**) Using the same print commands; 20 lines of C2C12 cells were printed. Local accumulation of spheroids and particles in the first day(s) of culture can clearly be seen in both **C→D** and **E→F**. All scalebars; 2.0 mm.

To this end, slight improvements in path design for single line deposition, as schematically displayed **Fig. 26**, included; **1**) positioning the needle towards the printing site while submerged, avoiding bath shearing to surface by the horizontal component. **2**) begin movement 3 mm before initiating extrusion to create a liquefied area, requiring less initial extrusion force and thus blowout. **3**) extrude at 2 mm/s. **4**) Stop all movement immediately after finishing deposition to reduce disruption during the most critical and sensitive period of diffusion packing. **5**) traveling back horizontally for 3 mm before moving upwards, reducing the trailing of ink components.

Printing was performed very close to the bottom (1-2 mm) to maximise the vertical distance to the surface, beneficial for ink retention, and allow for the ability to perform sufficient microscopic observation. Too close to the dish' surface however and the cells or subsequent construct will touch the container may spread upon it rapidly, depleting nutrients, hindering observations, and disintegrating constructs.

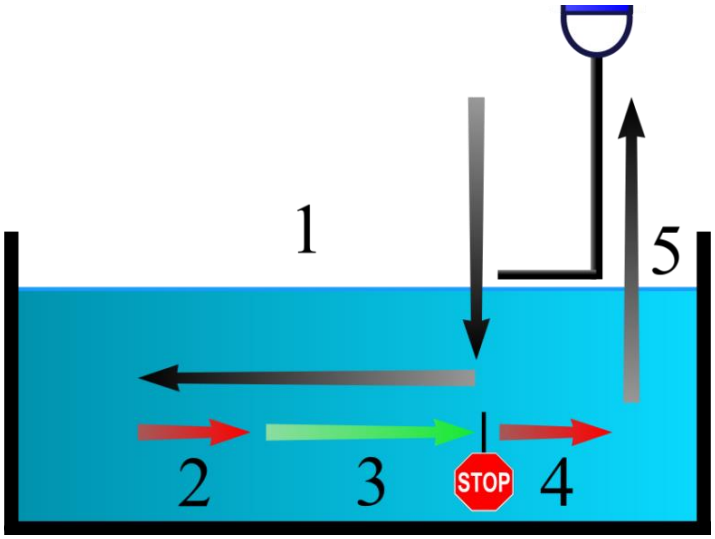

Figure 26. Line path optimizations. **1**) Enter bath at sufficient distance from the printing area and repositioning horizontally while submerged. **2**) Move 3 mm before print initiation without extrusion. **3**) Extrude for 10 mm. **4**) Stop and wait for 1-2 minutes before moving 3 mm without extrusion away from the printing area. **5**) Slowly leave the bath vertically.

4.5.2 Movement speeds and acceleration

Apart from traveling speed between two nodes, the maximum acceleration [mm/s^2] and maximum jerk [mm\s^3] could be set as well separately for moving in the XY plane, Z-direction, and plunger (extrusion), using the *M201*- and *M205*-commands respectively. These settings apply to de de-acceleration before reaching the next node as well.

Maximum acceleration and jerk have priority over the target movement speed, set by the *F*-value, which can cause the printer to reach start de accelerating or stopping before this speed is reached.

No command which can be utilized for extruding while stationary has been found to work on the printer used. Maximising the only movement acceleration low values while not restricting extrusion rate was tried for near-stationary extrusion, with the aim of large spheroid formation. In XG-based embedding baths, this resulted in ink flowing around the needle towards the surface. However, using a vertically position straight needle (G22), the formation of a spherical region consisting of rhodamine-B/DPBS expending radially in XG/SA-based bath, as seen in **Fig. 27**, indicate significant difference in hydrogel support behaviour with potential in for further study.

Of note is however the seemingly arbitrary implementation by the printer of these commands specific for acceleration. Sometimes they were not registered, and the printer proceeded at maximum acceleration. Other times it would not reset to a different set max acceleration, necessitating a complete restart of the system. The results therefore were quite unpredictable which made using these commands potentially wasteful for printing cell-laden bioinks and were thus not implemented in further testing.

Lines deposited at different movement speeds and thus extrusion rates were tested as well. It was first hypothesised the faster extrusion movement speeds allowed less time for ink to follow the needle and be displaced forming a denser construct of higher better fidelity. However, more significant result of higher movement speeds was a larger potential for ink blowout due to the sudden increase in pressure and acceleration by plunger initiation. Slower printing equalled lower extrusion rates and thus the comparably gentle second lowest printing speed of 2 mm/s was chosen during printing. Reserving the lowest 1 mm/s as a signal to the operator when extrusion was stopped, and the system was put on hold (**Fig. 26** step **4**).

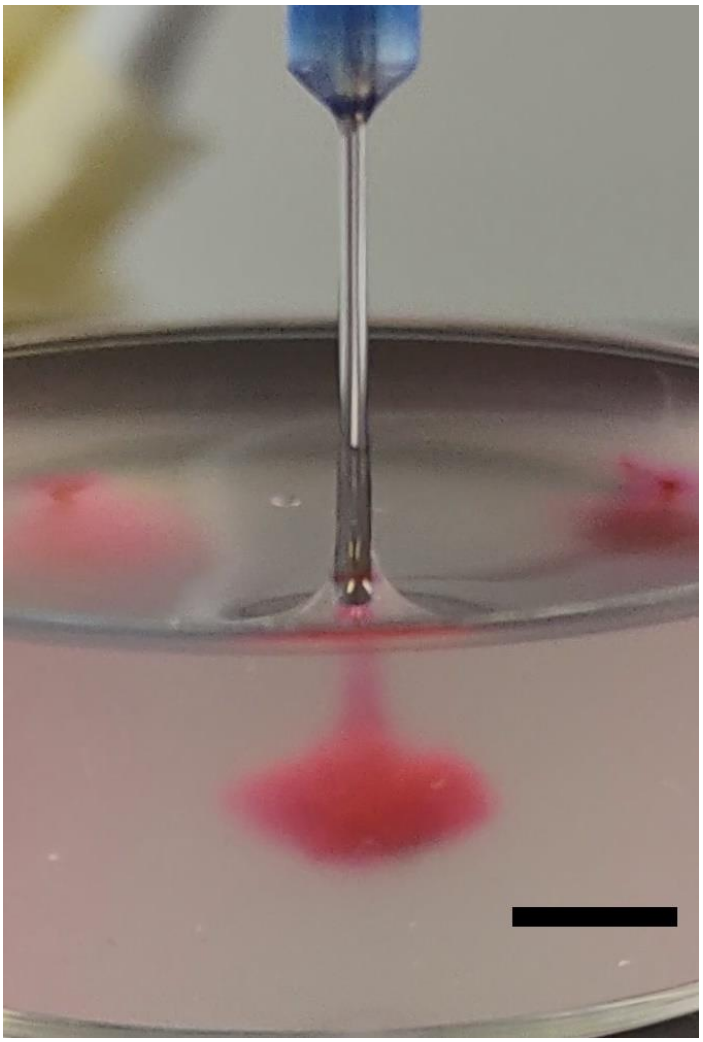

Figure 27. Near stationary extrusion Rhodamine-B/DPBS extruded in 1.5%/1.5% (w/v) XG/SA-Milli-Q water using a straight G22 stainless steel needle. Scalebar; 4 mm.

4.6 Post-print culture and extraction

The post printing culture and extraction has a lot of potential for optimization. The primary method used this research, whereby the embedding bath is carefully aspirated at the container's periphery, after which a comparable volume cell-specific culture medium is slowly added, underwent minimal optimization. This because very few of the printed construct had sufficient mechanical stability to endure full extrusion (virtually) intact, there was little opportunity to try out alternative methods, which are discussed in **Future Outlook**.
What was observed is that aspiration was best performed at speed, which locally liquefied the bath, while the print-containing area remained mostly solid and unaffected.
Increasingly diluted gel is affected more severely and at greater distance by peripheral removal, and thus a slower and more delicate execution is required.

This method has 2 main drawbacks. 1) The bath aspiration could be quite coarse compared to the fragility of constructs, and 2) the required time to fully free-up a printed construct can be a hindrance in certain experiments. Regarding both drawbacks the constructs' mechanical stability seemed to be the most crucial indicator for successful extraction, as seen in the prints performed with iPSCs, CMs/ECCs and especially SMCs.

Factors influencing the formation of cellular constructs of sufficient stability were;
1) Cell type, especially their proliferation rate and adhesion.
2) Initial cell density.
3) Extend of bath disruption during transport or refreshments.
4) Printed geometry, which only encompasses general length and thickness, but also homogeneity, which if not sufficient, may cause spontaneous break-up resulting from cell migration during compaction and reorganisation towards more cell-dense regions (**§5.4** & **§5.5**).
5) Fouling, e.g. intercellular presence of XG or cell debris, the latter of which steadily increases during culture.
And, if present;
6) Characteristics of co-printed particles, where particles harbouring cell-binding sites are integrated and become integral to construct stability.
The production of ECM, its composition and the subsequent adhesion sites probably also impact constructs stability, however no analyses regarding this aspect were performed during this research and thus will be part of future research.

Very stable constructs, formed by SMC(-spheroids), with or without the presence of PLA-μparticles, could be manipulated and picked up directly using tweezers or a spatula.
Slightly less stable construct could be delicately transported using a 1000 μm μpipette with a cut off tip, creating a wider opening.

Chapter 5. Results

Unless stated otherwise, the reference frame of the results depicted are such that the bath moved to the left or the needle moved to the right while printing, and the G23 90° bend stainless steel needle is used.

5.1 Printing particles-laden inks

Printing particle only laden inks was performed with large spherical alginate hydrogel μbeads ($Ø_{avr}$ > 90 μm), cell-sized PLA-μparticles ($Ø_{avr}$ ±30 μm), and acrylic pigment particles ($Ø_{avr}$ < 10μm).

For alginate particles the *neck-to-particle* diameter ratio was ±4.5, close to the transition value of 5 previously discussed in (**§2.2**). [59] Partial clog formation caused disruptive breaches at print initiation in some cases and intermittent extrusion flow in almost all. This resulted in lines with inconsistent cross-sectional diameters over their length (**Fig. 28.I**).

The result shown in **Fig. 28.III** was the last line printed before depletion of this syringe and all previous lines printed in the same session were almost devoid of particles. This dense line was the result of extruding the collection of particles slightly lighter than the carrier fluid, accumulated around air bubbles, residing near the top of the syringe. Also, different densities caused ascending and descending particles post-print, resulting in their large vertical spread, as can be seen in **Fig. 17.E**.

The PLA-μparticles densities were closer to the carrier fluid and those of cells than the heavier alginate and lighter paint particles, resulting in more regular and higher fidelity lines resembling those comprising cells presented later.

During all prints, diffusion packing occurred, reconfirming that when inks where the primary carrier fluid has water-like rheological properties, the local concentration of particles or cells will passively increase, when initially harbouring a sufficient particle density, through this process facilitated by XG-hydrogel embedding baths.

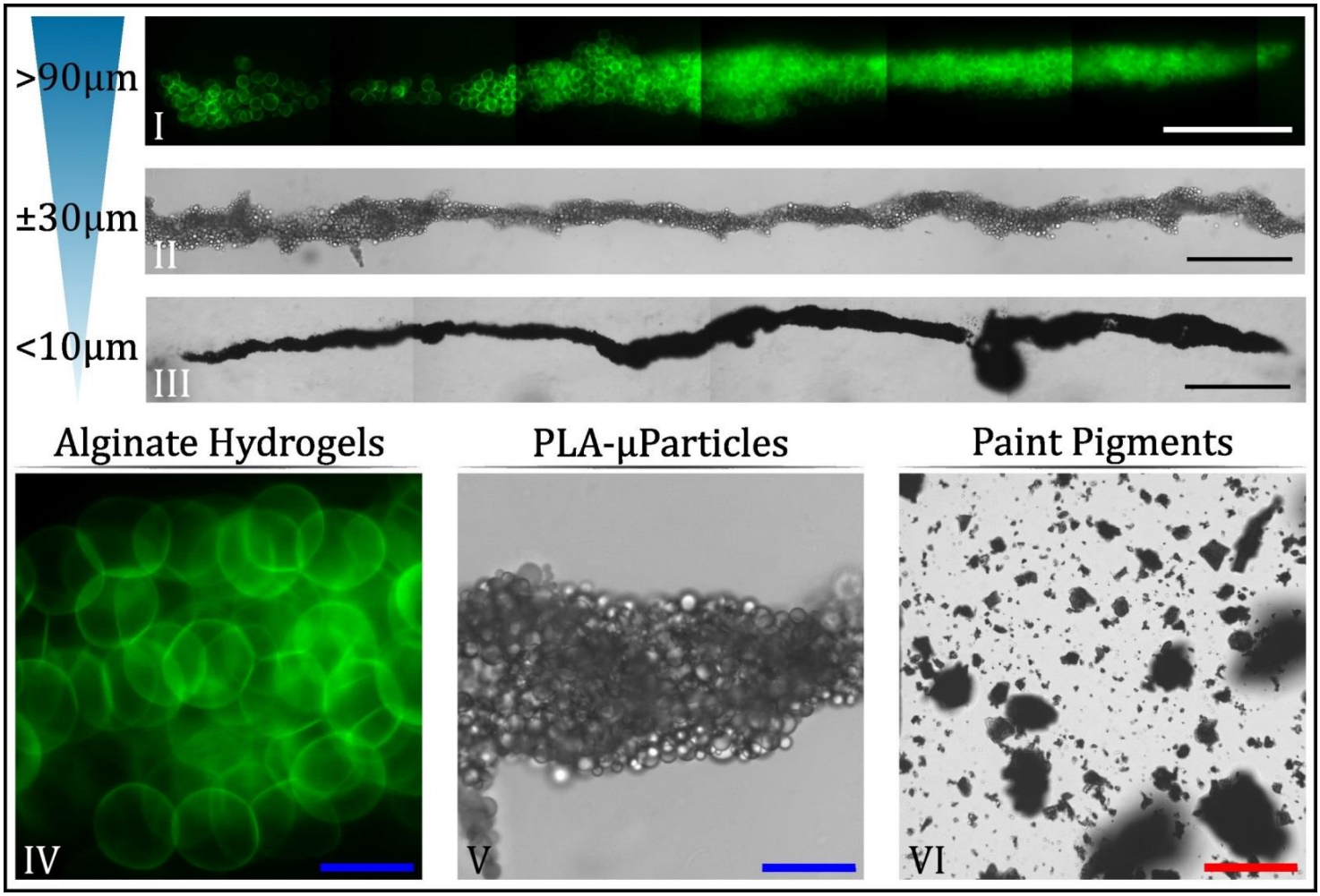

Figure 28. Results of the printing and subsequent compaction of particle laden inks. **I** & **IV**) In a 1.5% (w/v) XG/DPBS bath, the largest particles printed were FITC-labelled alginate hydrogel microbeads of $Ø_{avr}$ ±160 μm with the smallest being just over 90 μm in diameter. Seen here at E100% but more pronounced at larger infill values, an irregular extrusion due to intermitted clogging caused by either size and/or particle sinking was observed. **II** & **V**) PLA-microparticles of $Ø_{avr}$ ±30 μm, comparable to large cells, were printed at E100% in 1.5% (w/v) XG/DPBS. **III** & **VI**) Acrylic pigments suspended in 45% DPBS. 40% OptiPrep and 10% rhodamine-B, printed in 0.5% (w/v) XG/DPBS. Polydisperse in size, but most Ø<10 μm, and significantly denser than water, resulted in irregular extrusion. Diffusion packing was observed with all particles in most dense areas, which had the ability to partially correct irregular extrusions, and interconnected lines with quite constant diameters could still be achieved. Scalebars white 2000 μm, black: 1000 μm, blue: 200 μm, red: 100 μm.

5.2 Printing proliferating cell-laden bioinks

The fast-proliferating cell types C2C12-cells, RFP-SMCs, and WTC-iPSCs, were printed.

As mentioned previous (**§4.2.2)** part of the bioink optimization consisted of the printing with a C2C12-laden non-Newtonian bioink containing XG to ascertain if proliferation rates might allow cells to traverse, at least partially, interstitial hydrogel and thus linking separate cell (clusters) and thus creating larger structures created from more stable hydrogel bioinks. As also shown in in**. Fig. 19**, is the resulting formation of separate high cell-density clusters which, even though they generally increase in size due to proliferation, only form physical contact with adjacent structures due to rare chance encounters, insufficient for reliable tissue formation.

SMCs were printed as spheroids or in a mix with PLA-μparticles which will both be discussed separately in **§5.4** and **§5.6**/**§5.7** and respectively.

Fig. 29 show the result of E100% print of a φ_p 0.075 with G27 needle followed by a 7-day culture, during which 1/3 medium change every 2 days. The development of this line is representative of other lines printed with G23, G26 and G27 during the same session. The dense collection of cells quickly accumulated in a line shape by diffusion packing. At D1 the constructs' surfaces were already smooth but inside separate cell accumulations could be distinguished (**Fig. 29**.**V**). In the following days of culture, the cell population increases noticeably, increasing the average line cross-sectional area. **Fig. 29**.**V-VIII** depicts the development of a narrow low cell density section, prone to necking and breaking during bath movements, into one that is mechanically stable. This shows a possible advantage of printing proliferating cell types over non-proliferating species, for they can have a greater ability to heal and reinforces mechanically weaker sections.

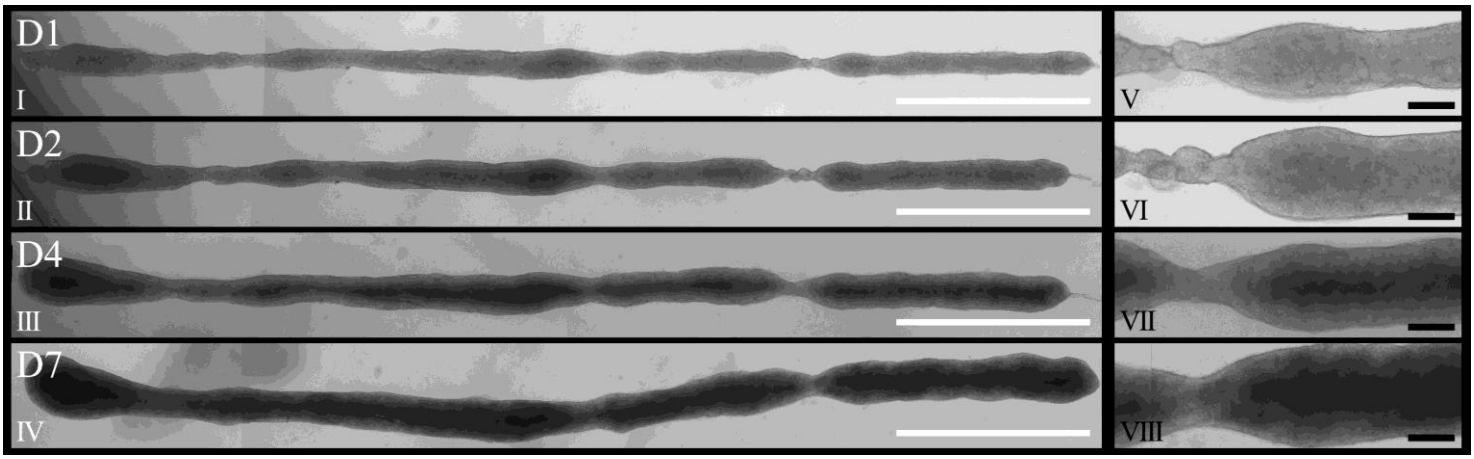

Figure 29. Culture of a line printed from WTC-iPSCs (P40+12, φ_p 0.075) in 1.5% (w/v) XG/E8-medium. Imaged at D1, D2, D4 and D7. **I-IV**) A timelapse of the development of the full line with increase line thickness and less light penetrating due to a gradual increase in cell numbers with minor increase in line length. Slight bending on D7 is caused by to bath replacement. **V-VIII**) Focusses on a section harbouring a low cell number, resulting in very narrow feature, which could form weak spot. Increasing cell population by cell proliferation and/or reorganisation reinforce this over the duration of culture. Scalebar white: 2000 μm, black: 200 μm.

5.3 Printing non-proliferating cell-laden bioinks

Here the result of printing CMs suspended in a CM-MM-based bioink at φ_p 0.064 is discussed which had the problem of intermittent clogging and extrusion due to the presence of fouling by fibres and (cell) debris (**Fig. 30**). This poor shape fidelity can be used to show one of the major drawbacks of printing non-proliferating cell species, for the abilities for cells to reorganisation can be often insufficient for correcting printing imperfections and sub-optimal cell densities on its own. The overall structures geometry and relative cell spacing remained quite static over the culture's duration (**Fig. 30.I-III**).

Areas which did not contain cells or in which cells were separated after diffusion packing was finished remained as such. In more cell dense regions, the limited development of continuous and smooth structures could be observed (**Fig. 30.IV-VI**). Most of these dense accumulations, which could reach were several 100 μm's in length, were seen to start contracting spontaneously at 0.2-0.5 Hz, between D5 and D6.

However, when these results are compared with those of fast proliferating cell species in the prior paragraph, printed with bioinks of only slightly higher φ_p, the relative sensitivity to final cell concentrations and the properties arising therefrom become clear.

If some inconsistency during printing, movement during transport or bath replacement, or cellular reorganisation causes the separation of cells or breaking constructs, the chances these will reconnect is low.

This delicacy is best compensated by the use of a higher φ_p bioink. This is done in a series of experiments that will be discussed later (**§5.5**), in which stable dense tissue fibres were formed from a bioink comprising only non-proliferating cell species at double φ_p.

If the build-up of intra-cellular debris and declining cell numbers are not compensated by the formation of intercellular bonds and/or the production of sufficiently stable ECM, in can be expected constructs consisting exclusively of non-proliferating cell types will diminish in mechanical stability after a certain optimal culture time.

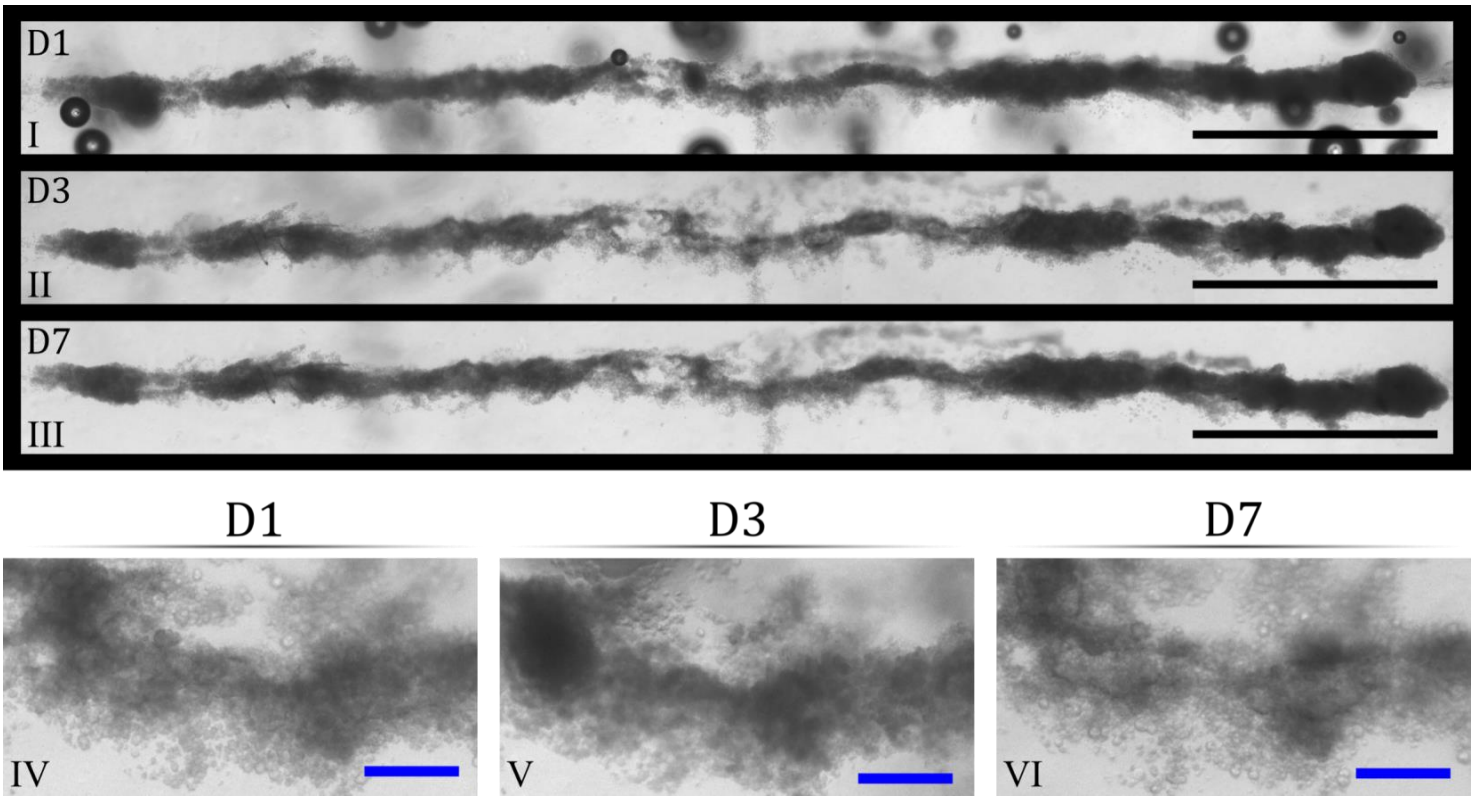

Figure 30. Printing and subsequent culture of thawed non-proliferating iPSC-derived DRRAGN CMs (P20+33). A bioink of φ_p 0.064 ($\emptyset_{avr}$ 19.9 μm) was extruded at E150% in a 1.5% (w/v) XG/CM-MM bath. **I-III**) Depict a time lapse of D1, D3 and D7 culture, showing the relatively stagnant geometry of the structure. **IV-VI**) Show a relatively high cell density area in the middle from which a smooth and continuous structure forms (±800 μm) which started contracting spontaneously at D7. Scalebars black: 2000 μm, blue: 200 μm.

5.4 Printing SMC-spheroid-laden bioinks

Several advantages were hypothesized when printing a spheroid suspension over a separated cell laden bioink. Due to their relatively larger size their travel distance between the initial extrusion location and final location prior to diffusion packing could be smaller, for they experience greater drag forces and for travel they require more carrier fluid, which is rapidly absorbed into the surrounding bath. Their mechanical stability and quick harvesting method also allows the preparation of high φ_p and relatively 'clean' bioink, being almost devoted of debris, often seen as a byproduct of the process of dissociation, which can cause cell accumulation and clogging.

To test this proliferating RFP-SMC were cultured into spheroids, being fluorescent making cell location and potential reorganisation distinguishable.
3-5 minutes after the bioink laden with SMC-spheroids ($\emptyset_{avr}$ 110 μm) suspended in a SMC-GM1, was loaded in the syringe, 3 separate bands could be discerned in the suspension. A pinkish deposition could be seen laying at the bottom, around the middle a suspended band accumulated and at the top floated trace amounts of foam with pinkish hue. During printing, every 3-4 minutes the syringe was carefully shaken for homogenization. Although clear indication of clogging was observed, the average deposition rate remained poor until the last E150% extrusion, where it is expected the spheroids which accumulated around the syringe's bottom ridge were squeezed through, resulting in a very high particle density print (**Fig. 31**). Discarding the failed prints, this dense tissue with a clear deposition gradient, was kept in culture for 10 days to track its development and make predictions about future SMC prints incorporating PLA-μparticles.

The separation between the outermost spheroids reached up to 2100 μm moments after deposition, however diffusion packing caused all but a handful to condense into the same structure, amounting to a huge increase in local cell density.
Over the following days construct compaction progressed and the line length decreased from 13 mm to 10 mm, 9.3 mm, 8.1 mm, 7.3 mm and finally 6.1 mm at D0, D1, D2, D4, D7 and D10 respectively. Meanly by what appeared to be the dissolution of spheroids.

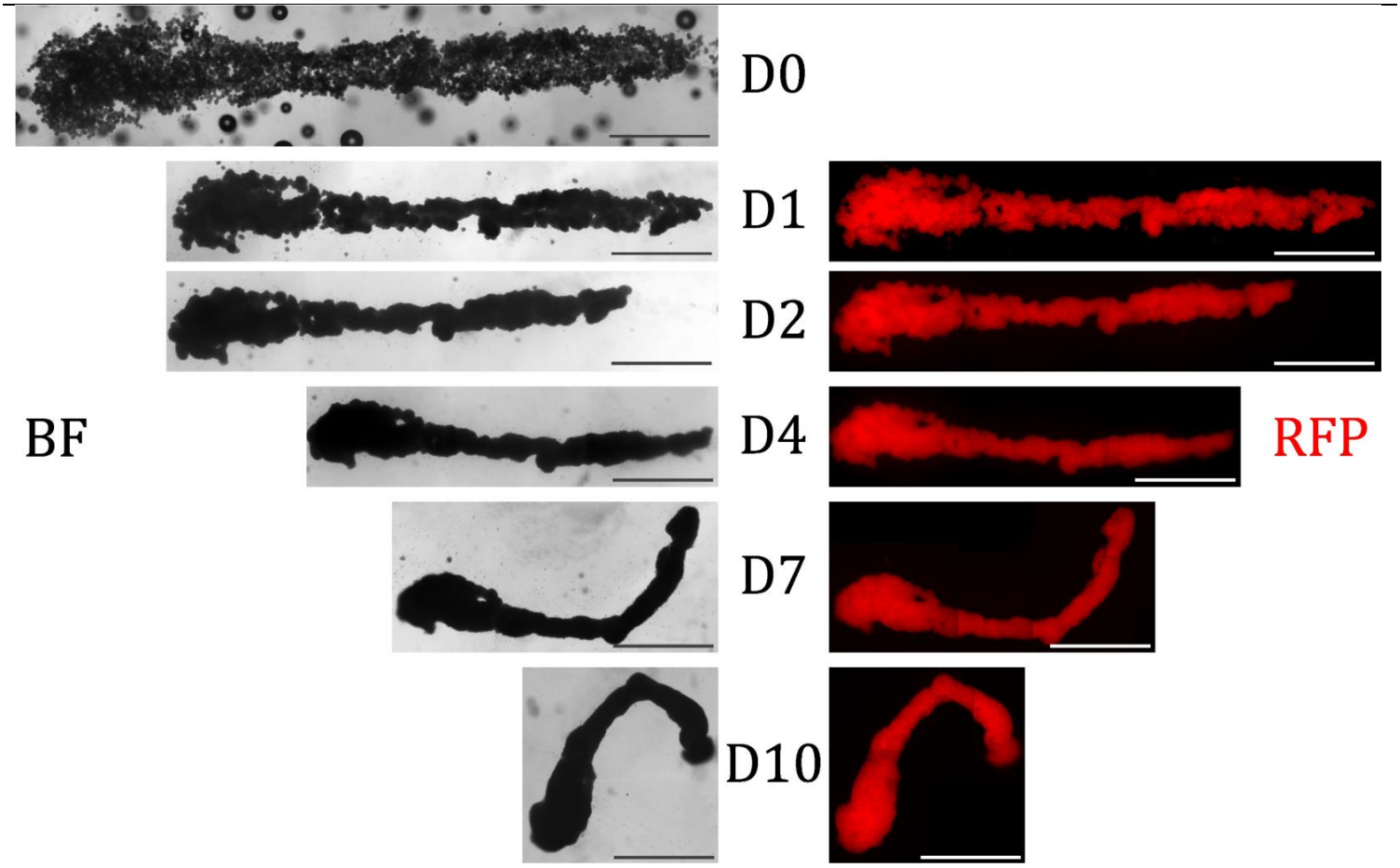

Figure 31. Timelapse of the formation of a construct formed by the printing and subsequent culture of SMC-spheroids over 10 days. The spheroids, only minutes after deposition on D0, accumulated radially by way of diffusion packing. In the following days, the spheroids merged while the SMCs proliferated. With increasing compaction and reorganisation, the construct's geometry condensed, its surface became more regular and variations in its cross-sectional diameter appeared to decrease. The slight bend observed at D7, formed spontaneously but was aggravated by the construct wrapping around the tweezer used to pick it up, the result of which could be seen at D10. Scalebars white and grey: 2000 μm.

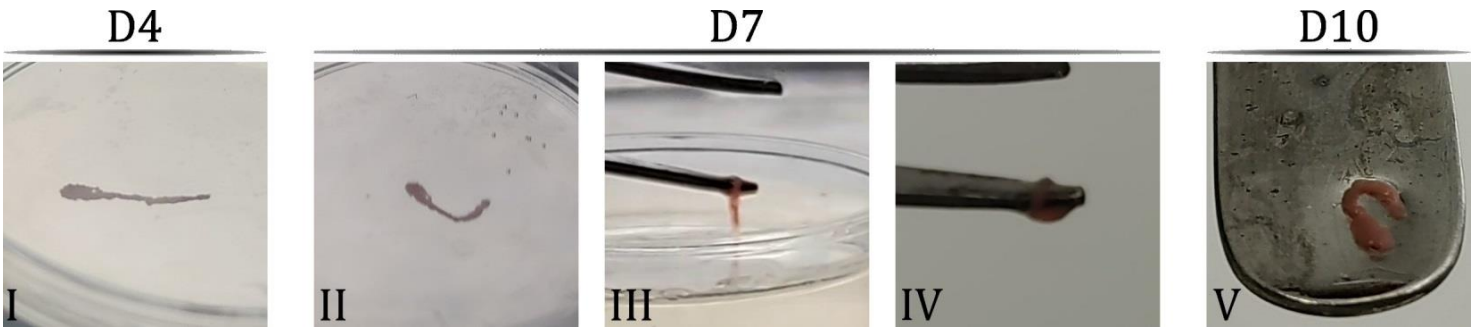

Figure 32. Macroscopic images of the development SMC-spheroid construct. On D7 both the construct was stable enough and the bath was sufficiently diluted to allow it to be picked up for which tweezers were used. Before this mechanical manipulation, there was already a slight bend forming which became more pronounced during the days thereafter.

The average line width first decreased from $1.3\pm0.3\times10^3$ μm to $8.1\pm3.0\times10^2$ μm, $7.5\pm2.7\times10^2$ μm, $6.6\pm2.5\times10^2$ μm, $6.2\pm2.5\times10^2$ μm from D1 to D7, after which it increased to $6.4\pm2.2\times10^2$ μm at D10.
Meanwhile the standard deviation between line width measurements decreased between every measured timepoint, due to the reorganization combined with cell proliferation caused the surface to become smooth and cross-sectional diameter to become more regular.

On day 7, the bath was deemed sufficiently diluted, and the construct was assumed mechanically stable enough to allow mechanical manipulation with tweezers (**Fig. 32**). This didn't seem to stretch or damage the construct and thus manipulation progressed to lifting it out of its embedding bath when, upon doing so, the tissue wrapped around the tweezer. After lifting from free submersion 2 times in 1 minute, an already present bend became more curved (**Fig. 31** & **Fig. 32.II-IV**), and slightly more pronounced in the following days (**Fig. 31** & **Fig. 32.V**). This could be due to a spatial imbalance in cellular orientation or proliferation, or the result of pulling forces generated by the SMCs acting upon the inside of this curve. After this, no external damage could be observed.

Fig. 33 extended Depth of Field (EDOF) composition images, generated form confocal Z-stacks of the tissue fixed at D10, show part of the overall structure with the cytoplasm of SMCs in **red** (RFP) and their nuclei in **blue** (DAPI). The signal depth was limited to ±65 μm from the surface, or up to 2-3 layers of cells, where it showed almost all aligned parallel to the construct's major axis, meaning that they are probably sensitive to and act according to external mechanical forces. This was not distinctive to more narrow and straight segments, as for in the sections where the line was widest at the ends, groups of cells seem to arrange around narrow or protruding features in an organised manner as well.
This suggests that the cell have the ability to be sensitive to, and accordingly act upon, external mechanical forces, causing an aligning cellular re-orientation.

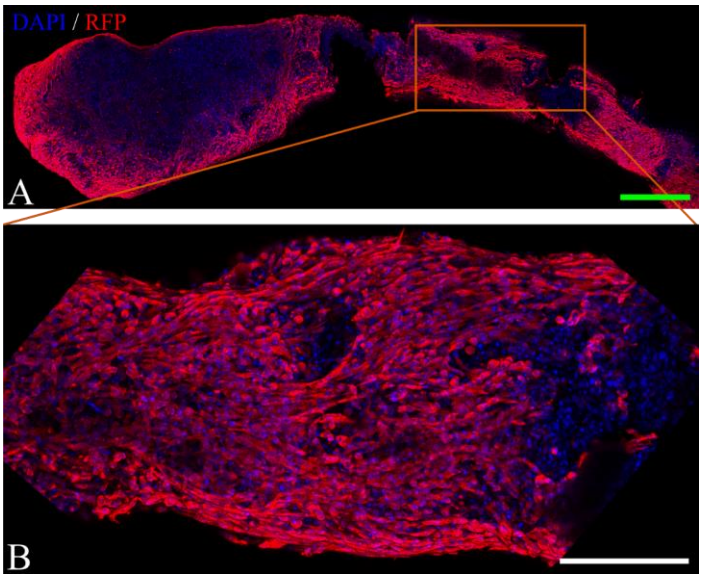

Figure 33. EDOF composites of confocal images showing part of the SMC-spheroid constructs at D10. In **red** represents data comprised of the RFP signal produced by SMC and present in its cytoplasm, as well as α-SMA, part of its cytoskeleton, immunostained with mGFP. Their nuclei are visualized with DAPI in **blue**. As can be observed in (**B**) almost all observed cells, the location of which extended to a depth of about 65 μm, showed clear alignment along the constructs' major axis and no indication of the initial spheroid constituents remained. Scalebars green: 500 μm, white: 200 μm.

Apart from the construct's mechanical stability, the possibility to perform a relatively progressive bath dilution in both time and volume can be partially ascribed to its reduced concentration of 0.75% (w/v) XG, necessitated due to inability to eliminate air bubbles at from the 1.5% regularly used.
Even though the construct laid upon the dish's surface from at least day 4 onwards, no indication cell-surface attachment could be observed, which was in opposition to constructs composed of C2C12-cells, CMs and ECCs.
In both the transmission, fluorescent and confocal data obtained, no (partially) intact initial spheroids could be distinguished.

5.5 Printing bioinks laden with a mixture of non-proliferating cardiac cell types

With the observed formation of stable tissue constructs from non-proliferating cell types (CMs) and from cellular self-reorganisation from spheroids an experiment was hypothesised with the goals of 1) show the possibility of stable construct formation from a bioink laden with multiple different non-proliferating cell types, 2) enhance the visualisation of individual cell positions during this process to track self-reorganisation, and 3) analyse its functionality during prolonged culture.

This was done by using a bioink containing a 40:60 mixture of hPSC-derived CMs and ECCs which could be individually located by utilising their distinct fluorescently labels. [99]

In the DRAGGN-line CMs red fluorescent mRubyII-α-actinin fusion protein present in sarcomeres allowed detailed visualisation of their presence and orientation in red, while GFP present in the cardiac marker NKX2.5-locus labels its cytoplasm green.

The red florescent mCherry acts as a ECC reporter when bound to the COUP-TFII locus.

The mCherry and mRubyII response signals overlap, however, adjusting the detection settings to be optimal for mCherry, compensating for its weaker signal, combined their position within the tissues, made them distinguishable from simultaneous capture (**Fig. 34.B-D**).

Similar to the previous experiments, diffusion packing facilitated the accumulation of the vast majority of deposited cell into their corresponding constructs during the first hours after printing. Between D0 and D2 this process, combined with cell migration, allowed the formation sections containing suboptimal cells numbers to keep the structure connected, resulting in some fragmentation. Although very narrow isthmuses were still present or formed after the first 2-3 days and the bath dilutions exposed them to progressively increasing forces, from this timepoint forward the remaining construct's geometry remained quite stable with only slight bending (**Fig. 34.A**). If a line break occurred, both end sections slightly decreased in length while their average cross-sectional diameter slightly increased, suggesting additional cell motility and repositioning (**Fig. 34.A**).

As expected from a bioink containing a cell suspension homogeneously mixed, the post-deposition cell distribution was random at D0 and D1 (**Fig. 34.B**). Interestingly, from D3 and onwards, all sections analysed using fluorescent imaging showed a clear spontaneous self-reorganisation into dense constructs with ECCs more prevalent at their periphery and CMs making up most of the cell population within their interior, mimicking their relative positions *in vivo*. This pattern can be seen in **Fig. 34.B**, depicting the same line section with random (D0) and organised (D13) distribution. Confocal Z-stack data with orthogonal slices confirm that that a 20-80 μm thick layer of mainly ECCs, where few to no CMs reside, covers the construct, while in the interior their prevalence ratio is flipped (**Fig. 34.C**). Sarcomeres were abundant and prominent in over the whole tissue however their orientation was mostly non-aligned (**Fig. 34.D**).This can be possibly attributed to a lack of external points of attachment providing mechanical resistance often crucial for alignment of cells and their cytoskeletons.

Beside the capacity for cellular self-reorganisation additional tissue function was further observed with the development of filopodia when sufficient bath dilution allowed a descending construct to contact the container's surface between D11 and D13 (**Fig. 34.E**). However, because this partial disintegration threated the cellular organisation, which was of great interest, the culture was terminated after electrical stimulation experiments, and fixated to preserve tissues uncorrupted,

At D7 some tissues contracted when an electrical stimulus was applied (20 V/cm for 10 ms). The first spontaneously contracting tissues were observed 1 day later. After at least 15 days of culture all constructs still intact responded when electrically stimulation. Graphs projecting the relative displacement between tissue terminals of a line with length 3.7×10^3 μm over time, examples of which are given for stimulation frequencies 2.5 and 3.5 Hz, show the contraction frequencies correspond almost perfectly with the stimulation frequencies tested up to 4.0 Hz (**Fig. 34.F**).

When fully freed from the suspension gel (>D11) the tissues could be moved around and picked up without inflicting perceptible damage using tools like tweezers, spatula, and micropipette aspiration (**Fig. 34.G**).

These functionalities represented the formation of stable but active self-reorganising 3D printed tissues which combined the functionality of both incorporated cell species up to >2 weeks of culture.

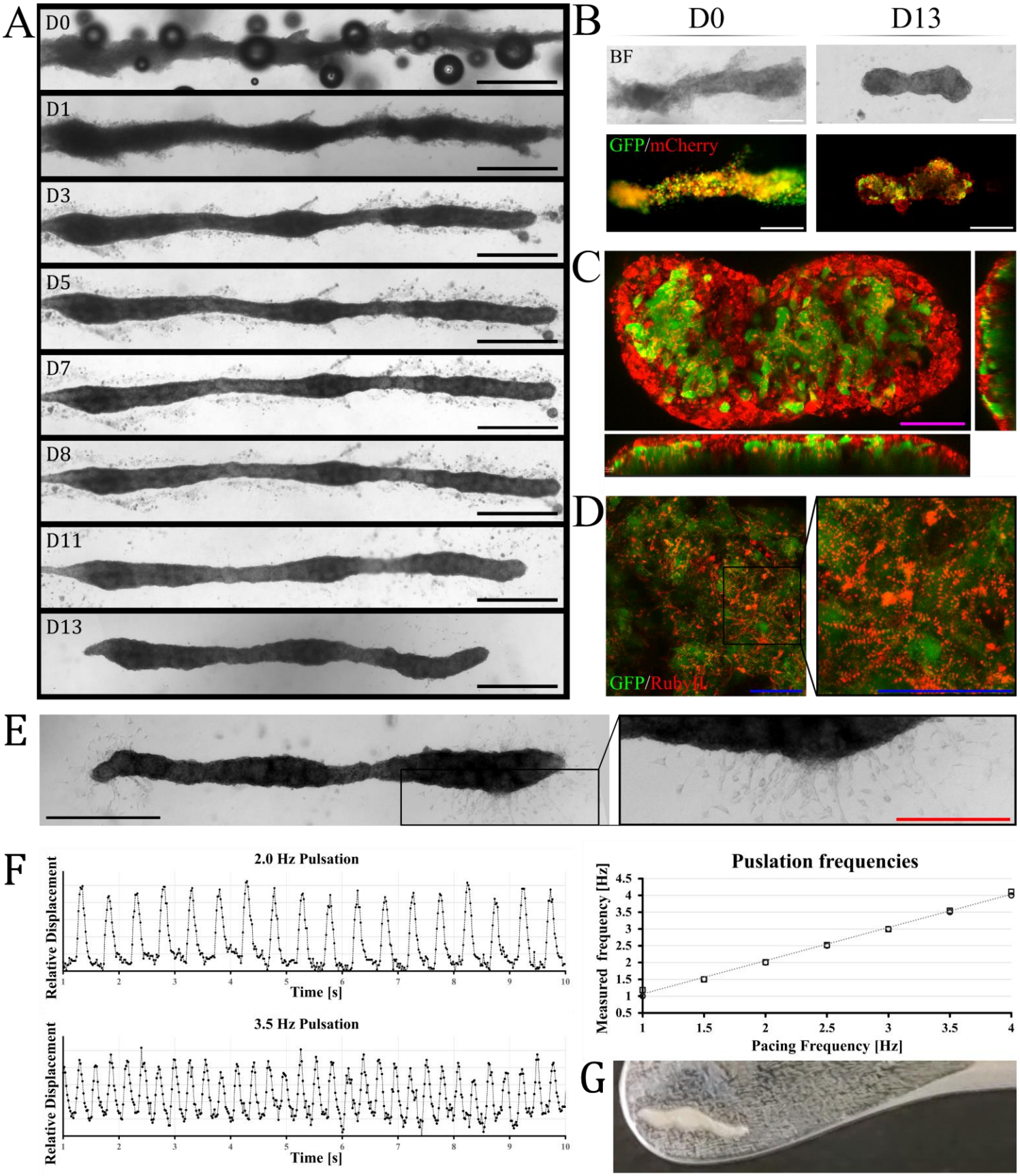

Figure 34. Printing a combination bioink laden with both CMs (φ_p 0.04) and ECCs (φ_p 0.08). **A**) Timelapse of a section E100% line. Between D0 and D1 the cells which end up part of the construct were compacted. The leftover clusters of cells would be washed away after sufficient bath dilution on D8. **B**) Brightfield and fluorescent images of the section at D0 and D13. At D0 distribution of ECCs (mCherry) and CMs (GFP) was random, while a spontaneous self-reorganisation separated the cell species distinctly with ECCs on the periphery and CMs at the interior. **C**) Analysing confocal Z-stack data of constructs, fixated at D11, allowing a better visualization of the cell species distribution. **D**) Zoom-in on the DRRAGN-line CMs (GFP) where mRubyII, staining ACTN2, visualize the presence and orientation of sarcomeres. **E**) Brightfield images of a tissue at D13 developing filopodia upon contact with the container surface after D12 days in suspension. **F**) Graphs depicting relative distance between a construct's most distance tips over time when exposed to an electrical potential of 20 V/cm for 10 ms at 1.0-4.0 Hz. The graph on the right notes the input Hz and corresponding pulsation frequencies. **G**) Mechanical stability allowed easy handling with a spatula, among other tools, without inflicting noticeable damage. Scalebars; black: 1000 μm, white: 250 μm, pink: 100 μm, blue 50 μm, red: 500 μm.

5.6 Printing bioinks laden with a PLA-μparticles & SMC-spheroids mixture

After observing the quick formation of very stable SMC structures and the emerging of spontaneous cellular self-reorganisation of CM/ECC constructs, the platform was thought suited for testing the incorporation of microparticles in 3D printed tissues. Which, if successful, would not only extent the remodelling capabilities shown, but also be used as a great tool in future projects to facilitate, among other things; a) the formation of more stable structures, b) the internal release of compounds such as medicine, growth factors or nutrients, or c) when dissolved, the formation of hollow, permeable, structures, while using fewer cells to reach the desired φ_p.

For this the previously observed stability of constructs comprising SMCs-spheroids was utilized by combining them with PLA-μparticles ($Ø_{avr}$ 30μm) in a bioink suspension. The particles' surface was collagen-coated leading to an enhanced affinity for cell binding, facilitating their incorporation, cell migration and final tissue stability.

The combined particle volume fractions of SMCs spheroids at (φ_p^{sph} 0.017) and Col-PLA-μparticles ($\varphi_p^{\mu p}$ 0.017) was with φ_p^{tot} 0.034 lower than intended due to insufficient spheroid size increases during culture. Because the extrusion rate was not increased to avoid possible backflow it was inevitable the shape's features were to become very narrow after diffusion packing.

Here they were prone to break and separate into individual constructs about the most cell dense regions between D0 and D1 (**Fig. 35.A**). Interestingly all but a few μparticels accumulated into these structures, compacting to a var greater degree than seen with inert particles printed similarly. This suggests SMC were able to connect and bind to μparticles and each other such that the whole aggregation was able to be pull and reorganise, forming cleared gaps between section >1100 μm in the first 24h (**Fig. 35.A-I** & **II**) in the process. These accumulated constructs were cultured up to 7 days during which they remained stable in overall size and shape, with only slight increase in spheroidicity, suggesting limited proliferations rates when compared to the constructs only comprising SMC-spheroid (**§5.4**).

Fluorescent imaging showed self-reorganisation from a randomly distributed mix of spheroids and μparticles on day 0 to a dense tissue which harbours all particles in reach of the cells which collapsed into said tissue (**Fig. 35.B**).

Although restricted by the limited penetration depth of the RFP response signal (±60 μm), from the lack of this signal during confocal imaging, the concentration of μparticles seemed higher in the constructs interior while, probably due to elevated SMC proliferation at its periphery as a result of their closer proximity to nutrients (**Fig. 35.B-V**).

The tissues were stable enough to be handled with tweezers, micropipette, and spatula, without inflicting noticeable damage.

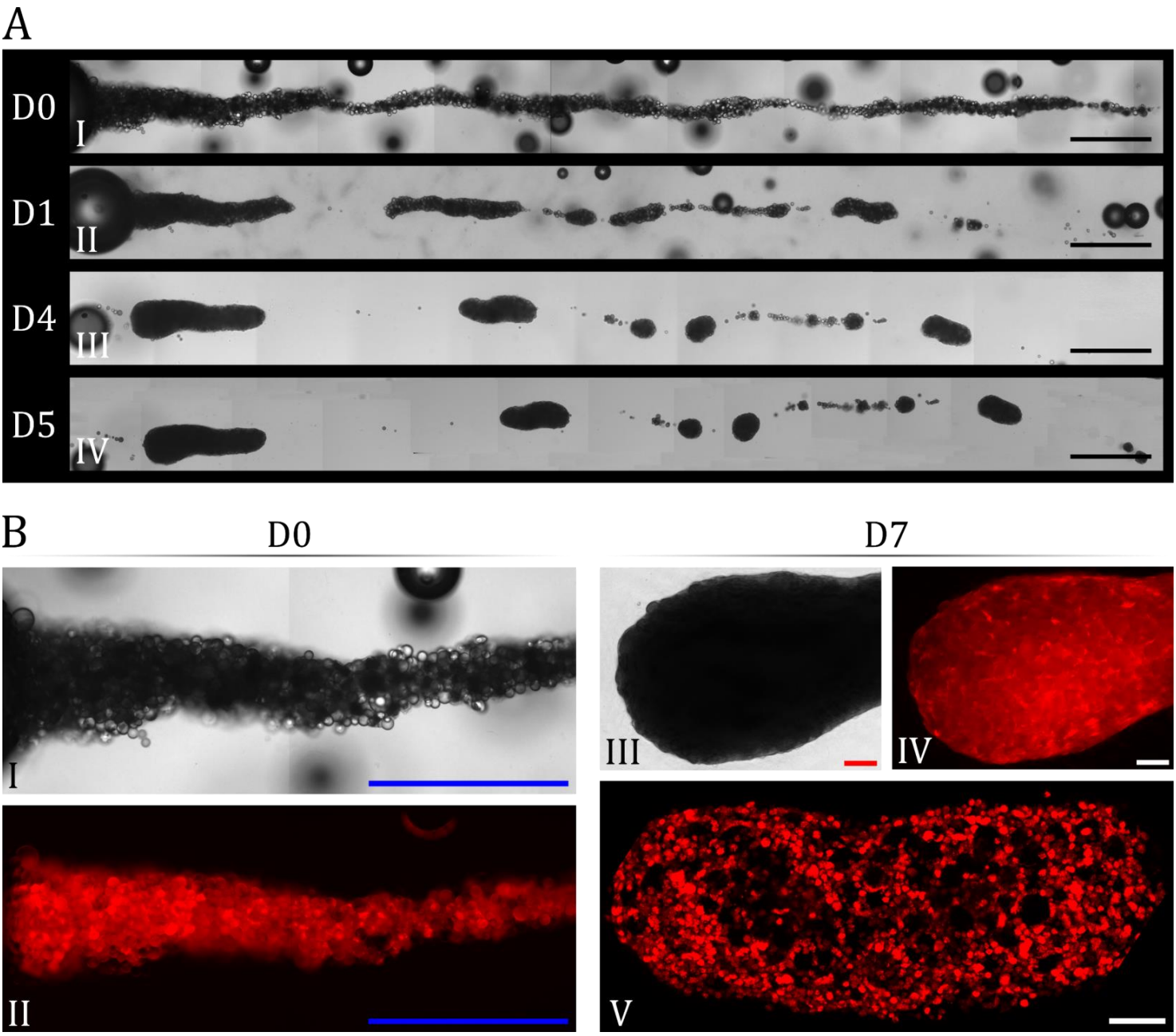

Figure 35. Printing of RFP-SMC spheroids (φ_p: 0.017) with Col-PLA-μparticles (φ_p: 0.017). **A**) As a result of spheroids developing to be smaller than expected the φ_p^{sph}, and thus φ_p^{tot}, were quite low, the post-compaction thicknesses didn't allow for the formation of a single stable structure. Compaction accumulated all but a small number of cells and Col-PLA-μparticles to the areas of highest density between D0 and D1 and during the subsequent days, reorganisation formed small but stable constructs. Scalebars black: 1000 μm. **B.I-II**) The more translucent Col-PLA-μparticles can be seen randomly distributed throughout the deposition area at D0. **B.III-V)** After 7 days of culture the PLA-μparticles were fully integrated into the constructs and surrounded by SMCs, of which the initial spheroids could not be discerned. **B-V**) EDOF confocal image shows the positions of many μparticles (dark spherical contours) throughout the construct interior, some next to other μparticels while others were separated but all fully encapsulated by SMCs. Scalebars; black & blue: 1000 μm, white & red: 100 μm.

5.7 Printing bioinks laden with a PLA-particles & SMCs mixture

Exploring the platform capabilities even further and to show particle types with different geometries, mechanical properties and densities can be printed simultaneously successfully an experiment was performed in which a bioink comprising of SMCs and Col-PLA-μparticles was printed. With μparticles being significantly denser, possess different mechanical properties and have more than double the volume compared to SMCs. Lines deposited with bioink φ_p^{SMC} 0.075 and $\varphi_p^{\mu p}$ 0.013 were noticeably wider and thicker compared to SMC-spheroid/μparticles printed, which can be attributed due to the lower φ_p^{sph}.

Similar to what was observed when printing SMC-spheroids/μparticles but more clearly seen here is that the extent of the gathering and accumulation of cells and particles was only limited by the geometry of regions where all particles formed a singular connected 'structure' after the initial diffusion packing. This extensive compaction was highly disruptive to shape fidelity as can be seen in the representative result **Fig 36.A**. Here the densest regions with poor to no interconnectivity formed 2 mayor, highly spherical tissues with only few particles not included. In these regions, a similar process compared to printing SMC-sph/μparticles occurred, whereby a homogeneously mix of SMCs and μp's can be seen to compact into a dense tissue including nearly all μparticles in its direct physical grasp (**Fig. 36.B-I-IV**). After day 3 the only development was a slight increase in spheroidicity, however overall size and shape remained constant indicating limited proliferations rates. The example EDOF confocal image presents an internal organisation **Fig. 36.B-IV**. Like mentioned prior the structures is not hollow, but the centre (lowest) portion is excluded from the EDOF the enable internal structures to be observed. The μparticles bundled densely in the centre, fully surrounded by locally aligned SMCs.

The tissues were also stable enough to be manipulated with tweezers and aspiration harmlessly.

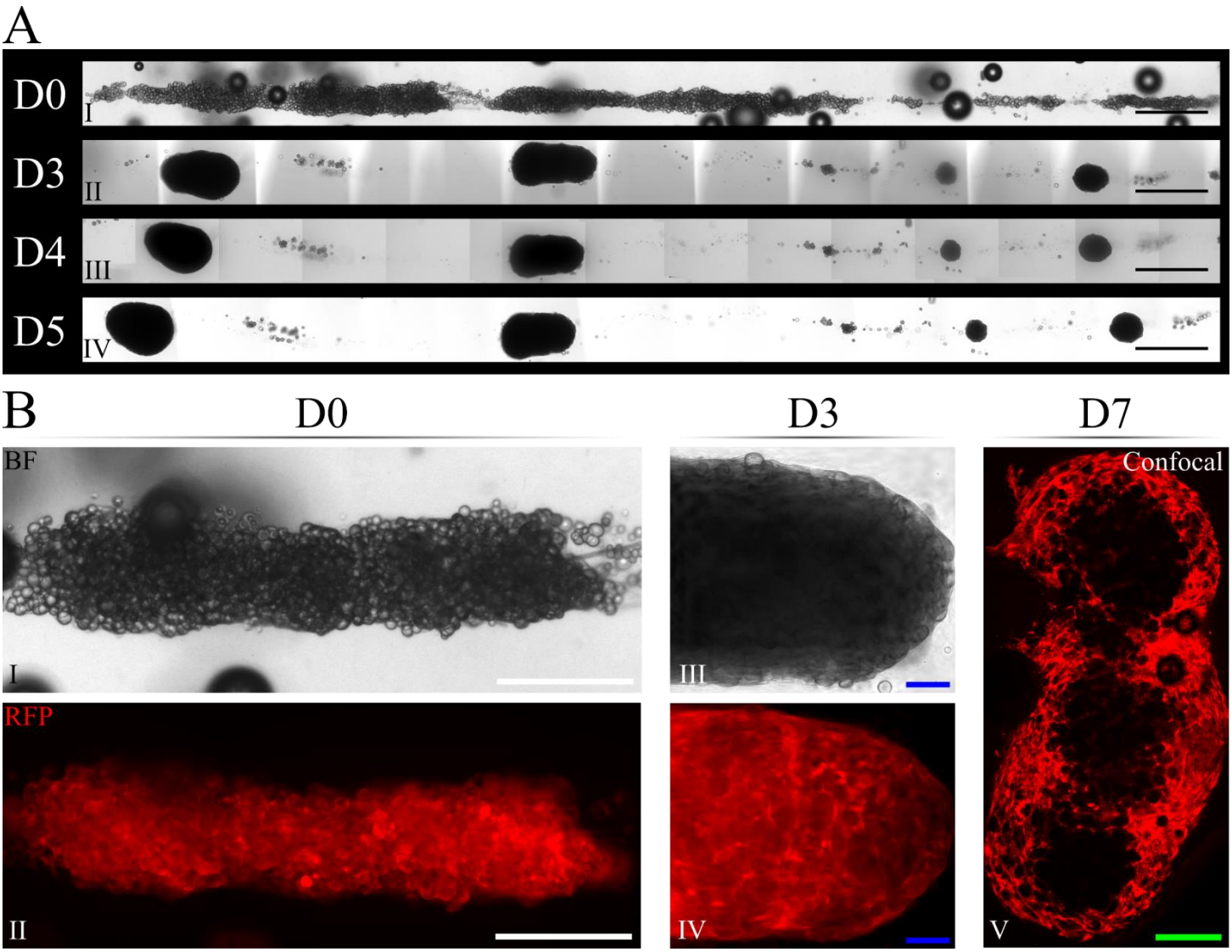

Figure 36. Printing of bioink laden with a mixture of RFP-SMCs (φ_p^{SMC} 0.074) and Col-PLA-μparticles ($\varphi_p^{\mu p}$ 0.013). **A**) E100% G23 line at moments after printing at D0 up to D5. Similar to SMC-spheroid/μparticles bioink, connected high particle density regions compacted in single dense spherical tissues which remained stable during the following 7 days of culture. **B.I-IV**) Zoomed in region of (**A**) shown to develop in a dens construct incorporating the Col-PLA-μparticles shown in more detail in EDOF confocal image (**B.V**). Scalebars; black: 1000 μm, white: 500 μm, blue: 100 μm and green: 250 μm.

Chapter 6. Discussion

6.1 Observed limitations of platform components

Characteristics which in some way reduce the employability and practicality of the platform were observed during the optimization phase and subsequent experiments. The most notable inherent limitations regard the ink components (**§6.1.1**), needle architecture (**§6.1.2**), XG-based embedding baths (**§6.1.3**), printer design and capabilities (**§6.1.4**), deposition and compaction (**§6.1.5**), Duration of culture and retrieve stage (**§6.1.6**), and observations (**§6.1.7**).
Some possible recommendations to these limitations will be suggested and discussed in **chapter 8 Future Outlook**.

6.1.1 Ink components

Particles properties can affect the extrusion pattern, the most important of these include size (**§6.1.1.2**) and density (**§6.1.1.3**) will be discussed.
Also of note are the properties of morphology, plasticity, concentration (φ_p), surface chemistry, and intra-particle interactions, however these were not analysed in sufficient detail and will thus not be discussed here.

6.1.1.1 Cell types

The current platform has drawbacks and limitations regarding the properties of the printed cell types. The structure comprised of those which can't compact into constructs of sufficient mechanical stability structures (fast enough), might be compromised by the necessary bath replacements. Constructs which incorporate proliferating cells have the benefit of becoming more stable over time by increasing their cross-sectional area and the potential to bridge or mend weak sections. However, a drawback of high cell metabolism is the large consumption are of nutrients including oxygen and the creating of waste products, which will both be discussed in **§6.1.3.2** in greater detail.
These factors cause a balance to be struck between the ability to endure dynamic processes; (1) Extrusion printing, (2) thriving in the subsequent high cell density environment, (3) form stable structures allowing enhanced bath refreshments in both volume and frequency one side, and the necessity to do so due to; (1) providing nutrients, (2) waste removal, and (3) construct retrieval, on the other.
Another possible limitation that could be imposed on the cell types is derived from the high number necessary for printing in the current setup. To be save, the combination of setting up the printer together with the dead space in both the syringe and needle totals ±150 μL for each printing session unavailable for printing itself. As an example, assuming an $\emptyset_{avr}$ for ECCs of 15.2 μm and a φ_p 0.1 bioink this results in 8.2×10^6 of unusable cells. Depending on the research facility's capabilities and resources, these minimal number of cells can impose restrains on the cell types which could be provided during certain stages of platform development and optimization, opting for those relatively cheap to obtain, expand and maintain. And, by extension, the shapes, sizes, and types of tissues constructs which can be potentially produced in meaningful quantities.
For these reasons the cellular constructs discussed in the results implemented cell types already in use by AST out of which stable construct could emerge (ECCs and CMs) and are fast-proliferating (iPSCs, MSCs and C2C12 cells).

6.1.1.2 Particle size

As previously discussed, (**§2.1**) regarding particle suspensions, a combination between cell sizes, φ_p, Re, particle-particle and particle-wall interactions, and internal geometry affect flow behaviour through an orifice impose size restrictions. [59] The SMC-spheroids and alginate hydrogel μbeads approach a high *neck-to-particle* diameter ratio D/d (**Fig. 17**) and clogging events were observed. However, some also exceeded their respective carrier fluid density and no experiment addressing the impact of particle size on the transition in extrusion regime was separately performed, and thus related statements could not be formulated based on the results currently obtained.

6.1.1.3 Particle density

The densities of bioink components, especially particles, are restricted in 3 main ways which are derived from the use of a single carrier fluid in which the components can move quite freely.
An upper boundary is imposed by the utilization of OptiPrep as a density modifier, which can only facilitate in the creation of stable homogeneous suspensions up to its own density (1.320 g/mL), when used as the only liquid component. Significantly heavier components will sink and cause irregular extrusion, clogging, or deposit on the syringe interior ledge.
Using the same logic, a lower bound results from the use as medium as the carrier fluid, which has a density close to that of water. Significantly lighter particles will float and cannot be extruded due to the dead space in the syringe and needle.
A third restriction on density is a necessity to minimize the relative differences between different bioink components, enabling the carrier fluid to temporarily suspend them homogeneously simultaneously.

Slight discrepancies between component densities will result in irregularities during extrusion, which in turn will cause a limit on the duration before the syringe has to be uninstalled for homogenisation.

Furthermore, forces generated due to density differences between a structure floating upon or suspended within shear thinning fluids could be greater than its yield stress, resulting in displacement of said structure. [111] In most instances this is not desirable and thus yield stress, cumulative particle densities, or construct shape should be tailored and tuned appropriately.

The impact of other particles component properties, besides sizes, densities, and φ_p, will not be discussed in detail, for they were not in the scope of this research and therefore not analysed.

6.1.2 Needle architecture

Bend needle geometry has been shown to exhibit good printing results in limited movement and deposition orientations. Only extruding while moving in the direction of the bend, relative to the embedding bath, creates the liquefied XG column which can be filled in a controllable and consistent manner needed for cell-dense and interconnected tissue formations.
The relatively large submerged vertical component, however, influences the surrounding baths which have to be kept in mind during design, especially requiring the need to moving near delicate printed structures.
Some things not achieved during this research, like sheet formation from adjacent lines or sideways movement, although local particle accumulations were observed.
It may thus be possible when altering bioink and/or embedding bath compositions, especially towards higher φ_p's, but also towards more successfully retain ink locally or decrease the distance at which traveling needles disrupt their surroundings.
In the current setup both the syringe and needle possess dead volume, harbouring ± 150 μL requiring additional particles/cells to reach the intended printed cell volume and thus raising culture time and costs. This relatively large use of cells (volume) has been one of the main restrictions on the maximal bioink φ_p^{cell} during this research.
The internal volume also provides surfaces upon which slowly sinking cells can deposit, which have the additional potential to cause intermittent flow by clogging, leading cell density extrusion to become less homogeneous.

6.1.3 XG-based embedding bath

6.1.3.1 XG concentration

The standard concentration of 1.5% (w/v) XG, used in the formation of most embedding baths during this research, was mostly chosen as a compromise between the disadvantages and advantages as noted in **§4.1**. This was based on the results of printing with a straight needle in DPBS-based bath. However, both the tools and the bath composition were changed continuously throughout these experiments. It is therefore probable that a XG-concentration more tailored to the specific conditions and objectives of the individual experiments could have been used for more optimal results, like done with the 0.75% (w/v) concentration used when printing SMC-spheroids. However, current restrictions on time, resources and a lack of cell-medium-based hydrogel rheological data, a constant XG-concentration proceeded to be used.

6.1.3.2 Physical characteristics

Printing designs and their fidelity are limited by the embedding bath rheological properties.
High viscosity at low shear causes a dragging force to be induced by both the traveling needle, restricting printing path geometry if disturbances to previous depositions are to be kept minimal, as well as during bath dilution, restricting aspiration speed, magnitude, and proximity to delicate printed constructs.
During this research multiple different culture media were used as the hydrogel's liquid component, some of which resulted in gels with properties making it difficult or impossible to remove air bubbles, introduced during mixing, with the tools available at the time. This heterogeneous mixture harbouring cavities may interfere with print fidelity and this property should therefore be considered and avoided in embedding bath design.

6.1.3.3 Nutrients availability

The use of high cell numbers is limited by the diffusion rates of nutrients, gasses, and waste products through the medium, XG gel and tissue itself. This limits construct size and density without active perfusion or altered culture conditions like elevated oxygen levels and nutrient concentrations. [26] Because the encapsulating hydrogel cannot be readily removed interdependent restrictions are imposed on multiple parameters such as initial cell concentration, cell types, deposition rate and depth, construct stability, bath composition, refresh rate, and nutrient concentration to avoid the formation of deficiencies or waste build-up detrimental to cell viability. Additionally sufficient diffusion rates are also necessary for the creating of a bioactive support, crucial in remodelling and morphogenesis after bioprinting. [54]

Baths containing cell cultures have a characteristic pinkish hue of the pH-indicator phenol red when undisturbed. However, it has been observed that during bath distortion, e.g. stirring with pipette tip, the upwelling embedding bath is noticeably more yellow, most noticeable in cultures containing fast proliferating cells (**Fig. 37**). Originating close to the constructs, these areas move mostly as separate stable blobs through the pinkish, more liquid medium, not mixing noticeably. It is hypothesised this discolouration is the result of the alteration of phenol red towards its lower pH protonated configuration, which might be an indication of the local build-up of acids, especially carbonic acid

(H_2CO_3, from CO_2 reacting with H_2O), generated during cell metabolism.
Air bubbles which were present in the bath upon printing disappeared during a day of culture ±10 mm radially from any high cell density spot, while more distant bubbles did not reduce in size over at least a week of culture. This might indicate a severe reduction of diffusion speeds through these XG-hydrogels compared to regular medium.
If this is the case, this introduces additional restrictions compared to culture in normal cell medium including on local and overall cell populations, construct thickness, minimal bath refreshment speed and minimal proximity of constructs. A restriction in maximal distance between surface and printing height should also be considered.

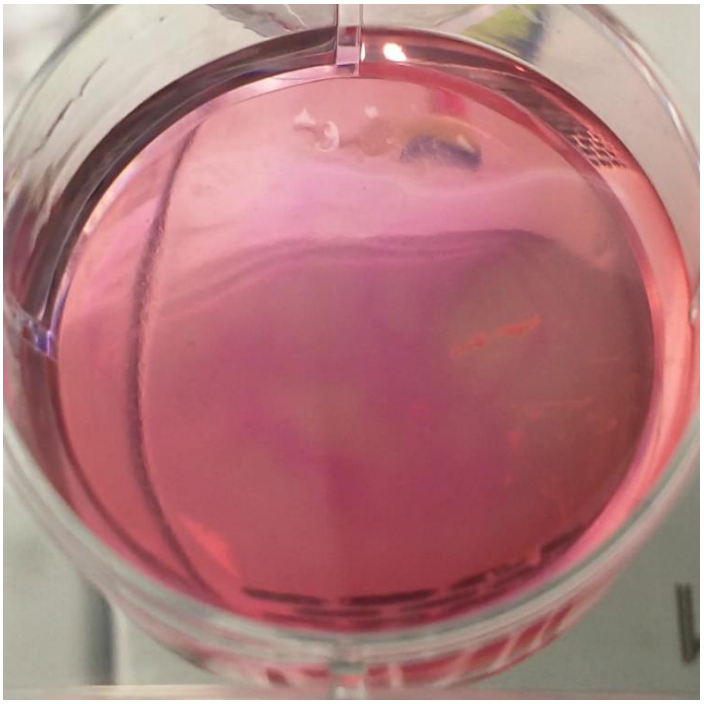

Figure 37. Visible upwelling and unmixed yellow bath discolouration after disrupting a 7-day culture of CM constructs in CM-MM.

A clear example showcasing a difference in proliferation rate is the SMCs printed in parallel lines presented in **Fig. 25**. During the needle's repositioning some spheroids ended very near to, or on top of, the bath's surface. Over the 2-day culture these cells proliferated very fast, clearly dominating the culture in numbers compared groups of spheroids deposited at least 5 mm below the bath's surface. The main difference between these populations is their vertical location, thus their proximity to fresh medium is similar. The proximity to oxygen is, however, quite different and it is therefore hypothesised inside the bath a critical oxygen gradient develops, forming a major barrier for cell metabolism, especially when competing with cells more proximal to the source.

6.1.4 Printer design and capabilities

The 3D extrusion printer used has characteristics and inherent limitations which must be taken into consideration when designing for experiments and during operation.

6.1.4.1 Printer design

As mentioned in **§3.6** printing occurs in a single chamber, closed by a single door. When the door is open during handling, only the descending flow from the HEPA-filter keeps outside non-sterile air from intruding, for it was currently not possible to position the printer inside a laminar flow hood. This increases the risk for contaminations greatly compared to working in normal cell culture conditions.

6.1.4.2 Extrusion resolution

The control on extrusion volumes, its resolution, depends on the device and equipment used. Only the vertical plunger can be controlled to establish extrusion, so a narrower volume container (syringe) enables smaller discrete volume to be extruded. The NewCreatorK software, native to the BioInvivo 3D printer, generates g-codes with an extrusion-value to 5 decimal places. Assuming this is most accurate E-value command the printer can interpret and reliably follow, without significant play in rest of the system, this corresponds to a minimum discrete volume of ± 2 nL, when calculating for the 1 mL syringe used in this research. Mechanical dispensing systems, like employed here, are regarded to have great spatial control and are more accurate extruding high-viscosity inks compared to pneumatic systems. [12]

6.1.4.3 Movement and deposition resolution

Derived from output from the NewCreatorK software, coordinates describing nodes composing the printing path are given in three decimals for all three axes. Again, assuming this is the most accurate positional command the printer can interpret and reliably follow, this corresponds to a maximum movement resolution of 1 μm.
Due to the momentum of both the device and embedding bath, slight inaccuracies can be expected during quick vector changes, which can possibly cause discrepancies in printing fidelity and reduce deposition resolution.

6.1.4.1 Printer features

Immediately after the initiation of every g-code, the syringe-holder moves to a relatively low position to self-calibrate its z-position. This imposes a maximum minimal distance between the build platform and syringe holder, restricting the length of the needle/syringe combination below the holder. Fortunately, when using the only manually adjustable holder, the needles used just clears the surface by ±2 mm during this movement, while the non-adjustable temperature-controlled holder could not. Which thus could therefore not be used.

6.1.4.2 Unpredictable printer performances

One of the unintended features the printer exhibited was an unpredictable interpretation of the g-code. Sometimes the commands for maximum acceleration (*M201*) and acceleration (*M205*) were randomly omitted or the value from a

previous run was adopted. In addition to this, the values for both commands can only be set once during the run of a single g-code and applies for both acceleration and deacceleration which, especially in future complex geometries, may increases printing times drastically.
Although this was not regular behaviour and the initial experiments utilizing of these commands showed promising results, the unpredictability combined with the potential waste of cells and materials to an erroneous print led to the choice to leave their implementation to follow-up optimizations experiments and to omit them for now.
Of note is also unusual sounds produced by the engines driving the leadscrews on all three axes, especially at very low revolutions, which didn't evoke confidence this system was designed to execute these commands as such.

6.1.4.3 Practical missing features

The printer has no ability to rotate or tilt the embedding bath or syringe (holder), significantly limiting the freedom in possible print geometries. This is especially true with the use of 90° bend needles, which have the additional restriction of being only shown to work successfully along a single horizontal axis for now.
No commonly used g-code command has been found to pause any or all printer movements. Because this feature could be very desirable during the crucial and delicate moments of diffusion packing, it was accomplished by cutting of all electrical power to the system. This action could however be potentially detrimental to the equipment when done frequently, and repeated system restarts extended the overall printing time greatly.
No real-time macroscopic or microscopic view of the printing process or bioink status (clogging, homogeneity) can be obtained in the current device. Something which could especially be of great aid during problem solving and optimisation.
The temperature-controlled syringe holder is not adjustable in height, which imposes a limit on needle lengths which excludes the bend needles in this research.

6.1.5 Deposition and Compaction

When printing a single line with a single pass, some generalisations about the minimum and maximum extrusion rates can be formulated, outside of which printing results are expected to be highly irregular.
Printing imperfections have a relatively increasing detrimental effect on print fidelity with decreasing particle infill value, resulting in areas harbouring suboptimal cells concentrations. Too few connections to withstand intracellular reorganisation forces and the quite coarse bath removal, lead to necking and breaking. This suggest that for each combination of printing parameters, there exists minimal particle infill value, below which regular breaking of the construct can be expected.
As derived from the **§2.3** about infill values, maximum extrusion rates do also exist. This value is meanly determined by the needle's $Ø_{OD}$ and its travel velocity. Ink replaces/fills the liquefied column of XG, produced by the traveling needle and left in its wake. Non-liquified bath will constrain the ink further, meaning that when the extruded volume is significantly higher (>E150-E200%) than which is liquefied, the path of least resistance guides the excess ink between the boundary of bath and needle, away from the intended printing area.
A direct result of restrictions on maximum particle infill values, which itself is a result of volume fraction and extrusion rate limitations, is a maximum particle volume concentration after compaction and thus a maximum initial constructs thickness.
Restricting the speed at which extrusion ramps up is also necessary, especially if not enough XG has been liquefied by needle movement. If ink travels too quickly, due to a sudden increase in pressure or a blockage is breached for example, it might yield the bath, be propelled, and be deposited away from the printing area.
The aim of printing a thicker line by way of repeated passes resulted in an heterogenous deposition where previously deposited ink is dragged by the needle, accumulating mostly on the exiting end and while leaving an insufficient number of particles to accumulate in a dense fibre (data not presented).

6.1.6 Duration of culture- and retrieve stages

From the previous paragraphs maximum and minimum culture times before successful construct retrieval can be considered.

A minimum culture time before retrieval is a result of a maximum bath removal speed, which itself is dependent on XG dilution speed, construct geometry, position, and development, but mainly on the speed at which its able to become sufficiently mechanically stabile. There is thus always a minimum time before the construct can be freed (intact), except when its stability and geometry allow an alternative method, e.g. careful extraction through a pipette tip or by tweezers of spatula.

In addition to this, certain processes also impose a maximum limit on construct retrieval time.

Firstly; the possible decreased diffusion rate within XG hydrogel networks hinder the availability of nutrients and cause the build-up of waste products and cell debris, which can both have a negative effect on cell viability, function, and construct stability.

Secondly; the proliferation of cells increases the construct size and thus construct radius. Because of inherent diffusion limitations, which steadily decreases the nutrients available to the (interior) cells, which is also detrimental.

Thirdly; the ability and result of spontaneous construct formation by cellular organisation is one of the key areas of interest for this platform. Gradual bath removal liberates suspended constructs which will be decreasingly supported and descend to the container's surface, the speed of which depends on bath removal and tissue density. Upon contact cells can easily migrate upon it, the consequences of which are dependent mainly on the cell-surface interactions but may lead to the disintegration of the construct's structure. This does not only form a danger to the constructs intended capabilities and reduce its significance for later analysis, the rapid spreading of surface bound cells also depletes available nutrients quickly.

6.1.7 Observations

In addition to the incapability of observing the printing process in real-time using the current printer, something which was partially resolved by employing a custom-made imaging setup, other components reduced the observational ability or quality.

Inverted (transmission) microscopes have a limited depth of field (the height of the layer in focus at any one time) and depth of focus (the total vertical range over which a focus can be retained). As mentioned before, printing the construct as close to the bottom of the dish as possible, to allow sufficient microscopic observations, can cause the cells or constructs to migrate to its surface and spread rapidly, with adverse consequences. Using embedding bath containers of relatively thick plastic combined with the limited DOF's of the microscope, sometimes diminished sufficient observational data for some sections positioned high out of focus.

Because the constructs do not contain lumen, the densest sections will block almost all light during bright-field, fluorescent and confocal microscopy, allowing only the outer edges to be observed in any detail. It is therefore difficult to observe its internal structure in a non-destructive manner like sectioning.

6.2 Initial experiments

The first initial experiments were performed using a stainless steel G22 straight needle. These results showed very local bioink retention, diffusion packing, albeit seemingly to a lesser extent, and the ability for adjacent lines to fuse and form stable tissue constructs out of CMs. Although the process was not optimized, and large shapes broke quickly, some tissues were kept in culture up to 18 days, during which they became increasingly spherical and were spontaneously contracting as a single structure.
However, these print results could not be replicated after depleting the initial XG-powder stock and instead sheet formation, like mentioned previously, became inherent.
This might be a consequence of the XG not being produced and packed in a sterile manner by the manufacture (Sigma-Aldrich). It is therefore very likely the powder and its derived hydrogel contained organism which can cause infections. It was assumed the chemical composition of XG, which influences rheological properties as mentioned in **§2.1**, was comparable between batches. It is therefore hypothesised a very fine network made from fungal hyphae, partially suppressed by the limited antifungal (fungistatic) activity of P/S and therefore not observed microscopically, may formed a secondary matrix throughout the hydrogel and may act as a net, capturing the bioink. [112]

The distinctive ink retention properties characteristic of the Newtonian embedding bath made from a mixture of XG and SA, shown in **Fig. 16A-C**, are similar to those found in the initial experiments. When improperly mixed, instead of forming a singular hydrogel network by intermolecular hydrogen bonds, ‘’pockets’’ of one hydrogel can be suspended in the other, depending on mixing and their ratio. This infection might have formed a secondary network, suspending XG, coincidentally causing a combination of properties which allowed for the compaction mechanism to transpire and proximal cells to reorganize without any obvious adverse effects.

If true, the presence of micro-organisms possibly alters both the embedding bath rheology and printed cell physiology, thus decreasing the ability to compare some experimental results and the conclusion base thereupon. However, it is shows highly desirable properties which well-designed secondary networks might add to the current platform.

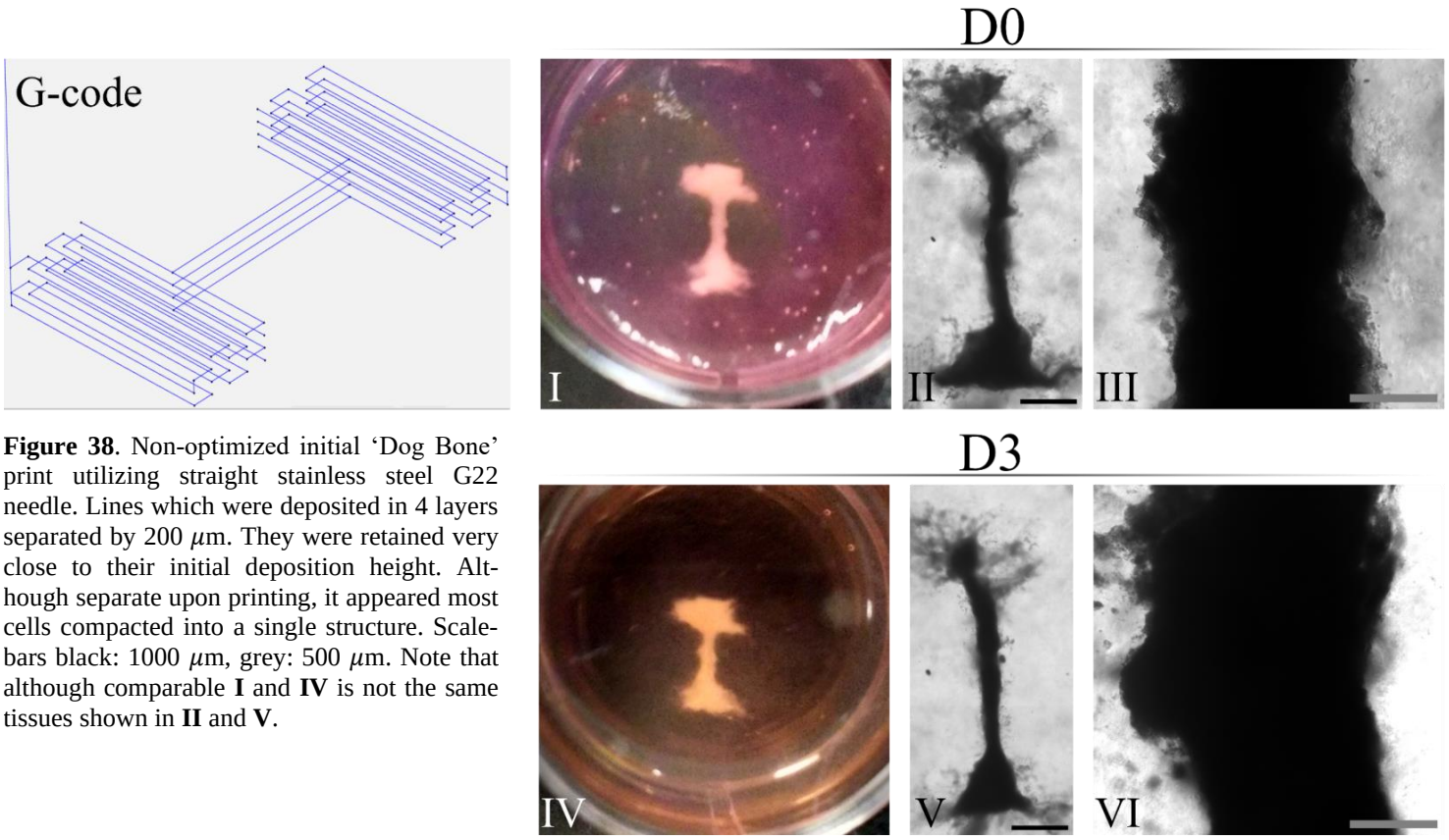

Figure 38. Non-optimized initial ‘Dog Bone’ print utilizing straight stainless steel G22 needle. Lines which were deposited in 4 layers separated by 200 μm. They were retained very close to their initial deposition height. Although separate upon printing, it appeared most cells compacted into a single structure. Scale-bars black: 1000 μm, grey: 500 μm. Note that although comparable **I** and **IV** is not the same tissues shown in **II** and **V**.

6.3 Discrepancies in experimental results

The printing results were not very consistent between sessions, something which can be expected during exploratory platform development, during which everchanging bioink and especially bath compositions and combinations thereof were explored, combined with a wide variety of g-codes, needle sizes and geometries, showed the platform's sensitivity to the interplay between its constituent components.
Most important to shape fidelity was to achieve the desired φ_p set at 0.1 at extrusion. This was however difficult to realise in practice, for slight deviation between assumed and true cell sizes resulted in relatively large volumetric differences (e.g. difference between $\emptyset_{avr}$ 20 μm and $\emptyset_{avr}$ 19 μm is -15% volume).
When this is combined with the discrepancies in assumed particle and carrier fluid densities, influencing local φ_p on a temporal manner, resulted in non-equal infill rates and thus inconsistent results which were only noticeable after printing due to the lack in the ability to monitoring the printing process in real-time.

Analysis from printed tissues the interior of was not performed, beyond the confocal penetration depth up to 60-70 μm, a distance readily exceeded by most tissue diameters. Discussions and conclusions about for example underlaying cellular compaction, organisation, viability, function, dissociation, maturation, nutrients availability, and debris build-up, could therefore not be addressed in detail and will have to be subject of future study.

Of note is the tendency for SMC tissues, separate or in spheroids, co-printed with Col-PLA-μp to become increasingly more spherical during culture, while tissue printed with only SMC-spheroids remain mostly in their respective shapes after fusion, although this is a small sample size.
The significant difference in the extent of cellular reorganisation can likely be ascribed to the cells' mechano-response to the presence of said particles, however, the bath compositions also differed with 0.75% (w/v) in SMC-GM1 for SMC-spheroids and 1.5% (w/v) XG in SMC-GM2 in the combined prints. The difference in rheological properties might have been sufficient to significantly alter its supporting capabilities. [54]
It has been shown that the post-print geometric developments of tissue constructs can be accurately and productively described using a model based on the cell-generated forces, tissue elastic modulus, tissue geometry, the gel's G' and G'' and its yield stress. [113] These include the buckling, breakup, and axial contraction of high aspect ratio beams (fibres) at sufficiently high cell forces or low tissue stiffness. Thes model might be applicable to this platform and describe developments seen during this research.

6.4 Platform potential

6.4.1 Examination of novel printing mechanisms

The printing of Newtonian (aqueous) and non-Newtonian (XG) bioinks in Newtonian (XG/SA) and yield stress thinning non-Newtonian (XG) embedding baths was examined. The diffusion mechanism, which was to the best of our knowledge first described in detail and utilized in the paper based on this research, was distinctly present when using Newtonian bioinks in non-Newtonian baths. [65] Although not stated explicitly in literature, it is expected to be present in most embedding printing works when printing in yield stress fluid. It resembles a diffusion evaporation method used for fabricating ultrathin PLC-membranes. [37] [114] Its local particle density increase effect was the main focus during this platform initial development. It was therefore recorded in detail using a custom setup, which enabled the capture of the presence and position of XG, bioink's carrier fluid, and suspended particles in real-time.

Due to the lack of an ionic, photonic, enzymatic, or thermal stabilizing method, the low viscosity ink had to be retained by the bath itself, demanding a needle with bend geometry, reducing printing geometry freedom. This however, resulting in good shape fidelity and shape stability comparable to previous works utilizing post-print stabilisation in XG embedding bath. [37] The novel printing platform may be classified as a very simplified kind of ''4D-printing'', by allowing for the creation of post-print features, when exposed to external stimuli (i.e. removal of the carrier fluid and surrounding hydrogel matrix swelling), which are difficult or impossible to fabricate when exclusively utilizing the extrusion printing method. [115], [116]

6.4.2 Demonstrating platform possibilities

To show the platform's potential in 3D-tissue formation, stable tissue fibres were printed from a variety of aqueous cell-tailored bioinks and corresponding embedding baths. Unlike most extrusion 3D printing methods, features were formed smaller than the needle $Ø_{OD}$. Fibre diameter is primarily a product of the infill rate, regulated by the product of ink volume over travel distance (extrusion value) and volume fraction (φ_p). To a lesser extent the nozzle gauge also influences feature sizes by governing the extent of bath liquification which in turn regulates the area in which bioink can be deposited homogenously, altering pre-compaction conditions and its outcome.
Preliminary results indicate the possibility for creating tissue sheet by way of sideways extrusion, proximal fibre fusion or printing of a fibre mesh. [65]

The chemotactically biocompatible property of XG allowed for the self-assembly and reorganisation of tissue constructs to occur while experiencing minimal interaction with materials the novel printing platform utilized. All tissues showed different functionalities, correlating to their components and print conditions.

By printing diluted hydrogel bioinks the absence of intra-particle hydrogel was demonstrated to be essential for the formation of dense stable tissue constructs, something the diffusion packing mechanism facilitates.

The fast-proliferating cell-types iPSCs and SMCs showed rapid development of mechanically stable constructs and tissue volume growth until the experiment was terminated.

A heterogenous mix of CMs/ECCs first compacted and then self-organised in a dense tissue which, and after a brief but extensive remodelling period of ±2 days, held their fibre shape if sufficient cell densities were present. Already after 24 hours a clear spatial difference in cell-type prevalence could be seen, with ECCs covering the outer surface of an interior comprised almost exclusively of CMs, mimicking their respective *in vivo* positions.

Both printed tissues comprised of CMs and CMs/ECCs started spontaneous contracting after a culture timeframe about double that to those of CM monolayer culture. Being susceptible to electrical stimulation, they could accurately follow pulses up to at least 4.0 Hz. Their contraction was however minor due to the sarcomere orientation being mostly randomly, possibly due to a lack of stable anchor points.

All XG-based embedding bath had minimum number of components, only consisting of cell-specific medium and XG powder. It is highly utilized, cheap, and therefor available to most (cell culture) laboratories. Preparation consisted of a simple mixing step, creating a hydrogel nutritionally near identical to well-established cell culture media.

Analogous to the XG-based embedding baths, the bioinks used were simple, inexpensive, and quick to fabricate. Only composed of a water-based particles suspension, it is highly adaptable regarding particle/cell types and sizes, carrier fluid composition, and the addition and inclusions multiple particle-types simultaneously, like hydrogel beads, μparticles, pigments, cells and cell spheroids. The rheological behaviour was highly consistent and thus predictable. No supporting matrix like hydrogel is needed for post-print stabilisation, which expands the ranges (of e.g. pH, temperatures, shear stresses, crosslinking agents) at which this bioink can be used such that it can be tailored to specific (cell) function and optimized cell viability during printing. [76] The major restrictions consist of their particle-to-nozzle size ratio and the necessity for all ink components to have similar densities.

To free printed constructs no scaffold removal methods, such as altering bath temperature, pH, or the addition of enzymes, have to be employed for removing the embedding bath, which have the potential to negatively impact cell function and viability. Instead, simple repeated dilutions were sufficient to incrementally reduce XG concentration. If this step is performed using culture medium, it has an additional benefit by substituting regular medium refreshments, increasing platform practicality, and mimicking common cell culture practices. The most prominent disadvantage of dilution is the required slow dilution and thus time, which is, due to its disruptive effect, mostly dependent on the construct mechanical stability.

Chapter 7. Conclusion

This research shows the initial development of a novel 3D-extrusion printing platform and its ability to successfully form cell tissue and particle constructs of predefined dense spheroid or fibres, from dilute aqueous suspension bioinks. It utilizes a XG-based hydrogel embedding bath which was, using cell-specific medium as the liquid component, specifically tailored to a compromise between exhibiting rheological properties and providing cell-specific culture conditions. The diffusion packing mechanism, not known to be discussed in literature previously, is comprised of the dissipation of bioink carrier fluid into the surrounding bath, by way of diffusion, followed by the intrusive swelling of hydrogel matrix, forming a net which drives allow sufficiently large particles together. It is characteristic to the XG-bath when printing aqueous Newtonian bioink, and results in a dramatic increase in local particle density along the printing axis or plane. This not only provides a passive mechanism for achieving high particle densities but also allows the printing of features significantly smaller than the needle's $\emptyset_{ID}$. Furthermore, the inability of cells to bind to and travel through the hydrogel matric assures minimal mechanotactic and hepatotactic cues and restricts cell motility.

Bioinks consisted only of a dilute Newtonian aqueous cell and/or particle suspension, where cell culture medium or other water-based liquid, substituted by a density modifier OptiPrep, acted as a carrier fluid.

Both the embedding bath and bioink are inexpensive, quick to manufacture, require few steps and limited initial bioprinting experience. All platform components: needles, g-codes, printers, containers, bioink compositions, and embedding bath compositions are highly customizable. Excessing printed constructs for retrieval and the providing of necessary nutrients were combined by simply diluting the XG, the rate of which could be adjusted to the construct properties and requirements.

The biological utilization was demonstrated with the successful printing and post printing culture of fibre (1.5D) tissues comprised of proliferating cells, non-proliferating cells, combinations of different cell types, spheroids, and/or Col-PLA-μparticles. Which all show cell-type specific functionalities such as CM sarcomere formation, subsequent spontaneous and electrically stimulated contraction; the self-reorganisation of different co-printed cell types to more *in vivo*-like relative cell positioning in CM/ECCs tissues; the continuous tissue volume increase during culture of proliferating SMCs and iPSCs and the extensive cellular reorganisation when printing SMCs and μparticles, leading to their successful incorporation.

The results obtained and possibility for a high-level of optimization and customisation allows for the presentation of a promising easy to adopt novel 3D-bioprinting platform.

Chapter 8. Future Outlook

8.1 Embedding bath

The acetyl and pyruvyl residues vary with bacterial species and fermentation conditions within the XG broths. These contents of the secondary structure, together with the solution's pH, ionic strength and the presence and nature of electrolytes, influence the form of the physical networks by influencing intramolecular crosslinking and chain geometry. [66]
This translates into differences in rheological properties between embedding baths prepared with different liquids or solutions, like cell culture media, and XG batches, the exact composition of which is not disclosed by the manufacture. Especially the thixotropic characteristics, influencing surface tension, viscosity, bath recovery after shearing, and the extent of disruption around a traveling needle, has the potential to be subject of extensive optimisation. Rheological studies on XG/medium hydrogels spanning a range of XG concentrations and different cell-specific culture media prior to printing should be performed to specify and optimise each embedding bath to experiment specific goals.

XG powder supplied is not sterile, harbouring unknown sources for infections. Exposing the powder to UV for >10 minutes does seem to incapacitate most, for it has been observed the number of infections were reduced significantly after this treatment.

As a result of the hydrogel discolouration, discussed in **§6.1.3.2**, experiments researching (gas) diffusion rates through XG-hydrogels are recommended to investigate the nutrients availability, or lack thereof, inside a embedding bath during cell culture, as done for oxygen availability in SHAPE printing by Katjez *et al*. (2022). [53] Experiments may have to be designed with this limit in mind, especially regarding guidelines on the density and proximity of constructs, construct size, bath removal rates, bath hight, XG-concentration, ambient gas concentrations, and type of cell medium (e.g. increased nutrient concentrations).

Although bare XG being is biocompatible, it can be chemically modified, with for example citric acid (CA) as a polysaccharide crosslinker, to display of specific chemical and physical ques with tailored effect on tissue development. [62], [73], [117]
Patterning using distinctly modified sections of XG may even be used for local development of a continuous tissue or collection of tissue, as demonstrated in Trikalitis et al. (2023) S6. [65]

The initial experiments showed to potential for more concentrated bioink retention with diffusion packing still present. Hypothesised to be a consequence of the presents of an additional fungal network, replicating this effect by introducing a secondary hydrogel network can be subject of great interest to enhance the platform by allowing more geometric freedom in printing designs.

Further study into the diffusion packing mechanism will enable finer control on final ink deposition and thus tissue formation. Besides the diffusion speeds experiments, the travel distances of larger particles are important to analyse. By printing an ink of heterogeneous suspension carrying distinguishable particles with sizes spanning multiple orders of magnitude, the netting ability of the hydrogel network can be evaluated.

Similar to Wu *et al*. (2011) the vertical cavity does not collapse readily in the needles wake. [46] A thin liquid layer of Newtonian filler placed on the bath surface filling this cavity readily which stabilises the deposited ink might be implemented to reduce sheet formation.

In SHAPE printing by Kajtez *et al*. (2022) a viscous fluid in is introduced between dispersed microgels, resulting in excellent shape retention provided by granular gels while also providing the diversity of bulk hydrogel formulations. [53] It might be possible to replace the annealing step, performed enzymatically, photonically, or ionically, to retain the printed constructs via the diffusion packing mechanism when the continuous phase (intra-granular) is to be XG.

8.2 Inks

A φ_p of 0.1 was sufficient to be printed into stable tissue fibre formations. No clogging events were thought to be (exclusively) the result of too high φ_p, so future printing experiment will probably benefit from exploring higher φ_p, increasing the speed and ease of thick construct formation. The only immediate drawbacks being the higher number of unusable particles/cells lost in the dead volume and higher changes of clogging.

As demonstrated by the Col-PLA-μp's, incorporation of additional components, can guide cell behaviour towards desired tissue formation like reorganisation and quick mechanical stability. Expanding upon this the proliferation, differentiation and maturity can be guided by the use of (cell laden) hydrogel beads [118], (sustained) growth factors release [119], the compartmentalized surface properties of Janus interfaces [106] and modified surface that can interact on demand with cells [120].
Even if particles have little influence on cell behaviour, their inclusion has the benefit of lowering cell usage while keeping or increasing φ_p. After their incorporation they

can be removed, for example the use of chelating agents to dissolve SA, exposes hollow area's which can be used for the supply of nutrients or be seeded by additional cell types, for example endothelial cells forming lumen.

Density differences between particles and between particles and carrier liquid have shown to result in relative displacement inside the printed ink column. This occurs in a short window of time before diffusion packing restricts particle movement during which this sinking or rising can be utilized for even denser and more localized deposition.

8.3 Setup changes and additions

8.3.1 Needle architecture

Although difficult to implement in the current 3D-printer setup, implementation of glass needles exhibits significant benefit over the syringe and Luer-Lock needle assembly, especially when printing low-complexity shapes such as fibres. [54] It has the potential to reduce dead volume, allows finer extrusion control, and would allow real-time observations with quick adjustments for better printing results.

printing a cylindrical column of XG simultaneously with bioink in its centre from a coaxial needle, has the potential to greatly reduce XG volume while still benefiting from diffusion packing. If switched, printing a centre column of XG while extruding bioink, might be a way to form hollow fibres if, after the tissue is sufficiently stable, the XG can be flushed or diluted.

Although the current flowrates are very low, these may be increased in future experiments. The viability of cell during extrusion depends mostly depend on shear stresses influenced by pressures and internal needle geometries. Li *et al*. (2011) compared viability in conical (tapered) and cylindrical nozzles both mathematically and experimentally and found tapered needles to produce much higher flowrates under the same pressure and induces far less cell damage under the same flowrates and needle $Ø_{ID}$. [56] Optimization of high throughput 3D-bioprinting might therefor benefit from use needles with more tapered features.

8.3.2 3D-printer

The 3D-printer's drawbacks discussed in **§6.1.4** does put limits on its usability in future experiments. Most importantly for dense tissue formation is the delicate window of time for initial diffusion packing, during which bath distortions should be kept at a minimum, the movement of a proximal needle should be highly controllable, like acceleration, jerk and pausing, ideally while keeping the device turned on.
The most important missing feature for more complex tissue formation is the ability to rotate either the needle or embedding bath around the vertical axis. In future experiments aiming for more complex designs, higher throughput and increased reproducibility, the implementation of a 3D-printer with these additional specifications is recommended.

8.3.3 Culture and in bath tissue development

Because the embedding bath prevents cell migration throughout, a co-culture in of different cell types can be easily established without the use of a physical barrier or channel while still allowing, for example, paracrine and endocrine signalling molecules to diffuse and function.

If the bath rheology allows it, additional printing can be performed to enhance tissue integrity by introducing additional particles/cells and by sequentially tailoring conditions to the development distinct sections of the construct. During and after bath dilution tissue development can be stimulated by the relatively easy addition or removal of chemical (e.g., growth factors), biological (e.g., cells), biophysical (e.g., particles) or electrical (e.g., electrical pulsation) ques.

8.3.4 Construct extraction

The current dilution method for tissue extraction requires the tissue to become mechanically stable enough for its shape to remain undistorted. An alternative method using full submersion, similar to Patrício *et al*. (2020) or establishing a constant flow has the potential to reduce dilution times significantly down to hours while exposing the tissue to the similar or less disruptive forces. [37]

Like mentioned previously, the rheological properties of XG-based hydrogels allow for the approximation of similar rheological properties in a broad temperature range, which allows for consistent printing performances at temperatures which can be tuned to specific bioink stabilisation methods (e.g., cross-linking or temperature-responsive mechanical properties). The opacity of medium-based XG-hydrogels may also allow for the utilization of UV-based stabilisation methods.

8.4 Internal tissue observations

Observing the progression of tissue development during these experiments was limited only to optical data (transmission and fluorescent) retrieved from a shallow layer of the construct's periphery with little information on its interior regarding structure or cell conditions. In addition to generating less dense tissues, using for example, (destructive) essays of viability staining or tissue sectioning, the internal processes could be visualized and tracked, generating considerably greater insight into the remodelling, and functioning of regions located deeper.

Chapter 9. Bibliography

[1] N. Academy, O. F. Sciences, N. Academy, and O. F. Engineering, *Science, Medicine, and Animals*. 1991.

[2] M. Hauswald, *Use of laboratory animals [16]*, vol. 353, no. 9168. 1999. doi: 10.1016/S0140-6736(05)77196-8.

[3] J. Egido *et al.*, "Animal models of cardiovascular diseases," *Journal of Biomedicine and Biotechnology*, vol. 2011, 2011, doi: 10.1155/2011/497841.

[4] R. Greek and A. Menache, "Systematic reviews of animal models: Methodology versus epistemology," *International Journal of Medical Sciences*, vol. 10, no. 3, pp. 206–221, 2013, doi: 10.7150/ijms.5529.

[5] W. Ernst, "Humanized mice in infectious diseases," *Comparative Immunology, Microbiology and Infectious Diseases*, vol. 49, pp. 29–38, 2016, doi: 10.1016/j.cimid.2016.08.006.

[6] S. W. Glickman *et al.*, "Ethical and Scientific Implications of the Globalization of Clinical Research," *New England Journal of Medicine*, vol. 360, no. 8, pp. 816–823, 2009, doi: 10.1056/nejmsb0803929.

[7] "Health Social Care Comm - 2004 - Hussain-Gambles.pdf."

[8] K. Duval *et al.*, "Modeling physiological events in 2D vs. 3D cell culture," *Physiology*, vol. 32, no. 4, pp. 266–277, 2017, doi: 10.1152/physiol.00036.2016.

[9] N. T. Elliott and F. Yuan, "A review of three-dimensional in vitro tissue models for drug discovery and transport studies," *Journal of Pharmaceutical Sciences*, vol. 100, no. 1, pp. 59–74, 2011, doi: 10.1002/jps.22257.

[10] A. Shapira and T. Dvir, "3D Tissue and Organ Printing—Hope and Reality," *Advanced Science*, vol. 8, no. 10. 2021. doi: 10.1002/advs.202003751.

[11] M. Dey and I. T. Ozbolat, "3D bioprinting of cells, tissues and organs," *Scientific Reports*, vol. 10, no. 1, pp. 10–12, 2020, doi: 10.1038/s41598-020-70086-y.

[12] S. V. Murphy and A. Atala, "3D bioprinting of tissues and organs," *Nature Biotechnology*, vol. 32, no. 8, pp. 773–785, 2014, doi: 10.1038/nbt.2958.

[13] D.-H. Kang *et al.*, "Engineered whole cut meat-like tissue by the assembly of cell fibers using tendon-gel integrated bioprinting," *Nature Communications*, vol. 12, no. 1, 2021, doi: 10.1038/s41467-021-25236-9.

[14] C. Jensen and Y. Teng, "Is It Time to Start Transitioning From 2D to 3D Cell Culture?," *Frontiers in Molecular Biosciences*, vol. 7, no. March, pp. 1–15, 2020, doi: 10.3389/fmolb.2020.00033.

[15] M. Hospodiuk, M. Dey, D. Sosnoski, and I. T. Ozbolat, "The bioink: A comprehensive review on bioprintable materials," *Biotechnology Advances*, vol. 35, no. 2, pp. 217–239, 2017, doi: 10.1016/j.biotechadv.2016.12.006.

[16] M. Hofer and M. P. Lutolf, "Engineering organoids," *Nature Reviews Materials*, vol. 6, no. 5, pp. 402–420, 2021, doi: 10.1038/s41578-021-00279-y.

[17] I. T. Ozbolat, W. Peng, and V. Ozbolat, "Application areas of 3D bioprinting," *Drug Discovery Today*, vol. 21, no. 8, pp. 1257–1271, 2016, doi: 10.1016/j.drudis.2016.04.006.

[18] A. Jayswal and S. Adanur, "An overview of additive manufacturing methods, materials, and applications for flexible structures," *Journal of Industrial Textiles*, vol. 52, pp. 1–42, 2022, doi: 10.1177/15280837221114638.

[19] M. A. Skylar-scott, J. Mueller, C. W. Visser, and J. A. Lewis, "Voxelated soft matter via multimaterial multinozzle 3D printing," *Nature*, vol. 575, no. November, 2019, doi: 10.1038/s41586-019-1736-8.

[20] A. Lee *et al.*, "3D bioprinting of collagen to rebuild components of the human heart," *Science*, vol. 365, no. 6452, pp. 482–487, 2019, doi: 10.1126/science.aav9051.

[21] J. Malda *et al.*, "25th anniversary article: Engineering hydrogels for biofabrication," *Advanced Materials*, vol. 25, no. 36, pp. 5011–5028, 2013, doi: 10.1002/adma.201302042.

[22] A. Ovsianikov, A. Khademhosseini, and V. Mironov, "The Synergy of Scaffold-Based and Scaffold-Free Tissue Engineering Strategies," *Trends in Biotechnology*, vol. 36, no. 4, pp. 348–357, 2018, doi: 10.1016/j.tibtech.2018.01.005.

[23] N. Khoshnood and A. Zamanian, "A comprehensive review on scaffold-free bioinks for bioprinting," *Bioprinting*, vol. 19, no. May, p. e00088, 2020, doi: 10.1016/j.bprint.2020.e00088.

[24] B. S. Schon, G. J. Hooper, and T. B. F. Woodfield, "Modular Tissue Assembly Strategies for Biofabrication of Engineered Cartilage," *Annals of Biomedical Engineering*, vol. 45, no. 1, pp. 100–114, 2017, doi: 10.1007/s10439-016-1609-3.

[25] A. Panwar and L. P. Tan, "Current status of bioinks for micro-extrusion-based 3D bioprinting," *Molecules*, vol. 21, no. 6, 2016, doi: 10.3390/molecules21060685.

[26] G. Cidonio, M. Glinka, J. I. Dawson, and R. O. C. Oreffo, "The cell in the ink: Improving biofabrication by printing stem cells for skeletal regenerative medicine," *Biomaterials*, vol. 209, no. November 2018, pp. 10–24, 2019, doi: 10.1016/j.biomaterials.2019.04.009.

[27] I. N. Aguilar *et al.*, "Scaffold-free bioprinting of mesenchymal stem cells using the Regenova printer: Spheroid characterization and osteogenic differentiation," *Bioprinting*, vol. 15, no. October 2018, p. e00050, 2019, doi: 10.1016/j.bprint.2019.e00050.

[28] T. Bhattacharjee *et al.*, "Writing in the granular gel medium," *Science Advances*, vol. 1, no. 8, 2015, doi: 10.1126/sciadv.1500655.

[29] M. E. Cooke and D. H. Rosenzweig, "The rheology of direct and suspended extrusion bioprinting," *APL Bioengineering*, vol. 5, no. 1, 2021, doi: 10.1063/5.0031475.

[30] K. Da Silva, P. Kumar, Y. E. Choonara, L. C. du Toit, and V. Pillay, "Three-dimensional printing of extracellular matrix (ECM)-mimicking scaffolds: A critical review of the current ECM materials," *Journal of Biomedical Materials Research Part A*, vol. 108, no. 12, pp. 2324–2350, Dec. 2020, doi: https://doi.org/10.1002/jbm.a.36981.

[31] M. Ali, P. R. Anil Kumar, J. J. Yoo, F. Zahran, A. Atala, and S. J. Lee, "A Photo-Crosslinkable Kidney ECM-Derived Bioink Accelerates Renal Tissue Formation," *Advanced Healthcare Materials*, vol. 8, no. 7, Apr. 2019, doi: 10.1002/adhm.201800992.

[32] F. Pati *et al.*, "Printing three-dimensional tissue analogues with decellularized extracellular matrix bioink," *Nature Communications*, vol. 5, 2014, doi: 10.1038/ncomms4935.

[33] D. B. Kolesky, R. L. Truby, A. S. Gladman, T. A. Busbee, K. A. Homan, and J. A. Lewis, "3D bioprinting of vascularized, heterogeneous cell-laden tissue constructs," *Advanced Materials*, vol. 26, no. 19, pp. 3124–3130, 2014, doi: 10.1002/adma.201305506.

[34] K. Hölzl, S. Lin, L. Tytgat, S. Van Vlierberghe, L. Gu, and A. Ovsianikov, "Bioink properties before, during and after 3D bioprinting," *Biofabrication*, vol. 8, no. 3, 2016, doi: 10.1088/1758-5090/8/3/032002.

[35] A. Shapira, N. Noor, M. Asulin, and T. Dvir, "Stabilization strategies in extrusion-based 3D bioprinting for tissue engineering," *Applied Physics Reviews*, vol. 5, no. 4, 2018, doi: 10.1063/1.5055659.

[36] J. Lewicki, J. Bergman, C. Kerins, and O. Hermanson, "Optimization of 3D bioprinting of human neuroblastoma cells using sodium alginate hydrogel," *Bioprinting*, vol. 16, no. February, p. e00053, 2019, doi: 10.1016/j.bprint.2019.e00053.

[37] S. G. Patrício *et al.*, "Freeform 3D printing using a continuous viscoelastic supporting matrix," *Biofabrication*, vol. 12, no. 3, pp. 1–4, 2020, doi: 10.1088/1758-5090/ab8bc3.

[38] D. B. Kolesky, K. A. Homan, M. A. Skylar-Scott, and J. A. Lewis, "Three-dimensional bioprinting of thick vascularized tissues," *Proceedings of the National Academy of Sciences of the United States of America*, vol. 113, no. 12, pp. 3179–3184, 2016, doi: 10.1073/pnas.1521342113.

[39] C. B. Highley, C. B. Rodell, and J. A. Burdick, "Direct 3D Printing of Shear-Thinning Hydrogels into Self-Healing Hydrogels," *Advanced Materials*, vol. 27, no. 34. pp. 5075–5079, 2015. doi: 10.1002/adma.201501234.

[40] N. Noor, A. Shapira, R. Edri, I. Gal, L. Wertheim, and T. Dvir, "3D Printing of Personalized Thick and Perfusable Cardiac Patches and Hearts," *Advanced Science*, vol. 6, no. 11, 2019, doi: 10.1002/advs.201900344.

[41] A. Shapira, N. Noor, H. Oved, and T. Dvir, "Transparent support media for high resolution 3D printing of volumetric cell-containing ECM structures," *Biomedical Materials (Bristol)*, vol. 15, no. 4, 2020, doi: 10.1088/1748-605X/ab809f.

[42] H. W. Kang, S. J. Lee, I. K. Ko, C. Kengla, J. J. Yoo, and A. Atala, "A 3D bioprinting system to produce human-scale tissue constructs with structural integrity," *Nature Biotechnology*, vol. 34, no. 3, pp. 312–319, 2016, doi: 10.1038/nbt.3413.

[43] C. Norotte, F. S. Marga, L. E. Niklason, and G. Forgacs, "Scaffold-free vascular tissue engineering using bioprinting," *Biomaterials*, vol. 30, no. 30, pp. 5910–5917, 2009, doi: 10.1016/j.biomaterials.2009.06.034.

[44] Q. Li *et al.*, "Regulable Supporting Baths for Embedded Printing of Soft Biomaterials with Variable Stiffness," *ACS Applied Materials and Interfaces*, vol. 14, no. 37, pp. 41695–41711, 2022, doi: 10.1021/acsami.2c09221.

[45] C. S. O'Bryan *et al.*, "Self-assembled micro-organogels for 3D printing silicone structures," *Science Advances*, vol. 3, no. 5, 2017, doi: 10.1126/sciadv.1602800.

[46] W. Wu, A. Deconinck, and J. A. Lewis, "Omnidirectional printing of 3D microvascular networks," *Advanced Materials*, vol. 23, no. 24, pp. 178–183, 2011, doi: 10.1002/adma.201004625.

[47] S. G. Patrício *et al.*, "Freeform 3D printing using a continuous viscoelastic supporting matrix," 2020, doi: 10.1088/1758-5090/ab8bc3.

[48] N. Noor, A. Shapira, R. Edri, I. Gal, L. Wertheim, and T. Dvir, "3D Printing of Personalized Thick and Perfusable Cardiac Patches and Hearts," *Advanced Science*, vol. 6, no. 11, 2019, doi: 10.1002/advs.201900344.

[49] T. J. Hinton *et al.*, "Three-dimensional printing of complex biological structures by freeform reversible embedding of suspended hydrogels," *Science Advances*, vol. 1, no. 9, 2015, doi: 10.1126/sciadv.1500758.

[50] Y. Wang *et al.*, "Direct writing alginate bioink inside pre-polymers of hydrogels to create patterned

vascular networks," *Journal of Materials Science*, vol. 54, no. 10, pp. 7883–7892, 2019, doi: 10.1007/s10853-019-03447-2.

[51] T. J. Hinton *et al.*, "Three-dimensional printing of complex biological structures by freeform reversible embedding of suspended hydrogels," *Science Advances*, vol. 1, no. 9, 2015, doi: 10.1126/sciadv.1500758.

[52] D. J. Shiwarski, A. R. Hudson, J. W. Tashman, and A. W. Feinberg, "Emergence of FRESH 3D printing as a platform for advanced tissue biofabrication," *APL Bioengineering*, vol. 5, no. 1, 2021, doi: 10.1063/5.0032777.

[53] J. Kajtez *et al.*, "Embedded 3D Printing in Self-Healing Annealable Composites for Precise Patterning of Functionally Mature Human Neural Constructs," *Advanced Science*, vol. 9, no. 25, pp. 1–13, 2022, doi: 10.1002/advs.202201392.

[54] J. A. Brassard, M. Nikolaev, T. Hübscher, M. Hofer, and M. P. Lutolf, "Recapitulating macro-scale tissue self-organization through organoid bioprinting," *Nature Materials*, vol. 20, no. 1, pp. 22–29, 2021, doi: 10.1038/s41563-020-00803-5.

[55] O. Jeon, Y. Bin Lee, H. Jeong, S. J. Lee, D. Wells, and E. Alsberg, "Individual cell-only bioink and photocurable supporting medium for 3D printing and generation of engineered tissues with complex geometries," *Materials Horizons*, vol. 6, no. 8, pp. 1625–1631, 2019, doi: 10.1039/c9mh00375d.

[56] M. Li, X. Tian, D. J. Schreyer, and X. Chen, "Effect of needle geometry on flow rate and cell damage in the dispensing-based biofabrication process," *Biotechnology Progress*, vol. 27, no. 6, pp. 1777–1784, Nov. 2011, doi: https://doi.org/10.1002/btpr.679.

[57] S. Mueller, E. W. Llewellin, and H. M. Mader, "The rheology of suspensions of solid particles," no. November 2009, pp. 1201–1228, 2010, doi: 10.1007/BF01432034.

[58] A. Iordan, A. Duperray, and C. Verdier, "Fractal approach to the rheology of concentrated cell suspensions," *Physical Review E - Statistical, Nonlinear, and Soft Matter Physics*, vol. 77, no. 1, pp. 2–7, 2008, doi: 10.1103/PhysRevE.77.011911.

[59] M. Souzy, I. Zuriguel, and A. Marin, "Transition from clogging to continuous flow in constricted particle suspensions," *Physical Review E*, vol. 101, no. 6, 2020, doi: 10.1103/PhysRevE.101.060901.

[60] A. Marin, H. Lhuissier, M. Rossi, and C. J. Kähler, "Clogging in constricted suspension flows," *Physical Review E*, vol. 97, p. 21102, 2018, doi: 10.1103/PhysRevE.97.021102.

[61] M. Müller, E. Öztürk, Ø. Arlov, P. Gatenholm, and M. Zenobi-Wong, "Alginate Sulfate–Nanocellulose Bioinks for Cartilage Bioprinting Applications," *Annals of Biomedical Engineering*, vol. 45, no. 1, pp. 210–223, 2017, doi: 10.1007/s10439-016-1704-5.

[62] D. F. S. Petri, "Xanthan gum: A versatile biopolymer for biomedical and technological applications," *Journal of Applied Polymer Science*, vol. 132, no. 23, 2015, doi: 10.1002/app.42035.

[63] D. Bergmann, G. Furth, and C. Mayer, "Binding of bivalent cations by xanthan in aqueous solution," *International Journal of Biological Macromolecules*, vol. 43, no. 3, pp. 245–251, 2008, doi: 10.1016/j.ijbiomac.2008.06.001.

[64] A. C. Daly, L. Riley, T. Segura, and J. A. Burdick, "Hydrogel microparticles for biomedical applications," *Nature Reviews Materials*, vol. 5, no. 1, pp. 20–43, 2020, doi: 10.1038/s41578-019-0148-6.

[65] V. D. Trikalitis *et al.*, "Embedded 3D printing of dilute particle suspensions into dense complex tissue fibers using shear thinning xanthan baths," *Biofabrication*, 2022, doi: 10.1088/1758-5090/aca124.

[66] A. Kumar, K. M. Rao, and S. S. Han, "Application of xanthan gum as polysaccharide in tissue engineering: A review," *Carbohydrate Polymers*, vol. 180, no. October 2017, pp. 128–144, 2018, doi: 10.1016/j.carbpol.2017.10.009.

[67] J. S. Lee and K. W. Song, "Time-dependent rheological behavior of natural polysaccharide xanthan gum solutions in interrupted shear and step-incremental/reductional shear flow fields," *Korea Australia Rheology Journal*, vol. 27, no. 4, pp. 297–307, 2015, doi: 10.1007/s13367-015-0029-5.

[68] J. Patel, B. Maji, N. S. H. N. Moorthy, and S. Maiti, "Xanthan gum derivatives: Review of synthesis, properties and diverse applications," *RSC Advances*, vol. 10, no. 45, pp. 27103–27136, 2020, doi: 10.1039/d0ra04366d.

[69] G. A. Saadatlou and G. Pircheraghi, "Concentrated regimes of xanthan-based hydrogels crosslinked with multifunctional crosslinkers," *Carbohydrate Polymer Technologies and Applications*, vol. 2, no. September 2020, 2021, doi: 10.1016/j.carpta.2021.100047.

[70] Y. Fan *et al.*, "Rheological thixotropy and pasting properties of food thickening gums orienting at improving food holding rate," *Applied Rheology*, vol. 32, no. 1, pp. 100–121, 2022, doi: 10.1515/arh-2022-0127.

[71] S. Ki-Won, K. Yong-Seok, and C. Gap-Shik, "Rheology of Concentrated Xanthan Gum Solutions.pdf." 2006.

[72] J. A. Carmona, N. Calero, P. Ramírez, and J. Muñoz, "Rheology and structural recovery kinetics of an advanced performance xanthan gum with industrial application," *Applied Rheology*, vol. 27, no. 2, pp. 1–9, 2017, doi: 10.3933/APPLRHEOL-27-25555.

[73] A. C. Alavarse, E. C. G. Frachini, J. B. Silva, R. dos S. Pereira, H. Ulrich, and D. F. S. Petri, "Amino acid decorated xanthan gum coatings: Molecular arrangement and cell adhesion," *Carbohydrate Polymer Technologies and Applications*, vol. 4, no. June, p. 100227, 2022, doi: 10.1016/j.carpta.2022.100227.

[74] Y. S. E. Tan and W. Y. Yeong, "Direct bioprinting of alginate-based tubular constructs using multi-nozzle extrusion-based technique," *Proceedings of the International Conference on Progress in Additive Manufacturing*, vol. 0, no. January, pp. 423–427, 2014, doi: 10.3850/978-981-09-0446-3_093.

[75] A. Blaeser, D. F. Duarte Campos, U. Puster, W. Richtering, M. M. Stevens, and H. Fischer, "Controlling Shear Stress in 3D Bioprinting is a Key Factor to Balance Printing Resolution and Stem Cell Integrity," *Advanced Healthcare Materials*, vol. 5, no. 3, pp. 326–333, 2016, doi: 10.1002/adhm.201500677.

[76] S. Boularaoui, G. Al Hussein, K. A. Khan, N. Christoforou, and C. Stefanini, "An overview of extrusion-based bioprinting with a focus on induced shear stress and its effect on cell viability," *Bioprinting*, vol. 20, no. August, p. e00093, 2020, doi: 10.1016/j.bprint.2020.e00093.

[77] A. Wyma, L. Martin-Alarcon, T. Walsh, T. A. Schmidt, I. D. Gates, and M. S. Kallos, "Non-Newtonian rheology in suspension cell cultures significantly impacts bioreactor shear stress quantification," *Biotechnology and Bioengineering*, vol. 115, no. 8. pp. 2101–2113, 2018. doi: 10.1002/bit.26723.

[78] S. Ansari, M. A. I. Rashid, P. R. Waghmare, and D. S. Nobes, "Measurement of the flow behavior index of Newtonian and shear-thinning fluids via analysis of the flow velocity characteristics in a mini-channel," *SN Applied Sciences*, vol. 2, no. 11, pp. 1–15, 2020, doi: 10.1007/s42452-020-03561-w.

[79] W. Kozicki, C. H. Chou, and C. Tiu, "Non-Newtonian flow in ducts of arbitrary cross-sectional shape," *Chemical Engineering Science*, vol. 21, no. 8, pp. 665–679, 1966, doi: 10.1016/0009-2509(66)80016-7.

[80] K. Nair *et al.*, "Characterization of cell viability during bioprinting processes," *Biotechnology Journal*, vol. 4, no. 8, pp. 1168–1177, 2009, doi: 10.1002/biot.200900004.

[81] OctoInkjet, "Neeldle supplier." [Online]. Available: https://www.needlez.co.uk

[82] P. Fomby *et al.*, "Stem cells and cell therapies in lung biology and diseases: Conference report," *Annals of the American Thoracic Society*, vol. 12, no. 3, pp. 181–204, 2010, doi: 10.1002/term.

[83] T. Yurugi-Kobayashi *et al.*, "Effective contribution of transplanted vascular progenitor cells derived from embryonic stem cells to adult neovascularization in proper differentiation stage," *Blood*, vol. 101, no. 7, pp. 2675–2678, 2003, doi: 10.1182/blood-2002-06-1877.

[84] T. Nagel, N. Resnick, W. J. Atkinson, C. F. Dewey, and M. A. Gimbrone, "Shear stress selectively upregulates intercellular adhesion molecule-1 expression in cultured human vascular endothelial cells," *Journal of Clinical Investigation*, vol. 94, no. 2, pp. 885–889, 1994, doi: 10.1172/jci117410.

[85] D. H. Kim, S. J. Heo, S. H. Kim, J. W. Shin, S. H. Park, and J. W. Shin, "Shear stress magnitude is critical in regulating the differentiation of mesenchymal stem cells even with endothelial growth medium," *Biotechnology Letters*, vol. 33, no. 12, pp. 2351–2359, 2011, doi: 10.1007/s10529-011-0706-5.

[86] C. C. Wu *et al.*, "Synergism of biochemical and mechanical stimuli in the differentiation of human placenta-derived multipotent cells into endothelial cells," *Journal of Biomechanics*, vol. 41, no. 4, pp. 813–821, 2008, doi: 10.1016/j.jbiomech.2007.11.008.

[87] N. Gomes, C. Legrand, and F. Fauvel-Lafève, "Shear stress induced release of von Willebrand factor and thrombospondin-1 in HUVEC extracellular matrix enhances breast tumour cell adhesion," *Clinical and Experimental Metastasis*, vol. 22, no. 3, pp. 215–223, 2005, doi: 10.1007/s10585-005-7359-5.

[88] J. Shen, F. W. Luscinskas, A. Connolly, C. F. Dewey, and M. A. Gimbrone, "Fluid shear stress modulates cytosolic free calcium in vascular endothelial cells," *American Journal of Physiology - Cell Physiology*, vol. 262, no. 2 31-2, pp. 384–390, 1992, doi: 10.1152/ajpcell.1992.262.2.c384.

[89] Y. H. Datta and B. M. Ewenstein, "Regulated secretion in endothelial cells: biology and clinical implications.," *Thrombosis and haemostasis*, vol. 86, no. 5, pp. 1148–1155, Nov. 2001.

[90] T. Pongjanyakul and S. Puttipipatkhachorn, "Xanthan-alginate composite gel beads: Molecular interaction and in vitro characterization," *International Journal of Pharmaceutics*, vol. 331, no. 1, pp. 61–71, 2007, doi: 10.1016/j.ijpharm.2006.09.011.

[91] E. E. S. Ong, "Yield stress measurement of a thixotropic colloid," pp. 383–401, 2019.

[92] J. T. Muth *et al.*, "Embedded 3D printing of strain sensors within highly stretchable elastomers," *Advanced Materials*, vol. 26, no. 36, pp. 6307–6312, 2014, doi: 10.1002/adma.201400334.

[93] K. Dubbin, Y. Hori, K. K. Lewis, and S. C. Heilshorn, "Dual-Stage Crosslinking of a Gel-Phase Bioink Improves Cell Viability and Homogeneity for 3D Bioprinting," *Advanced Healthcare Materi-*

als, vol. 5, no. 19, pp. 2488–2492, 2016, doi: 10.1002/adhm.201600636.

[94] J. H. Galarraga, M. Y. Kwon, and J. A. Burdick, "3D bioprinting via an in situ crosslinking technique towards engineering cartilage tissue," *Scientific Reports*, vol. 9, no. 1, pp. 1–12, 2019, doi: 10.1038/s41598-019-56117-3.

[95] W. Lee *et al.*, "Three-dimensional bioprinting of rat embryonic neural cells," *NeuroReport*, vol. 20, no. 8, pp. 798–803, 2009, doi: 10.1097/WNR.0b013e32832b8be4.

[96] B. Grigoryan *et al.*, "Multivascular networks and functional intravascular topologies within biocompatible hydrogels," *Science*, vol. 364, no. 6439, pp. 458–464, 2019, doi: 10.1126/science.aav9750.

[97] M. E. Pepper, V. Seshadri, T. C. Burg, K. J. L. Burg, and R. E. Groff, "Characterizing the effects of cell settling on bioprinter output," *Biofabrication*, vol. 4, no. 1, 2012, doi: 10.1088/1758-5082/4/1/011001.

[98] K. Dubbin, Y. Hori, K. K. Lewis, and S. C. Heilshorn, "Dual-Stage Crosslinking of a Gel-Phase Bioink Improves Cell Viability and Homogeneity for 3D Bioprinting," *Advanced Healthcare Materials*, vol. 5, no. 19, pp. 2488–2492, 2016, doi: 10.1002/adhm.201600636.

[99] M. C. Ribeiro *et al.*, "A cardiomyocyte show of force: A fluorescent alpha-actinin reporter line sheds light on human cardiomyocyte contractility versus substrate stiffness," *Journal of Molecular and Cellular Cardiology*, vol. 141, pp. 54–64, Apr. 2020, doi: 10.1016/j.yjmcc.2020.03.008.

[100] V. Schwach *et al.*, "A COUP-TFII Human Embryonic Stem Cell Reporter Line to Identify and Select Atrial Cardiomyocytes," *Stem Cell Reports*, vol. 9, no. 6, pp. 1765–1779, 2017, doi: 10.1016/j.stemcr.2017.10.024.

[101] M. J. Birket *et al.*, "Contractile Defect Caused by Mutation in MYBPC3 Revealed under Conditions Optimized for Human PSC-Cardiomyocyte Function," *Cell Reports*, vol. 13, no. 4, pp. 733–745, 2015, doi: 10.1016/j.celrep.2015.09.025.

[102] E. S. Ng, R. Davis, E. G. Stanley, and A. G. Elefanty, "A protocol describing the use of a recombinant protein-based, animal product-free medium (APEL) for human embryonic stem cell differentiation as spin embryoid bodies," *Nature Protocols*, vol. 3, no. 5, pp. 768–776, 2008, doi: 10.1038/nprot.2008.42.

[103] J. A. Guadix *et al.*, "Human Pluripotent Stem Cell Differentiation into Functional Epicardial Progenitor Cells," *Stem Cell Reports*, vol. 9, no. 6, pp. 1754–1764, 2017, doi: 10.1016/j.stemcr.2017.10.023.

[104] Bico Group, "Needle supplier." [Online]. Available: https://www.cellink.com/

[105] M. C. Ribeiro *et al.*, "A New Versatile Platform for Assessment of Improved Cardiac Performance in Human-Engineered Heart Tissues," pp. 1–17, 2022.

[106] T. Kamperman, V. D. Trikalitis, M. Karperien, C. W. Visser, and J. Leijten, "Ultrahigh-Throughput Production of Monodisperse and Multifunctional Janus Microparticles Using in-Air Microfluidics," *ACS Applied Materials and Interfaces*, vol. 10, no. 28, pp. 23433–23438, 2018, doi: 10.1021/acsami.8b05227.

[107] M. Kaya *et al.*, "Visualization of micro-agents and surroundings by real-time multicolor fluorescence microscopy," *Scientific Reports*, vol. 12, no. 1, 2022, doi: 10.1038/s41598-022-17297-7.

[108] M. Kaya, F. Stein, J. Rouwkema, I. S. M. Khalil, and S. Misra, "Serial imaging of micro-agents and cancer cell spheroids in a microfluidic channel using multicolor fluorescence microscopy," *PLoS ONE*, vol. 16, no. 6 June, pp. 1–24, 2021, doi: 10.1371/journal.pone.0253222.

[109] G. E. Neurohr and A. Amon, "Relevance and Regulation of Cell Density," *Trends in Cell Biology*, vol. 30, no. 3, pp. 213–225, 2020, doi: 10.1016/j.tcb.2019.12.006.

[110] F. Feijó Delgado *et al.*, "Intracellular Water Exchange for Measuring the Dry Mass, Water Mass and Changes in Chemical Composition of Living Cells," *PLoS ONE*, vol. 8, no. 7, 2013, doi: 10.1371/journal.pone.0067590.

[111] T. Bhattacharjee *et al.*, "Liquid-like Solids Support Cells in 3D," 2016, doi: 10.1021/acsbiomaterials.6b00218.

[112] E. Station, "(Chudiakov, 1935;," 1945.

[113] C. D. Morley *et al.*, "Quantitative characterization of 3D bioprinted structural elements under cell generated forces," *Nat Commun*, vol. 10, no. 1, pp. 1–9, 2019, doi: 10.1038/s41467-019-10919-1.

[114] E. Y. S. Tan, S. Agarwala, Y. L. Yap, C. S. H. Tan, A. Laude, and W. Y. Yeong, "Novel method for the fabrication of ultrathin, free-standing and porous polymer membranes for retinal tissue engineering," *Journal of Materials Chemistry B*, vol. 5, no. 28, pp. 5616–5622, 2017, doi: 10.1039/c7tb00376e.

[115] A. Kirillova, R. Maxson, G. Stoychev, C. T. Gomillion, and L. Ionov, "4D Biofabrication Using Shape-Morphing Hydrogels," vol. 1703443, pp. 1–8, 2017, doi: 10.1002/adma.201703443.

[116] M. Champeau, D. A. Heinze, T. N. Viana, E. R. de Souza, A. C. Chinellato, and S. Titotto, "4D Printing of Hydrogels: A Review," *Advanced Functional Materials*, vol. 30, no. 31, pp. 1–22, 2020, doi: 10.1002/adfm.201910606.

[117] T. Glaser, V. B. Bueno, D. R. Cornejo, D. F. S. Petri, and H. Ulrich, "Neuronal adhesion, proliferation and differentiation of embryonic stem cells on hybrid scaffolds made of xanthan and magnetite

nanoparticles," *Biomedical Materials (Bristol)*, vol. 10, no. 4, 2015, doi: 10.1088/1748-6041/10/4/045002.

[118] C. W. Visser, T. Kamperman, L. P. Karbaat, D. Lohse, and M. Karperien, "In-air microfluidics enables rapid fabrication of emulsions, suspensions, and 3D modular (bio)materials," *Science Advances*, vol. 4, no. 1, pp. 1–9, 2018, doi: 10.1126/sciadv.aao1175.

[119] F. Gu, B. Amsden, and R. Neufeld, "Sustained delivery of vascular endothelial growth factor with alginate beads," *Journal of Controlled Release*, vol. 96, no. 3, pp. 463–472, 2004, doi: 10.1016/j.jconrel.2004.02.021.

[120] Q. Feng, D. Li, Q. Li, X. Cao, and H. Dong, "Microgel assembly: Fabrication, characteristics and application in tissue engineering and regenerative medicine," *Bioactive Materials*, vol. 9, no. July 2021, pp. 105–119, 2022, doi: 10.1016/j.bioactmat.2021.07.020.

Appendix I. Experiment Overview

Table 1. Overview of experiments, their bioink and embedding bath compositions and the figures for which their data is presented

	Description	Ink composition		Bath composition	Figures
Exp. 1	Fluorescently labelled ink components for detailed exploration of deposition and diffusion packing	-	Coumarin 6 stained particles	1.5%/2.0% XG/SA – Milli-Q-water 1.5% XG – Milli-Q-water	**Figure 3** **Figure 5** **Figure 6** **Figure 7.C-D** **Figure 8**
		-	Rhodamine B		
		-	Milli-Q-water		
Exp. 2	Small particle laden ink	-	Acrylic paint pigments | $\emptyset_{avr}$ ≤10 µm	0.5% (w/v) XG – DPBS	**Figure 4.B** **Figure 7.B** **Figure 15** **Figure 24** **Figure 28.III-VI**
		φ_p0.05			
		10%	Rhodamine B		
		40%	OptiPrep		
		45%	DPBS		
Exp. 3	Non-proliferating cells species in Newtonian hydrogel bath	12.2×10^6 mL^{-1}	FLB-CMs	1.5%/1.5% (w/v) XG/SA – Milli-Q water	**Figure 16.E**
		φ_p 0.10	$\emptyset_{avr}$ 25 μm		
		5 μL mL^{-1}	hCol-I (1 mg mL^{-1} stock)		
		7.5 μL mL^{-1}	hCol-III (1 mg mL^{-1} stock)		
		20%	OptiPrep		
		70%	CM-MM		
Exp. 4	Large particle-laden ink	20×10^3 mL^{-1}	Fluorescent alginate hydrogel μbeats	1.5% (w/v) XG – DPBS	**Figure 17.A-B** **Figure 28.I** & **IV**
		φ_p 0.1	$\emptyset_{avr}$ ±210 µm		
		20%	OptiPrep		
		70%	DPBS		
Exp. 5	Cell spheroid-laden bioink	14.1×10^3 mL^{-1}	Thawed RFP-SMCs (P4+4) spheroids	0.75% (w/v) XG – SMC-GM1	**Figure 11.B** **Figure 17.C-D** **Figure 25.C-D** **Figure 31** **Figure 32** **Figure 33**
		φ_p 0.1	$\emptyset_{avr}$ ±109.6 μm		
		20%	OptiPrep		
		70%	SMC-GM2		
Exp. 6	Acrylic paint particles-laden ink	-	Mostly iron oxide dye pigments particles	1.5% (w/v) XG – DPBS	**Figure 17.E**
		φ_p ±0.05	$\emptyset$ <10 μm		
		Trace amount	Soap		
		95%	DPBS		
Exp. 7	Non-proliferating cells in hydrogel bioink	12.2×10^6 mL^{-1}	FLB Lact. Pur. CMs (P27+44)	1.5% (w/v) XG – DMEM	**Figure 18.I-II**
		φ_p 0.10	$\emptyset_{avr}$ 25.0 μm		

		2.1 μg mL^{-1}	hCol-I (1 mg mL^{-1} stock)	1.5%/1.5% (w/v) XG/SA – DMEM	
		3.0 μg mL^{-1}	hCol-III (1 mg mL^{-1} stock)		
		0.75% (w/v)	XG		
		90%	CM-MM		
Exp. 8	Proliferating iPSCs-laden bioink	37.3×10^6 mL^{-1}	WTC iPSCs (P40+12)	1.5% (w/v) XG – E8 SC-medium	**Figure 18.VIII-X** **Figure 21** **Figure 22.I-IV** **Figure 29**
		φ_p 0.134	$\emptyset_{avr}$ ±18.3 µm		
		20%	OptiPrep		
		2%	P/S		
		64.6%	E8 SC-medium		
Exp. 9	Bioink containing multiple non-proliferating cardiac cell types (V2)	12×10^6 mL^{-1}	Thawed DRRAGN-derived CMs (P10+21)	1.5% (w/v) XG – CM-GM	**Figure 18.III-IV** **Figure 34**
		φ_p^{CM} 0.04	$\emptyset_{avr}$ ±19.9 μm		
		29×10^6 mL^{-1}	Thawed DRRAGN-derived ECCs (P4+27)		
		φ_p^{ECC} 0.05	$\emptyset_{avr}$ ±15.2 μm		
		φ_p^{tot} 0.09			
		20%	OptiPrep		
		71%	CM-GM		
Exp. 10	Proliferating C2C12-cells-laden hydrogel bioink in non-Newtonian XG bath	87×10^6 mL^{-1}	C2C12-cells (P16+7)	1.5% (w/v) XG – C2C12-medium 1.5%/1.5% (w/v) XG/SA – C2C12-medium	**Figure 18.V-VII** **Figure 19**
		φ_p 0.10	$\emptyset_{avr}$ 13.0 μm		
		1.0% (w/v)	XG		
		90%	C2C12-med		
Exp. 11	Medium size particle-laden ink	6.9×10^6 mL^{-1}	PLA-microparticles	1.5% (w/v) XG - DPBS	**Figure 22.V-VIII** **Figure 28.II-V**
		φ_p0.05	$\emptyset_{avr}$ ±30 µm		
		70%	OptiPrep		
		10%	P/S		
Exp. 12	proliferating C2C12-cells-laden bioink in viscous Newtonian XG/SA hydrogel baths	8.3×10^6 mL^{-1}	C2C12 (P16+2)	1.5%/2.0% (w/v) XG/ALG – C2C12-medium	**Figure 25.E-F**
		φ_p 0.01	$\emptyset_{avr}$ 13 μm		
		20%	OptiPrep		
		79%	C2C12-medium		
Exp. 13	Bioink containing multiple non-proliferating cardiac cell types (V1)	8.1×10^6 mL^{-1}	Thawed DRRAGN-derived CMs (P10+21)	1.5% (w/v) XG – CM-GM	**Figure 34.C**
		φ_p 0.04	$\emptyset_{avr}$ ±19.9 μm		
		45.9×10^6 mL^{-1}	Thawed ECCs (P1+3)		
		φ_p 0.08	$\emptyset_{avr}$ ±15.2 μm		
		φ_p^{tot}0.12			
		20%	OptiPrep		
		68%	CM-GM		
Exp. 14	Non-proliferating CM-laden bioink	15.5×10^6 mL^{-1}	Thawed DRRAGN-derived CMs (P20+33)	1.5% (w/v) XG – CM-MM	**Figure 30** **Figure 37** **Figure 38**
		φ_p 0.064	$\emptyset_{avr}$ ±19.9μm		
		4 μg mL^{-1}	hCol-I		
		6 μg mL^{-1}	hCol-II		
		20%	OptiPrep		

		75%	CM-MM		
Exp. 15	Bioink containing proliferating SMC-spheroids and Col-PLA-μparticles	1.04×10^5 mL^{-1} φ_p^{sph} 0.017	Thawed RFP-SMCs (P4+4) spheroids $\emptyset_{avr}^{sph}$ ±67.3 µm	1.5% (w/v) XG – SMC-GM2	**Figure 35**
		1.2×10^6 mL^{-1} $\varphi_p^{\mu p}$ 0.017	Collagen coated PLA-μparticles $\emptyset_{avr}^{\mu p}$ ±30.3 μm		
		φ_p^{tot} 0.034			
		46%	OptiPrep		
		50.5%	SMC-GM2		
Exp. 16	Bioink containing proliferating SMCs and Col-PLA-μparticles	7.7×10^6 mL^{-1} φ_p^{SMC} 0.075	RFP-SMCs (P4+3) $\emptyset_{avr}^{SMC}$ ±26.5 μm	1.5% (w/v) XG – SMC-GM2	**Figure 36**
		8.9×10^5 mL^{-1} $\varphi_p^{\mu p}$ 0.013	Col-PLA-μparticles $\emptyset_{avr}^{\mu p}$ ±30.3 μm		
		φ_p^{tot} 0.088			
		24%	OptiPrep		
		67.2%	SMC-GM2		

Appendix II. Components of Culture Media

Table 2. Overview of compositions of used culture media and thus bioink liquid phase

Culture medium	Concentration	Component	Supplier	Catalogue #
SC-GM		E8	Thermo Fisher	1517001
	0.5%	RevitaCell	Thermo Fisher	A2644501
CM-MM		see **Apx II** for full composition		
CM-GM		DMEM	Thermo Fisher	41965-039
	10%	Horse Serum	Thermo Fisher	26050088
	1%	P/S	Thermo Fisher	15070063
	10 μg/mL	Insulin	Sigma-Aldrich	I9278
ECC-GM		BPEL, see **Apx II** for full composition		
	10 μM	SB43	R&D Systems	1614
SMC-GM1		Smooth Muscle Cell Growth Medium:	Cell applications inc.	311-500
	1%	P/S.	Thermo Fisher	15070063
SMC-GM2		Smooth Muscle Cell Growth Medium-2	Lonza	CC-3182
	-	SMC-GM2-Supplements	Lonza	CC-4149
	1%	P/S	Thermo Fisher	15070063
SMC-GM3	76,5%	DMEM	Thermo Fisher	41965-039
	2.5%	1M HEPES (in PBS)	Fisher Scientific	BP310
	20%	FBS	Sigma-Aldrich	F7524
	1%	P/S.	Thermo Fisher	15070063
C2C12-med	89%	DMEM	Thermo Fisher	41965-039
	10%	FBS	Sigma-Aldrich	F7524
	1%	P/S	Thermo Fisher	15070063

Table 3. Composition of Cardiomyocytes Maturation Medium (CM-MM)

Component	Concentration	Supplier	Catalogue number
DMEM	-	Sigma-Aldrich	D5030
D(+)-Glucose	15 mM	Millipore	1083371000
Sodium Pyruvate	0.5 mM	Thermo Fisher	13360039
Sodium 3-hydroxybutyrate	0.19 mM	Sigma-Aldrich	54965
L-Carnitine hydrochloride	0.5 mM	Sigma-Aldrich	C0283
Creatine monohydrate	1 mM	Sigma-Aldrich	C3630
Taurine	5 mM	Sigma-Aldrich	T8691
Phenol Red	0.011 g/L	Sigma-Aldrich	P3532
Trace elements A	1:1000	Cellgro	25-021-CL
Trace elements B	1:1000	Cellgro	25-022-CL
Trace elements C	1:1000	Cellgro	25-023-CI
Chemically defined lipid concentrate	1:100	Thermo Fisher	11905031
GlutaMAX™ supplement	2 mM	Thermos-Fisher	35050038
α-thioglycerol	0.45 mM	Sigma-Aldrich	M6145
Insulin-Transferrin-Selenium-Ethanolamine (ITS-X)	1:1000	Thermo-Fisher	51500-056
Ascorbic acid-2P	10 μg/mL	Sigma-Aldrich	A8960
Penicillin-Streptomycin	0.5%	Thermo Fisher	15070063
Sodium hydrogen carbonate	3.7 mg/mL	Millipore	1063290500
BSA	2.5 mg/mL	Bovostar	BSAS 0.5
The following is added no more than 1 week before the medium is used:			
Thyroid hormone triiodothyronine (T_3)	100 nM	Sigma-Aldrich	T6397
R3 insulin-like growth factor 1 human (I)	100 ng/mL	Sigma-Aldrich	I1271
Dexamethasone (D)	1 μM	Tocris	1126/100
Sodium DL-Lactate, syrup, 60% (w/v) (L)	7.81 μL/mL	Sigma-Aldrich	L1375
D-(+)-Glucose anhydrous (G) (Diluted in LI-medium)	450 nM	Sigma-Aldrich	346451

Table 4. Composition of BSA polyvinyl alcohol, essential lipids medium (BPEL-medium)

Component	Concentration	Supplier	Catalogue number
IMDM	43%	Thermo Fisher	21056023
Ham's F-12 Nutrient mix, GlutaMAX™ supplement	43%	Thermo Fisher	31765027
PHHM-II Protein-Free Hybridoma Medium	5%	Thermo Fisher	12040077
Chemically Defined Lipid Conentrate	2.5%	Thermo Fisher	11905031
Insulin-Transferrin-Selenium-Ethanolamine (ITS -X)	2.5%	Thermo Fisher	51500056
GlutaMAX™ Supplement	1%	Thermo Fisher	35050038
P/S (5,000 U/mL)	0.1%	Thermo Fisher	15070063
Poly(vinyl alcohol)	0.3%	Sigma	P8136
1-Thioglycorol (a-MTG)	1%	Sigma	M6145
L-Ascorbic acid 2-phosphate sesquimagnesium salt hydrate	1%	Sigma	A8960-5G
BSA	0.5%	Bovostar	BSAS 0.5